HIGH-PERFORMANCE TORQUE CONTROL OF SWITCHED RELUCTANCE MOTOR

SANJIB KUMAR SAHOO

NATIONAL UNIVERSITY OF SINGAPORE

2006

HIGH-PERFORMANCE TORQUE CONTROL OF SWITCHED RELUCTANCE MOTOR

SANJIB KUMAR SAHOO
(B.Tech(Hons.), IIT, Kharagpur, India)

A THESIS SUBMITTED

FOR THE DEGREE OF DOCTOR OF PHILOSOPHY

DEPARTMENT OF ELECTRICAL AND COMPUTER ENGINEERING
NATIONAL UNIVERSITY OF SINGAPORE
2006

Acknowledgments

My thesis supervisor, Assoc. Prof. Sanjib Kumar Panda has been a source of incessant encouragement and patient guidance throughout the thesis work. I express my gratitude to the Almighty for arranging our first meeting aboard a plane, where I got my initial motivation from him to pursue higher studies. My second thesis supervisor, Prof. Jian-Xin Xu has given me invaluable help in control theory and applications. I am grateful to him for motivating me towards better productivity. I am thankful to the professors in Drives, Power and Control Systems group at NUS, for their help and guidance in various ways. I wish to express my thanks to Mr. Y. C. Woo, and Mr. M. Chandra of Electrical machines and Drives lab, NUS, for their readiness to help on any matter. My fellow research scholars from the lab have been great in keeping my spirits up. For all the discussions on power electronics and drives or the tea breaks and lunches together, I will miss them for ever. I would like to thank the thesis examiners for their feedback on the thesis draft. My wife Suprava and daughter Sara have been bearing with me for the long hours and numerous weekends I have spent in the lab, and away from them. I wish to dedicate this thesis to their love and support.

Contents

Summary

In traditional switched reluctance motor (SRM) operation, stator phase windings are excited one at a time, in sequence. Due to the finite phase winding inductance, instantaneous commutation of phase torque or current is not possible. There is large variation in motor torque during phase commutation, leading to torque ripples. Torque ripples can be minimized by controlled sharing of torque production by neighboring phases. Secondly, torque production mechanism in SRM is highly nonlinear and hence it is difficult to achieve accurate torque control. This thesis investigates methods for accurate torque control of SRM, for both minimization of torque ripples and accurate average torque control.

Due to doubly-salient construction and the small air gap in SRM, there is excessive flux-fringing near the start of overlapping between stator and rotor poles. As overlapping increases, SRM enters into deep magnetic saturation. Due to flux-fringing and magnetic saturation, flux-linkage and torque are nonlinear functions of phase current and rotor position. A novel polynomial model has been developed for flux-linkage in terms of phase current and rotor position, by dividing the operating range into four separate regions. The models for incremental inductance, back-emf constant, and instantaneous torque are derived from the flux-linkage model. These models are quite accurate and computationally economical, compared to exponential and trigonometric functions based models reported in the literature. This modelling approach is suitable for real-time controller implementation.

A suitable torque sharing function (TSF) is designed to distribute the demanded motor torque among two neighboring phases simultaneously. Although a fast changing TSF leads to high operating efficiency, the maximum rate of change of phase torque is limited by the available DC-link voltage. A cubic torque sharing function is chosen for the work reported in this thesis. This TSF is the simplest possible for obtaining continuous and trackable phase current reference for a given motor torque demand.

Conventionally, torque control in electric drives is done indirectly by first converting the torque reference to equivalent current reference, followed by an inner current control loop. As SRM torque is a nonlinear and coupled function of phase current and rotor position, torque-to-current conversion of the indirect torque control scheme becomes difficult. A novel iterative learning control (ILC) based method has been proposed for torque-to-current conversion in real-time. For constant torque and constant motor speed, the phase torque references are periodic. Taking advantage of this fact, ILC has been used. Then, ILC-based controller is developed for accurate current tracking in the phase windings. An 'indirect torque controller' has been tested on the prototype SRM using two ILC blocks, one each for torque-to-current conversion and current tracking controller. This scheme can be used for constant torque reference and can minimize torque ripples without requiring a detailed model for SRM magnetic characteristics.

The two ILC controllers in the indirect torque control (IDTC) scheme will interact with each other, and can not be allowed to be active simultaneously. To overcome this problem, a 'direct torque control' (DTC) scheme is developed for phase torque tracking. This approach avoids the torque-to-current conversion. A spatial ILC scheme is proposed and implemented to cater for varying-speed applications. Next, for catering to applications where demanded torque is time-varying but differentiable, a nonlinear robust tracking control (NLRTC) method is developed. This method uses a simple trapezoidal phase inductance profile to calculate an equivalent controller which is basically the nominal feed-forward control signal. Then a feedback controller with variable gain is added to ensure torque tracking error to be within a small bound. This robust control method is appropriate for speed or position control applications required in servo drives.

The fundamental frequency of torque ripples in SRM is proportional to motor speed. The mechanical subsystem of the drive acts a low pass filter to the motor torque ripples. Hence, the effect on speed is reduced at high speed operations. The focus of this thesis work to minimize torque ripples in the low speed range. All the proposed methods have been validated on the prototype SRM. The torque ripples have been reduced to within 5% to 10% of average motor torque, for speeds up to 200 r/min. The proposed controllers will be particularly useful for pick-n-place applications, which require ripple-free operation at rated torque, right up to zero speed.

List of Tables

List of Figures

Symbols

ψ	flux-linkage associated with stator phase winding
W_f	filed energy associated with stator phase winding
W_c	Co-energy associated with stator phase winding
i	stator phase current
θ	rotor pole position with respect to stator pole
L	inductance of stator phase winding
W_e	electrical energy associated with stator phase winding
T_{av}	average motor torque
T_j	torque produced by phase j
T_d	demanded motor torque
β_s	stator pole arc
β_r	rotor pole arc
N_r	number of rotor poles
N_s	number of stator poles
L_u	phase inductance at unaligned rotor position
L_a	phase inductance at aligned rotor position

K	position rate of change of phase inductance
V_{dc}	DC-link voltage
v	phase voltage
R	phase winding resistance
ω	rotor speed ($rad\,\mathrm{sec}$)
C_T	effective phase torque constant
j	phase number (1 to 4)
θ_c	critical rotor position
$f(\theta)$	torque sharing function
T_{inc}	increasing torque share
T_{dec}	decreasing torque share
θ_{on}	phase on angle
θ_v	overlap angle for conduction of two nearby phases
$\theta_{v_{min}}$	minimum overlap angle
J	rotational inertia of drive system reflected on rotor
T_e	total motor torque(sum of all phase torque)
T_l	load torque
B	friction constant
x	system dynamic state variable
$\mathbf{x}$	system state vector
u	control input

t	time in sec
i_s	stator current after which core saturates heacily
θ_h	hinge-point for the two regions in rotor position
I_j^{fb}	j^{th} phase current feedback
v_j	j^{th} phase voltage
K_p	pi controller P-gain
K_i	pi controller I-gain
I^{err}	current tracking error
d	duty cycle
I^*	current reference
I	current output
G_c	closed-loop transfer function
ω_n	natural frequency
ζ	damping coeffficient
s	switching surface
ϕ	error boundary width
u_{eq}	equivalent control
M	bound of control voltage uncertainty
$\hat{u}_{eq}$	nominal equivalent voltage
$sgn(.)$	sign function
x_d	desired state
W	switching voltage magnitude

T^*	phase torque reference
T^*_{inc}	increasing phase torque reference
T^*_{dec}	decreasing phase torque reference
v_{ilc}	ILC control voltage
G_1	current control ILC gain
G_2	torque-to-current converter ILC learning gain
G_3	DTC ILC learning gain
F	compensating factor for saturation effect in torque productivity
N_i	number of position intervals for ILC
$T^{err}_{filtered}$	filtered phase torque error
u_{ff}	feed-forward control voltage
u_{fb}	feedback control voltage
e_b	error boundary

Acronyms

SRM	Switched Reluctance Motor
ILC	Iterative Learning Control
SMC	Sliding Mode Control
NLRTC	Nonlinear Robust Tracking Control
TSF	Torque sharing fucntion
DC	Direct Current
AC	Alternating Current
EMF	Electro-motive Force
PI	Proportional-Integral
PID	Proportional-Integral-Derivative
VSC	Variable Structure Control
PWM	Pulse-Width-Modulation
PC	Personal Computer

IDTC	Indirect Torque Control
DTC	Direct Torque Control
MB	Mega Byte
ADC	Analog to Digital Conversion
DAC	Digital to Analog Conversion
IO	Input Output
TTL	Transistor Transistor Logic

Chapter 1

Introduction

Many industrial automation applications need variable speed operation for improving energy efficiency or product quality. Electric drives [1] are preferred in variable speed applications for their ease of control, clean operating environment, and easy access of electricity at the point of use. DC motors are easiest to control and are commonly used in such applications. However, brush-commutator of DC motors adds to cost, complexity and need frequent maintenance. AC motors are more robust than DC motors, but generally difficult from control of view. With advancement in power electronics and microprocessor technology, AC motor control performance has been improved substantially. Due to this reason, more and more AC motors are used in variable speed applications. In the field of electric drives, research is directed towards adopting more robust motors in variable speed drive applications.

SRM have the simplest and most robust construction among all electric motors. Both stator and rotor are stacks of laminated sheets, with only stator having concentric coils. There are no permanent magnets or rotor bars on the rotor. These are also quite economical for mass manufacturing. SRM are better compared to induction motors in many ways as discussed in [2]. However, due to the double-salient construction and magnetic saturation, torque production is highly nonlinear. In conventional operation of SRM, the phase windings are switched on sequentially, one at a time. This mode of operation and the nonlinear torque production lead to large amount of torque ripples. Torque ripples can cause speed ripples, particularly at low speed operation. Such excitation also produces radial force on the rotor, leading to substantial vibration and acoustic noise [3]-[4]. Due to these reasons, SRM could not be used high-performance industrial applications.

Over the last few decades, researchers have suggested different techniques for mitigating this problem. This is still an open research problem and currently there is a lot of interest in it from the drives research community. The motivation behind this thesis has been to improve the toque control performance of SRM, making use of advanced control techniques and the latest digital hardware. With improved torque control, SR drives can be used for high-performance motion control applications.

1.1 Operating Principle of SRM

Switched reluctance motor works on reluctance torque principle [5]-[6]. Reluctance torque/force principle was the earliest (in first half of nineteenth century) known method of producing motion using electromagnetism. It is equivalent to an electromagnet pulling a piece of soft iron towards it so that the reluctance of the associated magnetic circuit is minimized. In switched reluctance motors, both stator and ro-

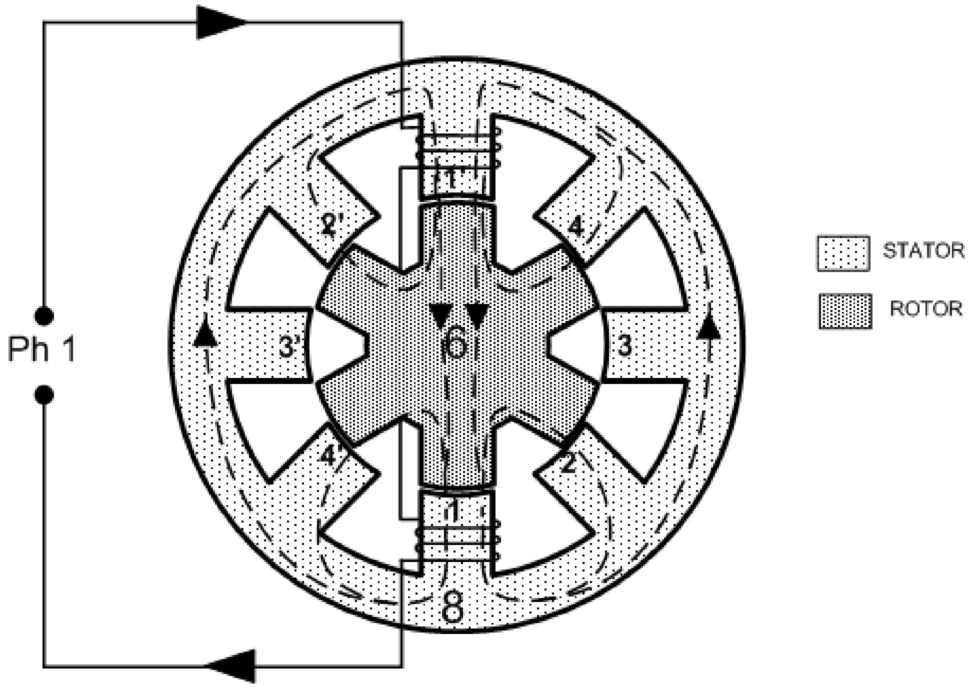

Figure 1.1: Cross-sectional view of SRM showing the stator, rotor, one phase winding and magnetic-flux path.

tor have salient poles, of different numbers, as shown in Fig.1.1. The SRM used in the experimental setup for this thesis work has 8 stator poles and 6 rotor poles. Each stator pole has a concentric coil wound around it. The windings on two stator poles, which are at exactly 180 degrees with each other (1-1',2-2',3-3' and 4-4'), are connected in series to constitute the phase winding (phase1 winding is shown in Fig.1.1). There are four phases for an 8/6 pole SRM. The magnetic path for one phase is shown, consisting of the stator core, stator poles, air gap, rotor poles and rotor core. It is worth noting that there will be some flux passing through the neighboring phases, but the mutual inductance of phase windings is found to be of very small magnitude as compared to self inductance. When two diametrically opposite rotor poles are aligned with the stator poles in a phase (the corresponding rotor position is called 'aligned position'), the reluctance of the magnetic path is at its minimum. The corresponding phase inductance would then be maximum. When the rotor poles are away from the stator poles, the reluctance increases and

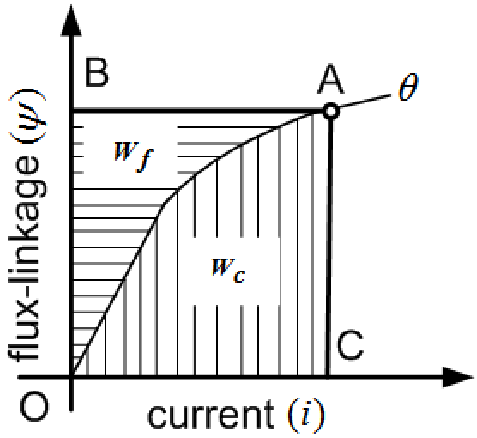

Figure 1.2: Field-energy (W_f) and co-energy (W_c) in SRM.

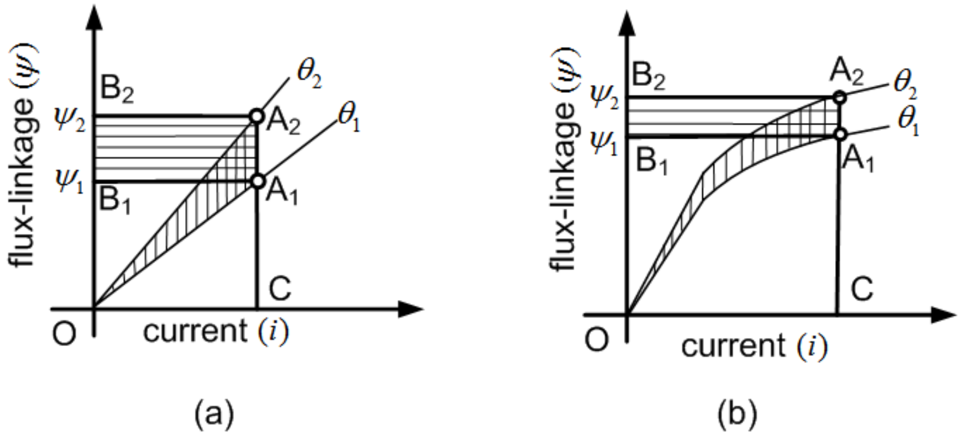

Figure 1.3: (a) Change in co-energy under linear magnetization, (b) Change in co-energy under saturated magnetization

is maximum when the rotor poles are right at the middle of two consecutive stator poles (the corresponding position is called 'unaligned' position). The phase inductance at unaligned position would be the minimum.

When any of stator phase windings is energized, the nearest rotor poles will experience a pull so as to align with the energized stator poles. Once the rotor poles fully align with the stator pole, the pulling torque will become zero. The fully aligned phase is then switched-off, and the next phase is switched on. Such sequential switching of phases produces a continuously rotating motion.

Fig. 1.2 shows the flux-linkage ψ vs. phase current i curve when rotor position is fixed at θ. In this case, the electrical energy input to the winding is stored as magnetic energy. The stored magnetic energy W_f (horizontally shaded area OAB), can be calculated as:

$$W_f = \int_0^t v\, i\, dt = \int_0^t \frac{d\psi}{dt} i\, dt = \int_0^\psi i\, d\psi \tag{1.1}$$

where v is the voltage across the phase winding. The vertically shaded area (OAC) under the ψ vs. phase current i curve represents a fictitious quantity called *co-energy*. This quantity does not have any physical meaning, but change in co-energy is same as the mechanical work done in electromagnetic system. This is useful for estimating the reluctance torque in SRM. Co-energy in Fig. 1.2 can be calculated as,

$$W_c = \int_0^i \psi\, di \tag{1.2}$$

Fig.1.3 shows the change in co-energy when phase current is maintained constant and rotor is allowed to move from position θ_1 to position θ_2. When motor operates in linear magnetic region (as can be seen in Fig.1.3.a), change in the co-energy is given by the triangular area (OA_1A_2) with vertical shading. The change in co-energy (ΔW_c), which is the amount of mechanical work done during the rotor movement, will be exactly one half of the electrical energy input (ΔW_e) to the phase, given by the area ($B_1A_1A_2B_2$).

$$\Delta W_e = \int e\, i\, dt = \int \frac{d\psi}{dt} i\, dt = i\,(\psi^2 - \psi^1) = (L^2 - L^1)\, i^2 \tag{1.3}$$

where ψ^2 and ψ^1 are flux-linkages at rotor positions θ_2 and θ^1 respectively; L^2 and L^1 are the phase inductance values at these rotor positions. The change in co-energy is equal to one half of the electrical energy ΔW_e:

$$\Delta W_c = \frac{1}{2}(L^2 - L^1)\, i^2 \tag{1.4}$$

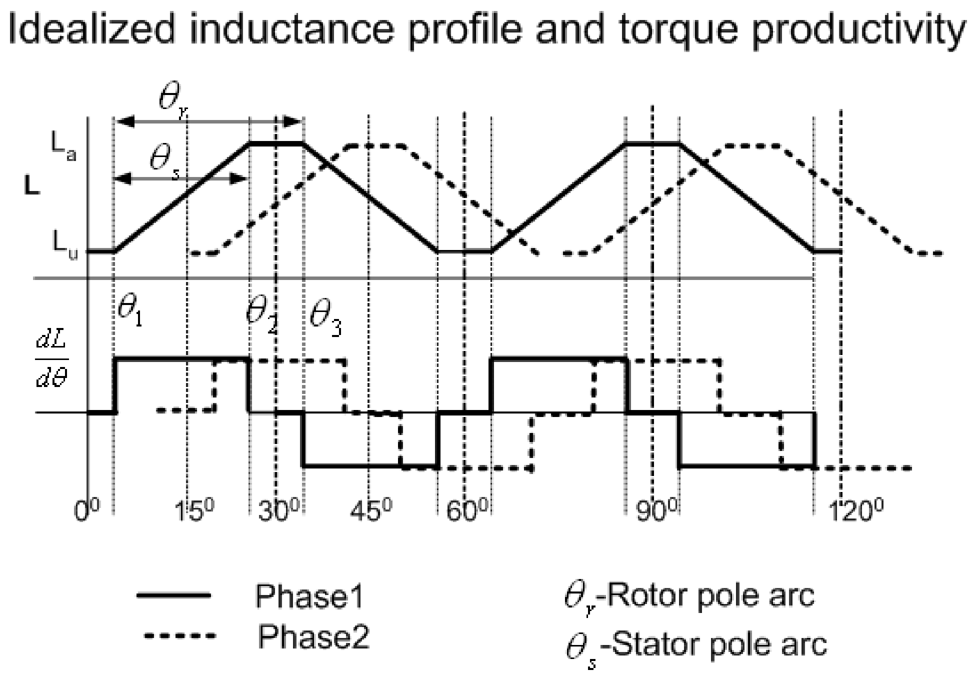

Figure 1.4: Trapezoidal profile for SRM phase inductance.

The average reluctance torque produce when rotor moves from θ_1 to θ_2, due to phase current i, is given by,

$$T_{av} = \frac{\triangle W_c}{\triangle\theta} = \frac{1}{2}i^2\frac{\triangle L}{\triangle\theta} = \frac{1}{2}\,i^2\frac{dL}{d\theta} \tag{1.5}$$

where $\Delta\theta$ is the displacement. Fig.1.3.b describes change in co-energy when the system enters into magnetic saturation region. Phase inductance depends on both rotor position as well as phase current. This complicates the calculation of average torque. However, it can be observed that the change in co-energy (mechanical work done) is more than one half of the input electrical energy. This results in better conversion ratio and hence, SRM is usually operated in deep magnetic saturation.

1.1.1 Trapezoidal Phase Inductance Profile

Assuming SRM to operate in linear magnetic region and that magnetic flux crosses the air gap only at 90^o, phase inductance can be idealized to be directly proportional to the overlap angle between stator and rotor poles. When stator and rotor poles are unaligned, this idealized phase inductance will be at the minimum (L_u). It will remain at this value as rotor pole approaches the stator pole, until the rotor pole tip meets the stator pole tip. Thereafter, it will rise at a constant rate as overlap angle increases and attain the maximum value (L_a) when there is maximum overlap. As per design practice, stator pole arc length (θ_s) is less than the rotor pole arc length (θ_r):

$$\theta_s < \theta_r \tag{1.6}$$

$$(\theta_s + \theta_r) < 2\pi/N_r \tag{1.7}$$

where N_r is the number of rotor poles. Due to this, the pole overlap remains constant for a period when the idealized phase inductance remains at the maximum value, L_a. As the rotor moves away from the stator pole, it will fall at a constant rate, until overlap becomes zero and it becomes L_u again. Therefore, the idealized phase inductance profile would have a trapezoidal shape as shown in Fig.1.4.

$$\begin{aligned}
L(\theta) &= L_u \text{ for } 0 \leq \theta \leq \theta_1 \\
&= L_u + K(\theta - \theta_1) \text{ for } \theta_1 \leq \theta \leq (\theta_1 + \theta_s) \\
&= L_a \text{ for } (\theta_1 + \theta_s) \leq \theta \leq (\theta_1 + \theta_r) \qquad (1.8) \\
K &= \frac{L_a - L_u}{\theta_s - \theta_r}
\end{aligned}$$

where K is the position rate of change of phase inductance.

The dotted line in Fig.1.4 belongs to a stator phase adjacent to the phase

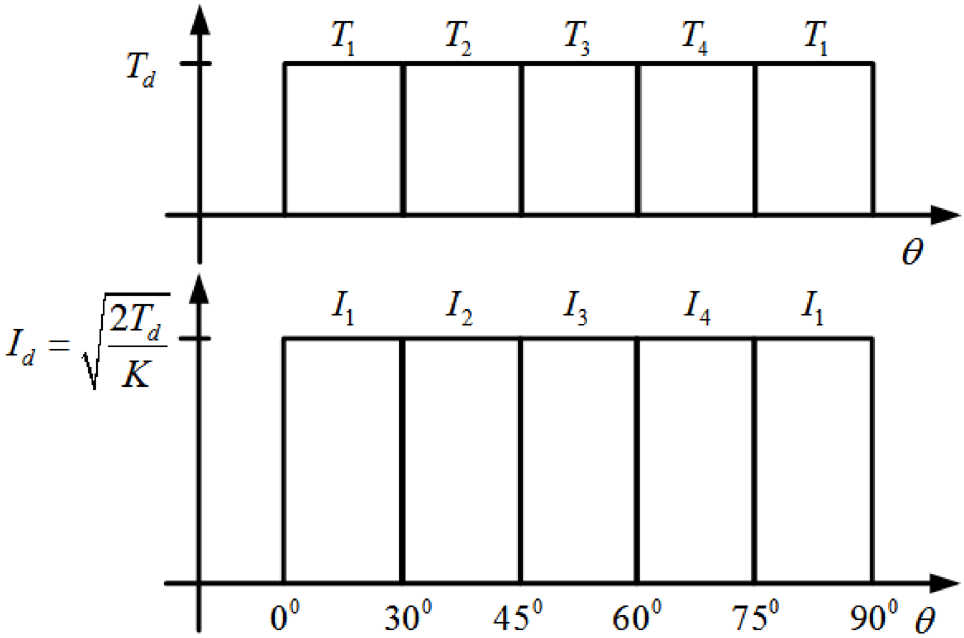

Figure 1.5: Phase torque shares and phase current references assuming linear magnetization.

discussed above. Hence, the phase inductance of all the phases can be obtained by suitably shifting the phase inductance profile of any one phase along the rotor position axis.

For this idealized phase inductance profile, instantaneous torque (T_{inst}) will be same as the average torque as in (1.5) i.e.

$$T_{inst} = \frac{1}{2}Ki^2 \tag{1.9}$$

where $K = \frac{dL}{d\theta}$ is the position rate of change of phase inductance. It is like the torque constant in DC series motor. In this case, SRM can generate constant torque if the phase windings are injected with rectangular current pulses as shown in Fig.1.5. As torque direction is independent of phase current direction, both motoring and braking torque production is possible with unidirectional current; by only placing the current pulse in the region of positive or negative K value.

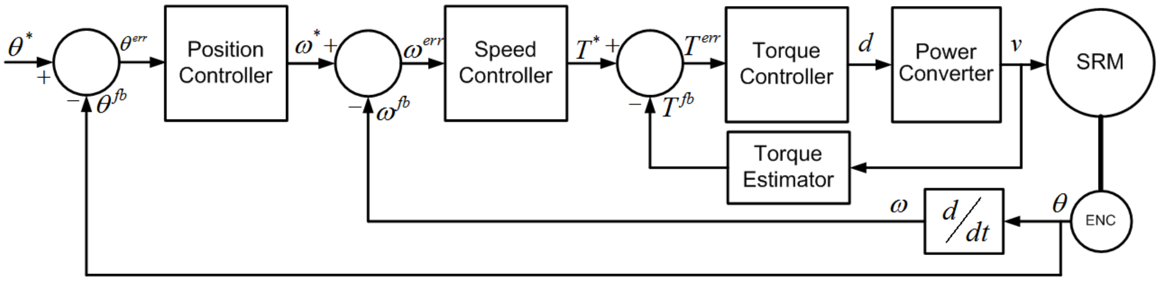

Figure 1.6: Block diagram of an SRM drive system used in motion control applications.

1.2 Problem Definition

A typical motion control system operates either in position control, velocity control or torque control mode. Fig.1.6 shows the block diagram representation of such a system. In closed-loop position control mode, the position error is used to obtain the speed reference for the inner speed control loop. Similarly, for the speed controller, there is an inner torque control loop. The accuracy of the outer loop depends on the bandwidth and accuracy of the inner loop controller. Hence, torque control is at the heart of a motion control system. For separately excited DC motor, with field current being kept constant, motor torque is proportional to armature current only. For AC motors, field-oriented-control (FOC) scheme converts the motor torque demand to equivalent stator current demand. For such drives, torque control is achieved indirectly through current controller. However, due to the nonlinear and non-invertible torque-current-rotor position relationship, torque control of SRM is quite complex and involved.

1.2.1 Electronic Phase Commutation

As described under section for SRM operating principle earlier, phase windings are switched in sequence to produce a rotating motion. It was shown that, at any time, only one phase conducts current and produces the total motor torque. The process of torque transfer from one phase to another is called phase commutation. Due to the non-zero phase inductance, and finite DC-link voltage available, it is impossible for the current to rise or fall instantaneously. Hence, in this operating mode where only one phase is excited at a time, there will be a large torque dip during the phase commutation. The peak-to-peak torque ripples due to non-ideal phase commutation can be even more than 100% of the average motor torque.

However, it can be seen in the Fig.1.4 that there is some overlapping in the torque producing regions of two adjoining phases. At any position, two phases can produce torque in same direction. During phase commutation, two nearby phases can share the total torque demand so as to avoid the torque dips during phase commutation. This can be put mathematically as:

$$\begin{aligned} T_d &= T_1 + T_2 \\ T_1 &= f(\theta) * T_d \\ T_2 &= (1 - f(\theta)) * T_d \end{aligned} \tag{1.10}$$

where T_d is the demanded motor torque, T_1 and T_2 are torque produced by the two conducting phases and $f(\theta)$ is the position dependent torque sharing function (TSF). Choice of $f(\theta)$ can not be arbitrary. Suitable TSF needs to be chosen as per various constraints.

1.2.2 Nonlinearity of SRM Magnetization Characteristics

Previous section describes the operating principles of SRM through the idealized phase inductance profile. However, in reality, there are some deviations in the phase inductance profile towards both the aligned and unaligned positions. Usually, SRM air-gap is smaller compared to other motors. When the rotor poles approach stator poles, there will be some flux fringing effect. This causes phase inductance to start rising even before the rotor pole tip reaches the stator pole. This is one cause of the actual phase inductance profile being different from the trapezoidal profile.

As seen in Fig.1.3(a), when SRM operates in linear magnetic region, only half of the electrical energy input to the phase winding gets converted to mechanical work. When SRM is operated in deep magnetic saturation region, more than half of the electrical energy input will be converted into mechanical work as shown in Fig.1.3(b). This reduces the amount of volt-amperes handled by the converter, for the same amount of work done by the motor. Hence, SRM is usually designed to work with deep magnetic saturation.

At the start of overlap between stator and rotor poles, only the pole tips carry the total magnetic flux. Hence, they get saturated at a very small current. As the overlap increases, saturation starts at a large current. With saturation, the effective phase inductance falls. The combined effect of flux-fringing and magnetic saturation, makes the phase inductance a nonlinear function of both rotor position and current. These effects result in a highly nonlinear and coupled relationship between phase torque, current and rotor position. So, a rectangular current pulse in the increasing inductance region, does not produce a rectangular torque pulse. To generate rectangular phase torque, it is essential to produce a position-dependent profile of the phase current.

These nonlinearities demand suitable nonlinear controller for good torque control accuracy. Nonlinear control laws are usually complex and require extensive on-line computation, possible by high-speed digital controller. Unlike linear controllers, nonlinear control techniques are specific to the type of plant nonlinearities. Hence, development of a suitable torque controller for SRM requires knowledge of the motor magnetization characteristics.

1.3 Review of Past Work on SRM Toque Control

The basic principles of operation of SRM were known for more than 150 years. However, due to the difficulty in its control, it could not become as popular as other motors. The paper by Lawrenson *et al.* [7], restarted interest in SRM in early eighties of the twentieth century. For the last two decades, there have been numerous works reported on SRM. A detailed survey on torque control schemes for SRM was done in [8]. Some researchers have tried special designs of SRM [9]-[10] to reduce the torque ripples. However, this approach negates the main advantage of SRM i.e. the simple design and construction of the motor. Hence, this thesis focuses on the control methods to solve the problem of torque ripples in multi-phase SRM with three or more phases.

Earlier works [11]-[12] using the micro-controllers for SRM control, were limited to varying the ON and OFF angles that would control the average torque of SRM. These two control angles were appropriately advanced to compensate for the loss in average torque as motor speed increases. This approach is effective for high speed operations, when operation is in single pulse mode. Torque ripples are not so critical at high speed as the system would act as an effective low-pass filter. However, such methods are not appropriate for torque ripple minimization at low speeds.

As high speed digital signal processors (DSP) became affordable, researchers started developing complex nonlinear control algorithms for SRM. In [13], Ilic'-Spong *et al.* had proposed using feedback linearization techniques for designing a speed control system for SRM. The nonlinearities in the state equations were compensated for, using state feedback, to obtain an equivalent linear system. PI controller was used for the transformed linear system. This process is computationally complex and requires an accurate nonlinear model of SRM. As finding an accurate nonlinear model for SRM is a very difficult task, practical application of such method is limited.

In [14], Taylor had made use of the large difference in the time constants of mechanical subsystem and the electrical subsystem. The mechanical subsystem was linearized, with motor torque as the control input. Desired motor torque is the reference input for the electrical system. The desired torque was first converted to phase current reference for each phase. A current controller with large gain was proposed to realize the current reference fast enough, so that the mechanical subsystem can ignore the current dynamics. However, the current controller was implemented using hardware, leading to an overall complex system.

Another common approach for trajectory control for nonlinear uncertain systems is the variable structure control (VSC). This approach was proposed in [15], [16] and [17] for designing a closed-loop speed controller for SRM. The controller consisted of two parts: an equivalent control that would cause the system to track the trajectory if model were accurate; and a switching control that would cause the tracking error to remain bounded in spite of any model in-accuracy. In [15], the authors had assumed that the SRM operates in the linear magnetic region. VSC based speed controller design also needs the system inertia and friction constant. Possible errors in so many parameters in the control scheme increases model-inaccuracy and hence, the burden on switching control increases. As switching control increases, the chattering amount increases and tracking performance decreases. Additionally, signum function was used for the switching control, giving voltages of $-V_{dc}$, 0 and V_{dc}. Due to limited bandwidth of a digital controller, such a switching logic would result in large variation of the controlled variable. In [17], motor operation in magnetic saturation region was considered. However, both the schemes used a single phase excitation scheme, which leads to drop in torque during the phase commutation period. This method still causes large amount of torque ripples.

The methods proposed in [13], [15] and [17] do not make any effort to reduce the torque ripples but focus on reducing the speed ripples by closed-loop control of speed. These schemes do not exploit the overlapping torque producing region of adjacent phases to use multi-phase excitation. Hence, these schemes can not be used for applications when drive has to be operated in torque control mode. However, if high-performance torque control of SRM drives is achieved, then a speed controller or position controller can be easily obtained by adding simple linear controller in the outer loop.

Another approach followed by researchers was to use intelligent techniques like artificial neural networks (ANN) as in [18]-[22] and Fuzzy control in [23]. In [18], Donovan *et al.* had used ANN to learn the nonlinear flux-linkage in terms of phase current and rotor position. A back propagation steepest descent algorithm is used to train a multi-layered feed-forward neural network. This method gives an analytical expression for flux-linkage from which torque expression can be derived. However, the number of neurons used was quite high for obtaining an accurate match of the flux-linkage. This leads to more computational load and hence is not suitable for real-time implementation. The torque matching was not good enough for being used for accurate torque estimation.

An adaptive fuzzy logic controller has been reported in [23] for torque ripple minimization of SRM. Fuzzy controller can approximate any analytical relationship and hence can be used for uncertain systems and can work with cheap and low-accuracy sensors. The torque reference is converted to equivalent current reference by using the fuzzy system. An LMS (least-mean-square) algorithm based adaptation scheme is used for adapting the weights based on output torque error, which adds robustness to the scheme. However, this system is not suitable for high-performance, ripple-free and very accurate torque control for SRM. In [25]-[26] Henriques *et al.* use Neuro-Fuzzy system for obtaining a compensation current component to be added to a standard PI speed controller output. The Neuro-Fuzzy system learns the compensation currents from the torque ripples, with training data generated by simulations. However, any off-line learned data requires large on-line memory for the range of torque and speed.

In [24], Panda *et al.* had proposed a PI controller for speed control of SRM, where the controller gains are scheduled according to Fuzzy rules and reasoning. Considering the nonlinearity of SRM torque generation mechanism, this approach gives a better speed performance compared to a fixed-gain PI controller. Two-phase-on approach was used for maximization of motor torque capability but no torque sharing was considered. Such approach produces large dips in motor torque near phase commutation.

Iterative learning control (ILC) is another popular control strategy for solving trajectory tracking control problem in nonlinear systems, without spending much effort on detailed modelling. In [28] Kim *et al.* had proposed ILC for improving machining accuracy in CNC machines. In [30] Xu *et al.* have used ILC for minimization of torque ripples in permanent magnet synchronous motor (PMSM). Similarly, Sahoo *et al.* [29] have used ILC to calculate the phase current references for phase torque references off-line and then store them in look-up tables. Though this scheme reduces torque ripples, it requires large amount of on-line memory.

Various control techniques have been reported in literature for SRM torque control. One approach converts the phase torque to phase current reference and uses a current controller for realizing the current reference. Often, an analog circuit based hysteresis controller is used to achieve accurate current control. Such approach has been in practice for a long time in drives industry. However, the analog circuits are known to be difficult to set up and maintain, as compared to digital systems. Also, analog circuit components can drift with aging and change in temperature and thus, may require re-tuning. Hence, most modern systems are developed on digital systems with advanced micro-controllers having digital signal processing capability. Advanced control techniques can be applied using these digital controllers for developing high-performance drives. The work for thesis is directed towards developing such a fully-digital controller for SRM drive.

1.4 Contribution of this Thesis

As described in the literature survey on SRM control, no definite control method has been established with accurate torque control. Hence, this thesis is aimed at developing an accurate torque controller for SRM. In many robotics and servo applications, direct drive principle is used. In these applications, the motor is operated at lower speed compared to gearbox based systems. Additionally, the drive is expected to produce rated torque right down to zero speed. Torque ripples can not be tolerated in such systems as they may produce speed ripples. Hence, accurate torque control is aimed mainly at removing any torque ripples at low speed and constant torque operations. Contribution of this thesis work is listed as following:

- A torque sharing function (TSF), with two cubic segments is developed for distribution of motor torque demand between two active phases. The design method for various parameter of the TSF like on-angle, overlap-angle is explained in details.
- A novel polynomial based model is developed for representing the measured phase flux-linkage as a function of phase current and rotor position. This analytical expression requires less memory than look-up tables. It is computationally less expensive as compared to the usual trigonometric or exponential functions. Hence, it is suitable for real-time implementation. This

model can be used for deriving other properties of SRM like incremental inductance, back-emf constant and instantaneous torque, analytically. The resulting torque model is used for torque feedback in torque control schemes in this thesis work.

- A novel iterative learning control based *'indirect torque control'* (IDTC) scheme is developed. Accurate torque-to-current conversion and current tracking are achieved by iterative learning control (ILC). As ILC does not need detailed knowledge of SRM's nonlinear magnetization characteristics, this method is very useful for minimizing torque ripples without spending any effort in modelling. However, this method is suitable only for applications when both torque and speed are constant.

- Then, a direct torque controller (DTC) is developed using ILC, which avoids the difficulties of torque-to-current conversion in indirect torque control. The problems of torque ripples in conventional bang-bang type DTC scheme are overcome by this method. The scheme can be used for applications when speed is varying, but motor torque demand is constant.

- For typical motion control applications, torque reference is time-varying. A novel DTC scheme is developed using nonlinear robust tracking control (NL-RTC), for accurate phase torque tracking when motor torque is time-varying. A nominal model is obtained from the flux-linkage data, which is used for designing a feed-forward control. Then, a varying-gain feedback controller is added to the feed-forward control to add robustness to the system.

- All the proposed control methods are validated experimentally using a 'dSpace-DS1104' DSP based R&D board for a prototype SRM having specifications: 8/6 poles, 4 phase, 1 hp, 4000 r/min.

1.5 Experimental Setup for the Thesis Work

Any proposed control algorithm for SRM needs to be verified on a prototype SRM. Mere simulation results showing good performance are not convincing due to the inevitable uncertainty in the nonlinear models for SRM. Hence, an experimental platform had been developed to verify the control algorithms. A rapid-control-prototyping system is used as the platform for validating the high-performance nonlinear tracking controller for a prototype SRM.

Fig.1.7 shows a block diagram of our experimental setup. Here is a list of modules used in the experimental platform:

- Prototype SRM
- Digital Controller for implementing the control algorithm
- Power converter
- Encoder/Tachogenerator
- Current sensors
- Signal pre-processing boards
- Loading system
- Torque Transducer

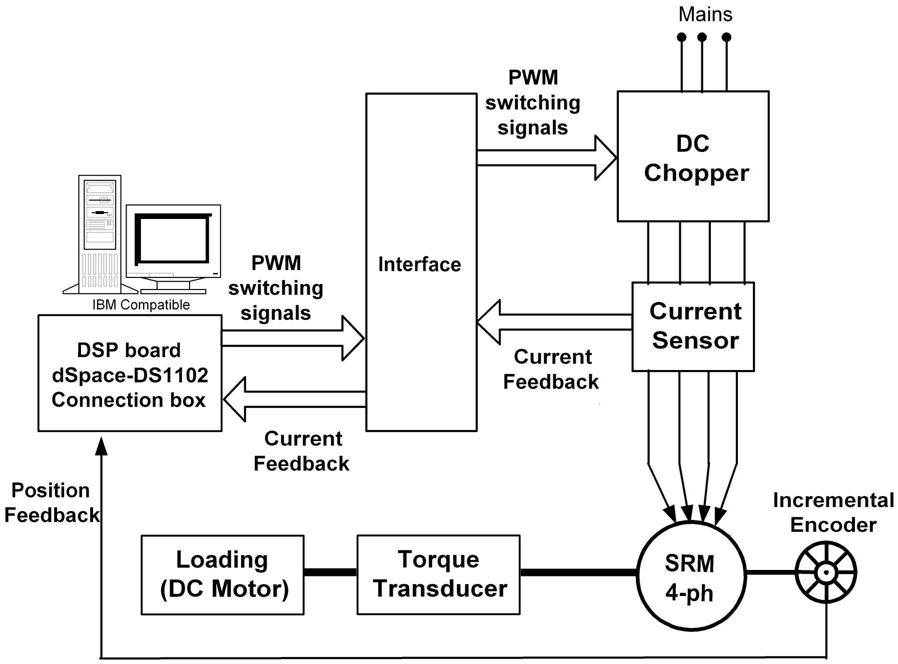

Figure 1.7: Experimental setup used for this thesis work

Table 1.1: Specifications of Prototype SRM

Rated Power	1 hp
No. of poles	8/6
Max speed	4000 $rmin$
Rated Torque	1.78 $N.m$

1.5.1 Prototype SRM

A four phase, 8/6 poles SRM has been used as the prototype for testing the control algorithms. Detailed specifications are given in Table 1.1.

1.5.2 Digital Controller

The 'dSpace' DS1104 R&D Controller Board has been used for testing the control algorithms. Some of its special features are as follows:

1.5.2.1 Hardware Features

- It is plugged into a PCI slot of a PC.
- It is a complete real-time control system based on a 603 PowerPC floating-point processor running at 250 MHz
- Memory
  - Global memory: 32 MB SDRAM
  - Flash memory: 8 MB
- Timer
  - sample rate timer (decrementer): 32-bit down counter, reload by software, 40 ns resolution
  - 4 general purpose timer: 32-bit down counter, reload by hardware, 80 ns resolution
- Interrupt
  - 5 timer interrupts
  - 2 incremental encoder index line interrupts
- ADC
  - 4 multiplexed channels equipped with one 16-bit sample hold ADC, 10 V input voltage range, 2 ms conversion time
  - 4 channels each equipped with one 12-bit sample hold ADC, 10 V input voltage range, 800 ns conversion time
- DAC

  - Eight 16-bit resolution, 10 V output voltage range, 5 mA maximum output current Max. 10 ms settling time

- Digital I/O
  - 20-bit parallel I/O Single bit selectable for input or output 5 mA maximum output current TTL output/input levels

- Encoder interface
  - 2 channels selectable single-ended (TTL) or differential (RS422) input fourfold line subdivision Max. 1.65 MHz input frequency, i.e. fourfold pulse counts up to 6.6 MHz 24-bit loadable position counter, reset on index. 5 V/0.5 A sensor supply voltage.

- PWM output Texas Instruments TMS320F240 DSP 16-bit fixed-point processor 20 MHz clock frequency slave DSP subsystem for timing signal generation
  - 3-phase PWM output
  - 4 x 1-phase PWM output
  - 14-bit digital I/O

1.5.2.2 Software Features

'ControlDesk' is dSPACE's software for carrying out experiments, a graphical user interface for managing the dSPACE boards. It provides all the functions to control, monitor and automate experiments and make the development of controllers more efficient. The dSPACE Real-Time Library, the real-time core software with a C programming interface is provided to help access the hardware I/O for implementation of the controller. Instrumentation offers a variety of virtual instruments

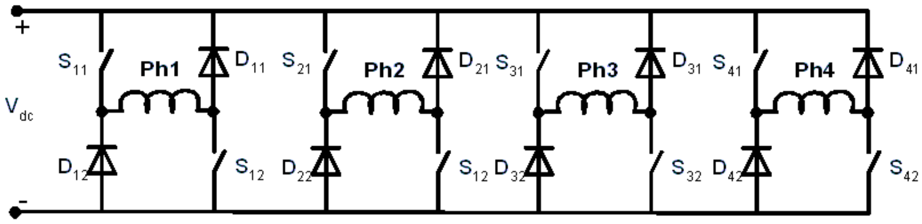

Figure 1.8: Schematic of an asymmetric bridge converter for a 4-phase SRM

to build and configure virtual instrument panels according the one's needs. Input instruments allow to change parameter values online. Any set of instruments can be combined to produce a virtual instrument panel that is specific to the application. In addition, Instrumentation provides data acquisition instruments from the application running on the real-time platform.

The control algorithms developed under the future chapters are written in 'C' programming language and have been verified on this experimental platform.

1.5.3 Power Converter for SRM

Various types of converters have been proposed in the literature for SRM. A good survey and comparison of the converter topologies are provided by Slobodan *et al.* in [31]. An asymmetric half-bridge converter with four half-bridges, as shown in Fig.1.8, is used to supply the four phases of SRM. The converter configuration is capable of applying $+V_{dc}$ (when S_{j1} and S_{j2} of the j^{th} phase are both closed), $-V_{dc}$ (when S_{j1} and S_{j2} are both open) or $0\,V$ when either of the switches are closed. With PWM, the voltage applied to each winding can be smoothly varied from $-V_{dc}$ to V_{dc}. The DC supply (V_{dc}) to the converter is supplied via a three-phase diode-bridge rectifier. It is also worth noting that there is no chance of 'shoot-through'

Table 1.2: Specifications of Position Encoder

Make	Hengstler
Model	RI58-O/4096AK.47RA
Pulses per rev	4096
Supply voltage	5V DC

condition in this converter. This adds to the robustness of the drive system.

1.5.4 Encoder

An incremental encoder is used for rotor position sensing as well as speed measurement. The encoder gives out an index pulse per each rotation which is captured by the contoller. The rotor position corresponding to the index pulse is obtained during initial setup and stored in memory. During each rotation, it is used to reset the position counter to the fixed value in memory. This helps obtaining the absolute rotor position, required for SRM control.

1.5.5 Current Sensor

Four current sensors are used for independent measruement of the four phase currents. Here, multi-range (5-8-12-25A) LEM Module LA 25-NP current sensors are used. In this application, primary to secondary turns ratio is selected to be 1:1000 (thereby the current range becomes $25\,A$). Across the output, $300\,\omega$ resistor is connected to convert the sensed current signal into an equivalent voltage signal. With the above turns ratio, the calibrated voltage signal is given by $0.3\,V/A$. Finally, the circuit board containing the four current sensors is put inside another shielding box to minimize the EMI effect.

1.5.6 Signal Pre-processing Boards

The DSP interfacing circuits consist of filters for phase current signals, over-current protection circuit, buffers for pulses coming form the incremental encoder and PWM interface circuit. Filters are required for the current signals since they generally come from noisy environments and it is necessary to minimize their noise content before feeding them into DSP for processing. They also act as anti-aliasing filters for the digital controller. According to 'Sharon's Sampling Theorem', the analog input to a digital system should not contain any frequency component beyond half the sampling frequency of the digital system. These two issues determine the cut-off frequencies for the filters. In the present implementation, second order low-pass Butterworth filters are used. The cut-off frequencies are chosen to be 1 kHz. Further, programmable gain amplifiers (PGAs) with a gain of 2 have been used in the filters to ensure the full load current spans the input range of the the ADC converters($\pm 10\,V$). With this PGA gain, the current signals are calibrated as $1.6667\,A/V$. The outputs of the PGAs are connected to the ADC inputs of the DSP connector board.

For protection of the stator windings from very high current, over-current protection circuit has been designed so as to inhibit the gating signals to all the phases when any one phase current reaches the peak value (set by the designer). Here, the peak current is set at 15 A. In order to avoid high frequency chattering of phase current when it reaches the peak value, the standard Schimtt-type hysteresis control strategy has been incorporated into the protection circuit.

1.5.7 Loading System

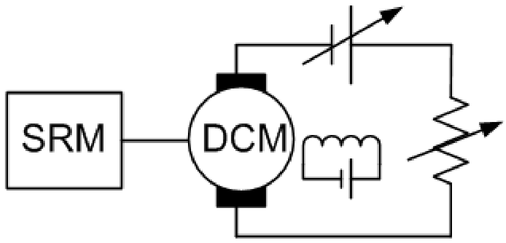

Figure 1.9: DC machine based loading mechanism for the SRM platform

A separately excited DC machine in series with an additional variable DC power supply and a resistive load bank act as load on the SRM, as shown in Fig.1.9. The additional DC supply is required at low speed, as the DC generator voltage output will be quite small to apply the desired load on the system. The variable DC supply voltage allows smooth variation of load on the system.

1.5.8 Torque Transducer

A torque transducer is required for measurement of static torque value at different values of rotor position and phase current. The torque data is used to validate the torque model obtained from flux-linkage model. Such torque estimator is used for feedback in closed-loop torque control schemes. The specifications of the torque transducer are provided in Table 1.3.

As such torque transducers have a slow-bandwidth and hence can not be used for measurement of torque ripples. Due to their inherent flexibility, torque transducers may reduce the resonance frequency drastically and hence should not be used in high-bandwidth applications.

Table 1.3: Specifications of the Torque Transducer

Make	S. Himmelstein & Co.
Model	MCRT 49001V(5-1)-C-F-A-150000
Torque Range	5.65 Nm
Torque Overload	22.6 Nm
Maximum Speed	15000 rpm
Measurement bandwidth	DC to 500 Hz

1.6 Organization of the Thesis

Chapter 1 has introduced the background of thesis work. Basic operation of SRM is explained. The problem of torque ripples and their causes have been identified. Motivation for this research has been stated. A brief review of past work has been provided to show the state-of-the-art. Contributions of the thesis work have been listed. The prototype SRM and the experimental setup are described.

Chapter 2 discusses issues of SRM modelling. Details on static flux-linkage and torque measurement are provided. An analytical flux-linkage model is developed from measured flux-linkage data. The torque model derived from flux-linkage model is validated with the measured torque data.

The issues of choosing an optimal torque sharing function are discussed in Chapter 3. The motor demanded torque is first distributed among two active phases through the torque sharing function. An optimal torque sharing function is chosen according to some performance criteria. Detailed design steps are provided for obtaining various parameters of the TSF used in this work.

Chapter 4 shows the application of ILC in torque-to-current conversion. Conventional indirect torque control schemes use the memory intensive look-up tables for torque-to-current conversion. A novel ILC based current compensation is added to the current reference obtained by assuming a linear magnetization characteristics. The learning gains for ILC are obtained from the phase inductance values at aligned and unaligned rotor positions, when motor would be in linear magnetic region. Without using any detailed nonlinear model, ILC gives excellent average torque control with quite low torque ripples.

Chapter 5 elaborates the control methods for tracking the phase current references accurately. Various methods for this as reported in the literature are discussed. An ILC based current controller is developed to track the phase current references accurately for applications where the motor demanded torque and speed are constant. A sliding mode control (SMC) based current controller is used when phase current references are not periodic but are differentiable. Combining the ILC based torque-to-current conversion with an ILC based current controller, an accurate indirect torque controller scheme is developed. Experimental results are provided to validate the fully ILC based indirect torque controller.

In Chapter 6, a direct torque control scheme is developed, which uses only one ILC and hence is easier to design and implement. Torque model developed in chapter 2 is used for torque feedback. Iterative learning control updates the phase voltage by an amount equal to the product of the learning gain and the phase torque tracking error. As the phase torque reference is periodic in rotor position, the ILC scheme is developed and implemented in rotor position. This removes the constraint of constant speed operation. To improve the robustness of the scheme further, a zero-phase low-pass filter is designed and implemented. Experimental validation of the proposed spatial ILC based DTC scheme is provided. It is found that for constant motor demanded torque level, the peak-to-peak torque ripples can be reduced to within 10% of average torque, for operation up to the rated torque with motor speed around 200 r min.

Chapter 7 introduces the nonlinear robust tracking controller (NLRTC) for direct torque control scheme for SRM. This DTC scheme is useful for application involving position control or speed control, where the torque demand is time-varying. A nominal model is obtained from available flux-linkage data. The proposed scheme uses a variable-gain feedback controller which achieves smooth torque output in a robust manner. The details for the controller design are provided. Finally experimental results are provided to validate the proposed scheme.

Chapter 8 concludes the thesis. It briefly states the focus areas and then discusses the proposed solutions. It also lists the possible future work in this line.

1.7 Summary

This chapter introduces the problem of torque ripples in SRM drives and explains the motivation for the thesis work. The principles of operation and the causes of torque ripples are described. A literature survey on the past work in this area is provided. The main contribution of this thesis are then listed. The structure of this thesis is provided along with the focus area of each chapter. The experimental platform used for validating the proposed control schemes is described. The next chapter elaborates on SRM modelling.

Chapter 2

SRM Modelling

It is essential to have a good understanding of the plant being controlled. Control design is often preceded by modelling of the plant. Representation of the dynamic relationship between plant's input and output in a mathematical form leads to convenience of analysis and controller design. SRM flux-linkage and torque are highly nonlinear function of phase current and rotor position. Various proposals have been reported in the literature for flux-linkage modelling. Torque model is derived from the flux-linkage model using the principle of co-energy. However, an analytical model for flux-linkage has not yet been established which can lead to an accurate torque model. In this chapter, novel polynomial based modelling has been proposed for flux-linkage. This modelling technique has been found to be quite accurate in capturing the flux-linkage, instantaneous torque, incremental inductance and other parameters. As compared to exponential or trigonometric functions, polynomials require less computation and hence suitable for real-time controller implementation.

Variable speed electric drives can be represented by two subsystems: electromagnetic and mechanical. Usually, the mechanical subsystem is much slower than the electromagnetic subsystem. This is particularly true for small and medium sized motors [14]. The two subsystems, can be analyzed and designed independently. This simplifies the control design task. The dynamics of the mechanical subsystem can be represented by the following equations:

$$\frac{d\theta}{dt} = \omega \tag{2.1}$$

$$J\frac{d\omega}{dt} = T_e - T_l - B\omega \tag{2.2}$$

where,

$$\begin{array}{lll} \theta & - & \text{Rotor position in } rad \\ \omega & - & \text{Motor speed in } rad/sec \\ J & - & \text{Total inertia as seen from rotor in } Kg.m^2 \\ T_e & - & \text{Motor torque in } N.m \\ T_l & - & \text{Load torque in } N.m \\ B & - & \text{Friction constant } N.m/(rad/sec) \end{array} \tag{2.3}$$

The motor torque is the sum of phase torques:

$$T_e = \sum_{j=1}^{4} T_j \tag{2.4}$$

where T_j is the torque produced by the j^{th} phase. Accurate and ripple-free motor torque production requires that phase torque references, obtained from the torque sharing function are realized accurately. This thesis work focuses on accurate phase torque tracking. For convenience, phase torque will be referred by T, and phase current by i, *i.e.* without any subscript.

The torque produced by each phase winding is a function of the phase current or flux-linkage and rotor position as $T(i(t), \theta(t))$ or $T(\psi(t), \theta(t))$. Hence, phase torque can be controlled indirectly, by controlling phase current or phase flux-linkage. In the popular 'indirect torque control' (IDTC) scheme, each phase torque reference is first converted to an equivalent phase current reference and then current controllers track the current references accurately.

For the electromagnetic subsystem if IDTC scheme is used, then phase voltage is the system input and phase current or phase flux-linkage is the system output. The dynamic relationship between phase voltage and flux-linkage is shown in (2.5):

$$\frac{d\psi}{dt} = v - iR \tag{2.5}$$

Phase current dynamics can be obtained by expanding (2.5) as:

$$\frac{d\psi}{dt} = \frac{\partial\psi}{\partial i}\frac{di}{dt} + \frac{\partial\psi}{\partial\theta}\frac{d\theta}{dt} \tag{2.6}$$

$$\frac{di}{dt} = \left(\frac{\partial\psi}{\partial i}\right)^{-1}\left(v - iR - \frac{\partial\psi}{\partial\theta}\frac{d\theta}{dt}\right) \tag{2.7}$$

When compared with a the nonlinear dynamic system of the form

$$\dot{x_1} = f_1(x_1, t) + b_1(x_1, t)\, u_1 \tag{2.8}$$

the current dynamics gives:

$$\begin{aligned} x_1 &= i \\ f_1 &= \left(\frac{\partial\psi}{\partial i}\right)^{-1}\left(-iR - \frac{\partial\psi}{\partial\theta}\frac{d\theta}{dt}\right) \\ b_1 &= \left(\frac{\partial\psi}{\partial i}\right)^{-1} \\ u_1 &= v \end{aligned} \tag{2.9}$$

For 'direct torque control' (DTC) scheme, SRM phase torque is the system output. The system dynamics can be expressed by following equations:

$$\frac{dT}{dt} = \frac{\partial T}{\partial i}\frac{di}{dt} + \frac{\partial T}{\partial\theta}\frac{d\theta}{dt} \tag{2.10}$$

By substituting $\frac{di}{dt}$ from (2.7), we get:

$$\frac{dT}{dt} = \left(\frac{\partial T}{\partial i}\right)\left(\frac{\partial\psi}{\partial i}\right)^{-1}\left(-iR - \frac{\partial\psi}{\partial\theta}\frac{d\theta}{dt}\right) + \frac{\partial T}{\partial\theta}\frac{d\theta}{dt} + \left(\frac{\partial T}{\partial i}\right)\left(\frac{\partial\psi}{\partial i}\right)^{-1} v \tag{2.11}$$

By writing in the general form for nonlinear dynamics, we get:

$$
\begin{aligned}
x_2 &= T \\
f_2 &= \left(\frac{\partial T}{\partial i}\right)\left(\frac{\partial \psi}{\partial i}\right)^{-1}\left(-iR - \frac{\partial \psi}{\partial \theta}\frac{d\theta}{dt}\right) + \frac{\partial T}{\partial \theta}\frac{d\theta}{dt} \\
b_2 &= \left(\frac{\partial T}{\partial i}\right)\left(\frac{\partial \psi}{\partial i}\right)^{-1} \\
u_2 &= v
\end{aligned}
\tag{2.12}
$$

The phase torque reference is time-varying. Hence, phase torque control is a nonlinear tracking control problem. Tracking control performance can be improved using model-based feed-forward compensation. Calculation of f and b in either torque control scheme require knowledge of $\psi(i, \theta)$ and $T(i, \theta)$. Hence, this chapter focuses on obtaining these models.

2.1 Flux-linkage modelling

Modelling any plant or process can be done either from the basic laws of physics or from measured data followed by curve fitting. For SRM, the nonlinearity in magnetization characteristics arises from flux fringing and core saturation, which can not be modelled from first principle. Hence, a common approach taken by most researchers is to measure the flux-linkage at different phase current and rotor positions and use regression techniques. It is also essential to validate the flux-linkage model by matching the torque model derived from the flux-linkage model. For this, measured torque data is required. Static torque data is obtained by measuring torque value at different current with rotor being locked in position. Following subsection discuss the measurement methods for flux-linkage and static torque.

2.1.1 Measurement of Flux-linkage under Static Condition

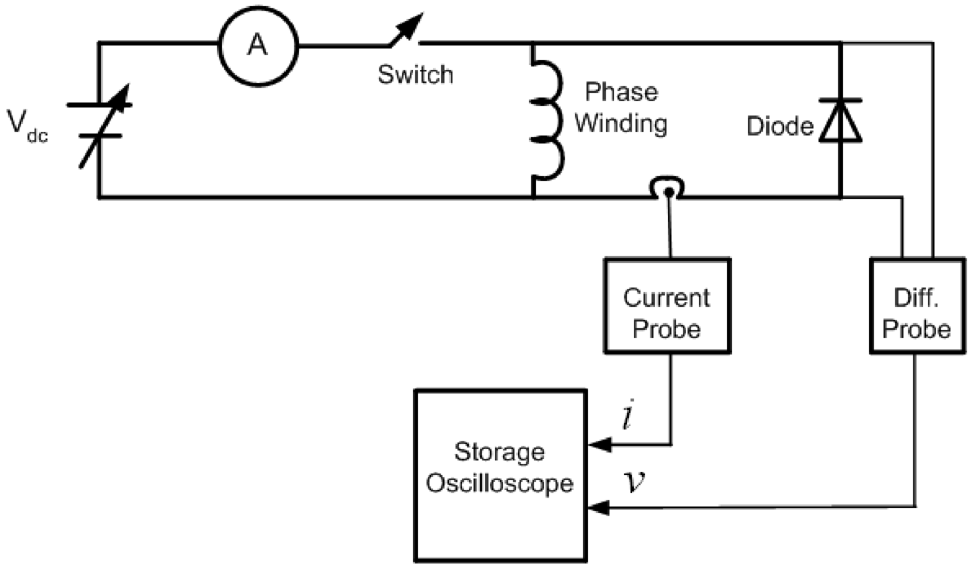

Figure 2.1: Schematic of the setup for phase flux-linkage measurement

Phase flux-linkage is measured at various rotor positions and current levels for the prototype motor. It is assumed that all the phase windings are identical and any mutual coupling between windings is negligible. The rotor is locked in position while making the measurements for different values of phase current. The schematic diagram of the flux-linkage measurement system is given in Fig.2.1. A MOSFET is used as a switch to ensure fast and accurate switching. With the switch closed, the DC supply voltage is increased slowly until the required current flows in the phase winding. Thereafter, when the switch is opened, the energy stored in the winding is dissipated as heat in the phase winding resistance and through the freewheeling diode. A differential probe is used to measure the voltage across the winding and a current probe is used for current measurement. The current and voltage values are stored using a digital storage oscilloscope. Flux-linkage at a given rotor position is estimated for the initial current value, through numerical

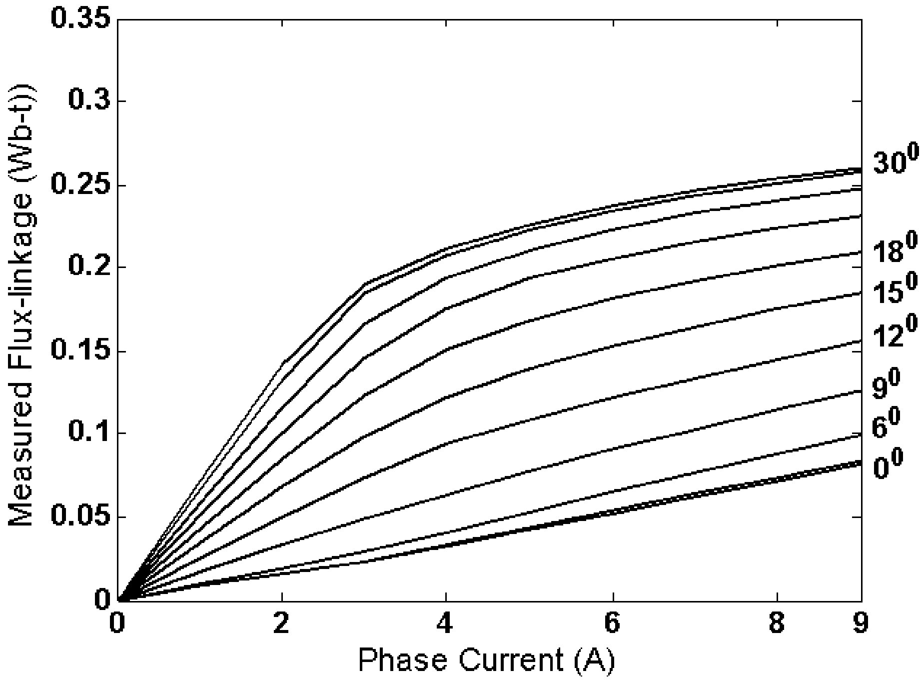

Figure 2.2: Measured flux-linkage data on prototype SRM. Each curve shows the flux-linkage for a given rotor position at different phase currents

integration as given in following equation,

$$\psi(i, \theta) = -\int_0^{t_s} (v - iR)dt \tag{2.13}$$

where $t = 0$ corresponds to the time of opening the switch (current having the maximum value) and t_s corresponds to time when current reaches zero, v is the voltage across the phase winding (the forward voltage drop of the free-wheeling diode), i is the current in the phase winding and R is the resistance of the phase winding. The negative sign is used on the right hand side of the equation as change in flux-linkage would be negative when current decays to zero. The measurements were taken at position intervals of 1^0 between unaligned and aligned position, and at current intervals of $1\,A$ up to $9\,A$. As indicated in [43], there could be errors from, 1) movement of rotor due to application of very large torques, 2) effect of numerical integration method, 3) variation of phase winding resistance due to change

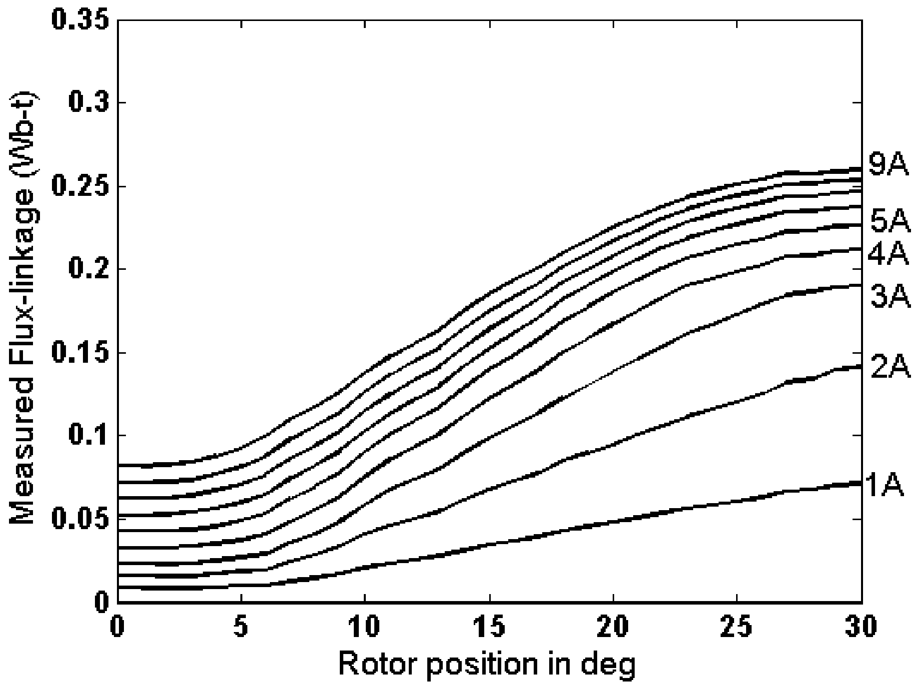

Figure 2.3: Measured flux-linkage data on prototype SRM. Each curve shows the flux-linkage for a given current at different rotor positions

in winding temperature, and 4) due to eddy current losses while current is rising or falling. In this work, an optical encoder has been used to obtain an accurate recording of the rotor position during the measurement. The digital oscilloscope was set to a high sampling frequency of $50\,kHz$, to improve the accuracy of numerical integration over the sampled data. The effect of temperature variation is reduced by having about fifteen-minute gaps between consecutive recordings. To reduce the random errors in measurement, average of three different measurements was taken.

Fig.2.2 shows the measured flux-linkage for the phase winding as a function of phase current at different rotor positions. Fig. 2.3 shows the same flux-linkage as a function of rotor position at different values of phase current. The highly nonlinear variation of the flux-linkage with phase current and rotor position can be seen from these figures. The phase inductance at any rotor position and phase current can be calculated from the flux-linkage measurement, using equation $L(i, \theta) = \frac{\psi(i,\theta)}{i}$. Fig.2.4 shows plot of L vs. rotor position. It can be seen that at higher currents, the magnetic saturation leads to a drop in effective inductance.

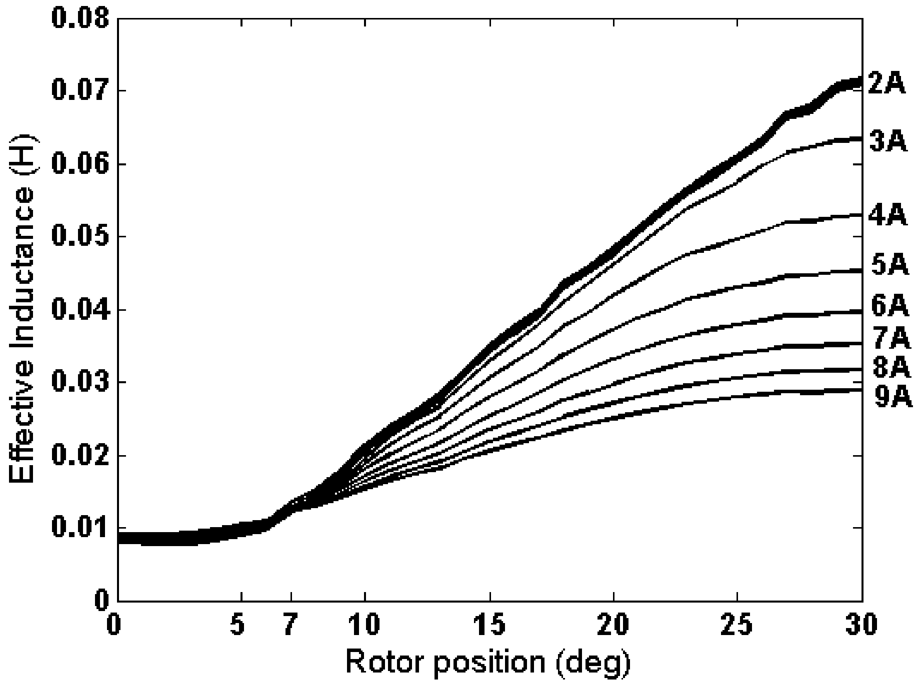

Figure 2.4: Phase inductance estimated from flux-linkage data. Each curve shows the inductance for a given current at different rotor positions.

2.1.2 Measurement of Torque under Static Condition

For SRM torque modelling, we need to obtain the motor torque value at different phase currents and rotor positions. Torque can be measured under static condition if a fixed current is established in the motor winding while rotor is locked in position. In the laboratory setup, a strain-gauge type torque transducer has been used with detailed specifications listed in Table-1.3. An optical encoder had been attached to one end of the motor, which displays the rotor position accurately. A locking

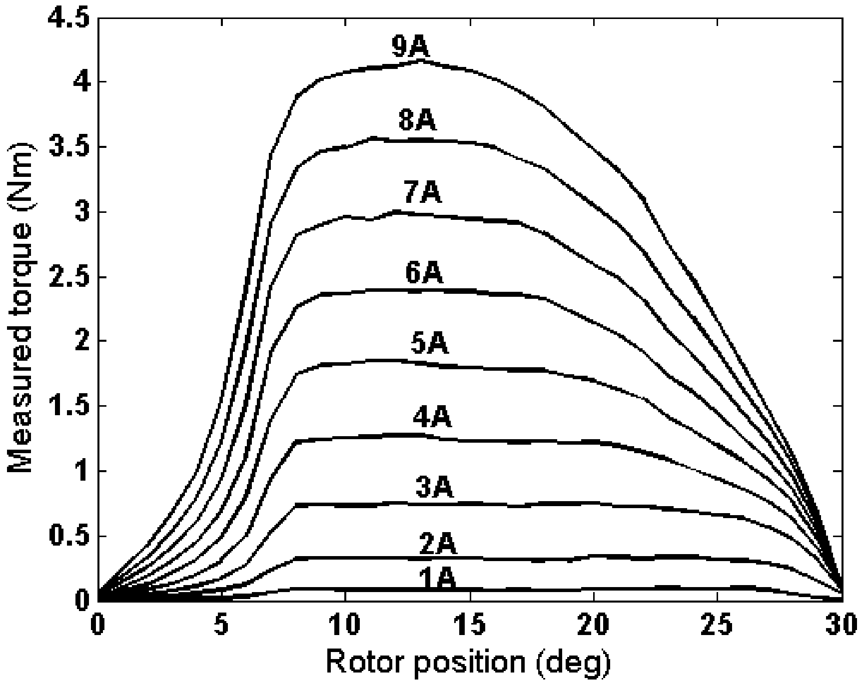

Figure 2.5: Measured phase torque data with rotor locked in position. Each curve shows the torque for a given current at different rotor positions

disc has been installed after the torque transducer for fixing the rotor position at every 1^0 over about 60^0. A variable DC supply was used to supply currents from $1\,A$ to $9\,A$ at an interval of $1\,A$.

Static torque data is shown in Fig.2.5. Each curve shows the phase torque at the specified phase current at different rotor positions. It can be seen that torque has a highly nonlinear relationship with phase current and rotor position.

2.1.3 Past Work on Flux-linkage Modelling

As can be seen from Figs.2.2 and 2.3, the flux-linkage is a highly nonlinear mapping of phase current and rotor position. This poses a major challenge, and also provides possibility for numerous alternative functions and methods in finding a prospective model.

Cubic spline functions had been used in [44] for capturing the experimentally measured flux-linkage data. Spline functions are regionally valid and often used for predicting values near experimental data points. Flux-linkage values for one rotor position over the range of current values have been interpolated with cubic spline functions. The four coefficients of the cubic spline are obtained for each segment(a set of three consecutive points) with the constraints that; 1) the predicted data at the three points match with the input data, and 2) the first derivative at the start point of each segment is equal to the first derivative at the end point of the previous segment. The first derivative at the start of the first segment is zero. Then, co-energy at any current levels, for the given rotor position, is obtained through integration of the cubic functions. The variation of co-energy with rotor position, is captured by another spline function. The coefficients of the bi-cubic spline interpolation are stored in matrix array. Motor torque is estimated from partial derivative of these bi-cubic spline functions representing co-energy with respect to rotor position. The other dynamic quantities like incremental inductance ($\frac{\partial\psi}{\partial i}$) of phase windings and back-emf constant ($\frac{\partial\psi}{\partial\theta}$), can be calculated from derivative of the spline functions for flux-linkage. However, cubic splines fit the measured data exactly. Thus, any noise in measurement will enter into the modelling and will lead to large deviation in estimation of the dynamic quantities, which are obtained through differentiation.

Other approach is to find a globally valid analytical relationship to capture the flux-linkage as a function of rotor position and phase current. This is motivated by the promise of compactness and ease of deriving the other dynamic quantities like instantaneous torque. Numerous analytical models have been proposed for the flux-linkage.

Torrey *et al.* in [45] have reported such a compact model as:

$$\psi(i, \theta) = a_1(\theta)\left(1 - e^{a_2(\theta) \times i}\right) + a_3(\theta) \times i \tag{2.14}$$

where $a_1(\theta), a_2(\theta)$ and $a_3(\theta)$ are different for different rotor positions. This model was first proposed by Taylor *et al.* in [46]. For a given rotor position, a_1, a_2 and a_3 are obtained through nonlinear regression in the flux-linkage data for different current levels. The variation of these three coefficients over rotor position is periodic and hence was expressed as a truncated Fourier series. This model predicts the flux-linkage quite accurately. However, the instantaneous torque prediction derived from this flux-linkage model contains high frequency errors due to the presence of high frequency sinusoids of the Fourier series. In [47], Torrey *et al.* have proposed to represent the parameters of the above mentioned model, as piecewise linear functions of rotor position. The resulting model, though simple and captures the flux-linkage data accurately, has large error in prediction of instantaneous torque.

In [48], Chan *et al.* have proposed the use of a series of exponential functions to approximate the 3D surface of the flux-linkage, current and rotor position mapping. Equation for torque is derived by integration and differentiation of the series of functions. The resultant function is computationally too complex for real-time implementation.

In [49], Mahdavi *et al.* had represented the flux-linkage data in terms of phase inductance. The phase inductance and rotor position relationship in Fig.2.4 for each given current is represented as a truncated Fourier series containing three terms.

The coefficients of these Fourier terms are solved by the phase inductance values at the unaligned position, aligned position and a position midway between these two positions. These Fourier series coefficients are then represented as polynomials in current, to determine the summary equation valid over the complete data space. The authors have used this model for PSPICE simulations but have not shown any comparison with the measured current or torque.

In [50], Stiebler *et al.* have proposed to represent the flux-linkage variation with each rotor position, as shown in Fig.2.3, in terms of the flux-linkage values at the unaligned and aligned position, and a function in rotor position. The flux-linkage at the two extreme positions are functions of current alone. This method gives an acceptable fit for the flux-linkage but the instantaneous torque prediction contains large error.

In [51], Saha *et al.* have divided the operating current range into saturated and unsaturated regions. Each flux-linkage vs current curve is represented as two separate pieces of polynomials in current. The coefficients of these polynomials are truncated Fourier series in rotor position. This approach is good when used for a rotor position sensor-less scheme, but the instantaneous torque prediction is not good enough for high performance torque controller.

As discussed in the preceding paragraphs, there has been enormous interest among the research community for obtaining a suitable model for SRM flux-linkage and torque in terms of phase current and rotor position. The models so far reported are either too complex or not so accurate. In view of this, some investigations have been made in this thesis work for a suitable SRM model, which can lead to an accurate torque estimator. The resultant model can be used in real-time control implementations.

2.2 Exponential Flux-linkage Model

The model (2.14) reported in [45] is intuitive as well as compact for flux-linkage modelling. Hence, this model is chosen for further investigation. The coefficients $a_1(\theta), a_2(\theta)$ and $a_3(\theta)$ can be obtained from the flux-linkage vs current curve for a given rotor position as shown in Fig.2.6. The slope of the measured flux-linkage vs current curve at large phase currents is a_3, as the first term in the model would be very small. Thus a_3 is the incremental phase inductance when machine goes into saturation. The coefficient a_1 can be thought of as the flux-linkage after which the motor goes into saturation. The degree of saturation or curvature of the flux-linkage vs current curve at the given rotor position is captured by the coefficient a_2. The values of these coefficients at different rotor positions are obtained by nonlinear regression of each flux-linkage vs current curve at individual rotor positions; and shown in Fig.2.7.

A second step of curve fitting is necessary for representing these coefficients as functions of rotor position. It is worth noting that the plot of the coefficients for rotor positions beyond the aligned position would be mirror images of the plot up to the aligned position. Over one complete rotation, the plot of the coefficients will be periodic, with a period same as the rotor pole pitch. The authors in [45] have proposed use of Fourier series based approximation for the model coefficient functions. Method of least squares was used for curve fitting. It was shown that the

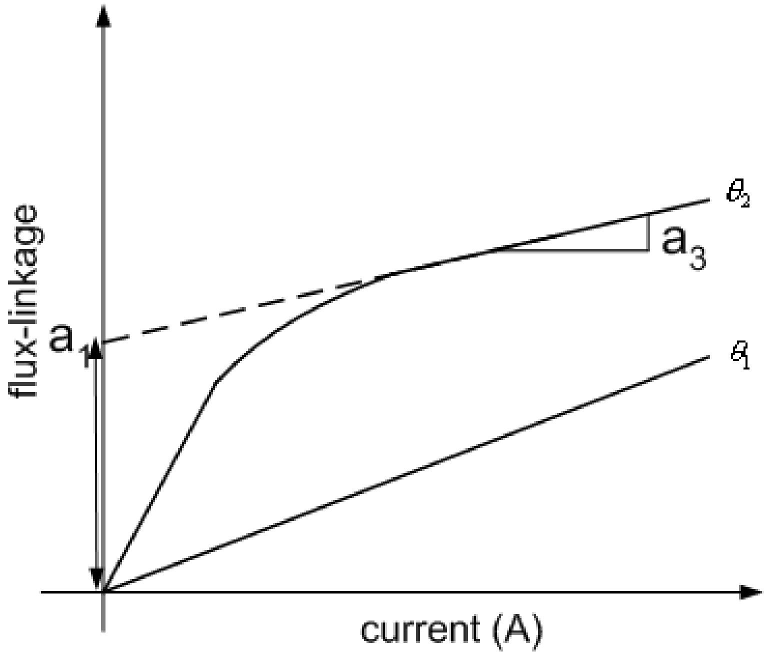

Figure 2.6: Coefficients of the exponential model for phase flux-linkage

flux-linkage matching was quite accurate. Then, the resultant flux-linkage model was used to derive the torque model, as shown in following equation:

$$\begin{aligned} T(i,\theta) &= \{i + \frac{1}{a_2(\theta)}(1 - e^{a_2(\theta)i})\}\frac{da_1}{d\theta} - \\ &\{\frac{a_1(\theta)}{a_2(\theta)^2}(1 - e^{a_2(\theta)i}) + \frac{a_1(\theta)i}{a_2(\theta)}e^{a_2(\theta)i}\}\frac{da_2}{d\theta} + \frac{1}{2}i^2\frac{da_3}{d\theta} \end{aligned} \tag{2.15}$$

However, the torque prediction from this torque model is not accurate. As can be seen in (2.15), the expression for the instantaneous torque contains derivatives of the coefficient functions $a_1(\theta), a_2(\theta)$ and $a_3(\theta)$. The presence of high frequency components in the Fourier series approximating the coefficient functions cause their derivatives to have large amount of error in prediction, as shown in [52] reproduced in Fig.2.8. Hence, a fairly good approximation of the model parameters at different rotor positions in a sense of least squared error in flux-linkage ensures good prediction for the flux-linkage, but not the instantaneous torque.

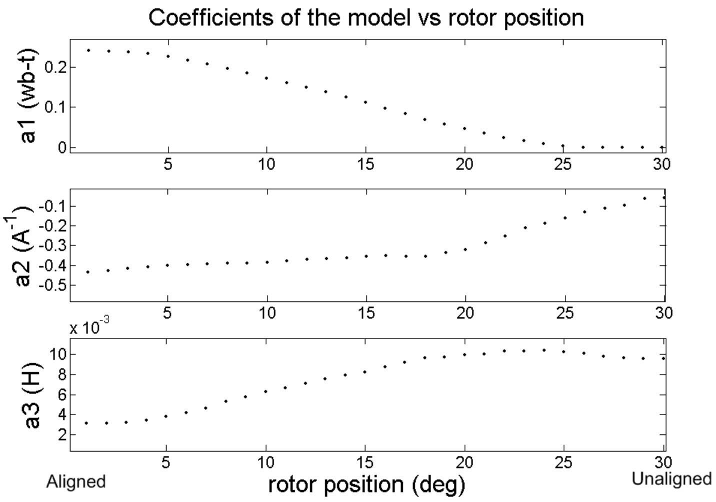

Figure 2.7: Coefficients of the exponential model obtained at discrete rotor positions

2.2.1 Polynomials for the Coefficients

As suggested in [45], there could be other ways like splines for representation of the model parameters as functions of rotor position. Splines are localized polynomials and defined separately for each rotor position interval and can represent any data accurately. In this work, use of cubic splines for the coefficients $a_1(\theta)$, $a_2(\theta)$ and $a_3(\theta)$ in (2.14) has been investigated. It has been found that such method leads to high frequency prediction error for instantaneous torque. This finding also indicates that the fitting functions for the model parameters should be as smooth as possible, in addition to matching their values at discrete rotor positions. Hence, single polynomials valid over the complete range of rotor positions have been used for fitting these coefficients. Starting with third order polynomials, the order has been slowly increased to improve the fitting. The fitting by polynomials of various orders are shown in Figs.2.9-2.11 for the three coefficients. Lower order polynomials lead to large error. However, a high order polynomial incurs more computation and leads to high frequency oscillations as in case of Fourier series approximation. Although

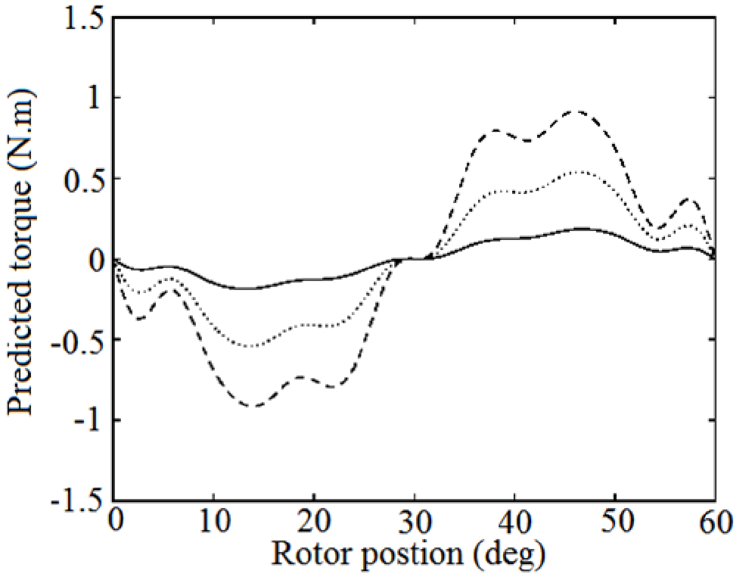

Figure 2.8: Matching of measured static torque with prediction of the torque model derived from exponential flux-linkage model, when variations of model coefficients are approximated using Fourier series

$a_1(\theta)$ could be captured with a third order polynomial, fifth order polynomials were used for all the coefficients for convenience of implementation. These polynomials are expressed below:

$$
\begin{aligned}
a_1(\theta) &= a_{11}\theta^5 + a_{12}\theta^4 + a_{13}\theta^3 + a_{14}\theta^2 + a_{15}\theta + a_{16}, \\
a_2(\theta) &= a_{21}\theta^5 + a_{22}\theta^4 + a_{23}\theta^3 + a_{24}\theta^2 + a_{25}\theta + a_{26}, \\
a_3(\theta) &= a_{31}\theta^5 + a_{32}\theta^4 + a_{33}\theta^3 + a_{34}\theta^2 + a_{35}\theta + a_{36}.
\end{aligned}
$$

The torque prediction when polynomials are used for capturing the coefficients, is shown in Fig.2.12. There are no oscillations in torque prediction. A possible explanation for this is: the torque depends on the rate of change of derivative of the flux-linkage with respect to rotor position. However, the fitting is still not quite accurate near the region where the torque-vs-position curve changes a fast rate. We may conclude from above findings that the method of least square error fitting on flux-linkage data does not automatically result in an accurate torque estimator.

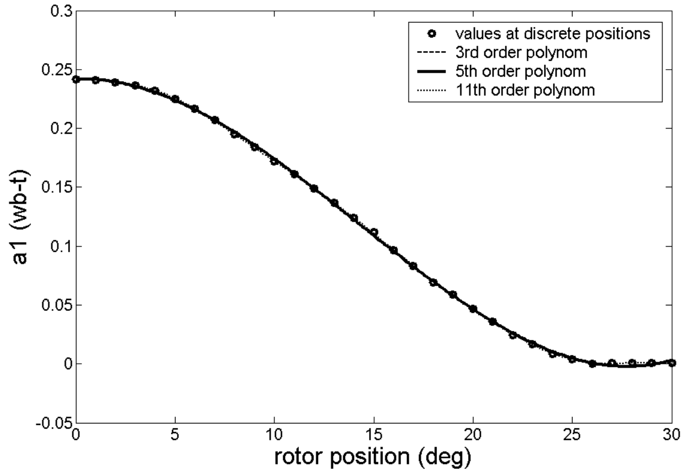

Figure 2.9: Curve-fitting of $a1$ with polynomials

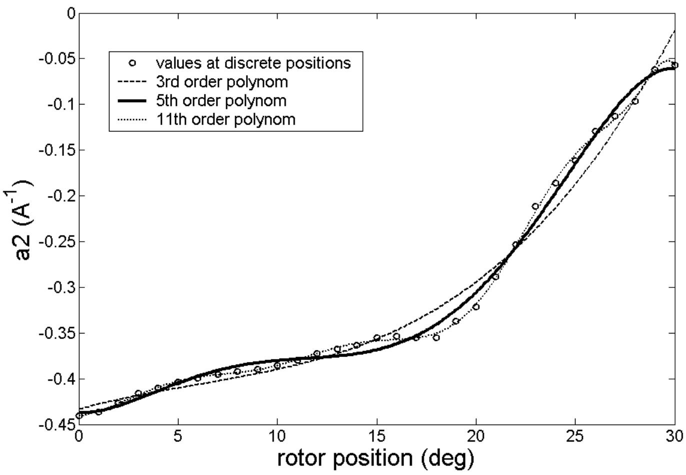

Figure 2.10: Curve-fitting of $a2$ with polynomials

2.2.2 Direct Curve Fitting of Static Torque Data

As discussed in previous section, the torque model derived from flux-linkage model is not accurate. The predicted torque data does not match the static measured torque data. However, the expression for torque in (2.15) can be used to obtain an analytical torque model, independent of the flux-linkage data. This would be useful for online torque feedback. The parameters of (2.15) can be obtained by

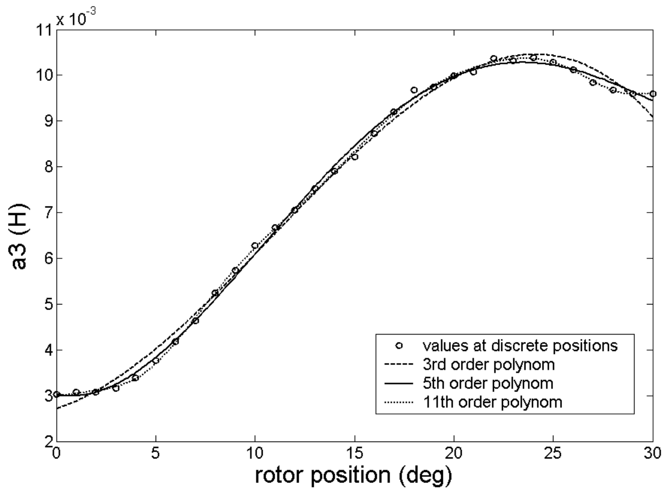

Figure 2.11: Curve-fitting of $a3$ with polynomials

least-square error fitting of the measured torque data directly.

The cost function for the least-square error fitting is defined as:

$$J =_{c \in C}^{min} \{\sum_{i=1}^{N} (T_m(i) - T_e(i))^2\} \tag{2.16}$$

where T_m is the measured torque data and T_e is the corresponding estimated torque data, and

$$\begin{aligned} c &= \{a_{i1}, a_{i2} ... a_{i6}\} \; i = 1, 2, 3 \\ C &= (-\infty, \infty) \bigcap (-\infty, \infty) \bigcap ... \bigcap (-\infty, \infty) \end{aligned}$$

The cost function in (2.16) is highly nonlinear in the parameter space, with many local minima. Levenberg-Marquadt (LM) gradient-expansion method [54] has been used for obtaining the solutions. As LM method is highly sensitive to the initial values, first Genetic Algorithm (GA) has been used to enter the neighborhood containing the best solution. Then, LM method is used to refine the search for the best solution. The final value of the cost function after the LM search was found to be $3.9927E - 3$. The instantaneous torque predicted by the resultant model is shown to be in good match with the measured data as shown in Fig.2.13.

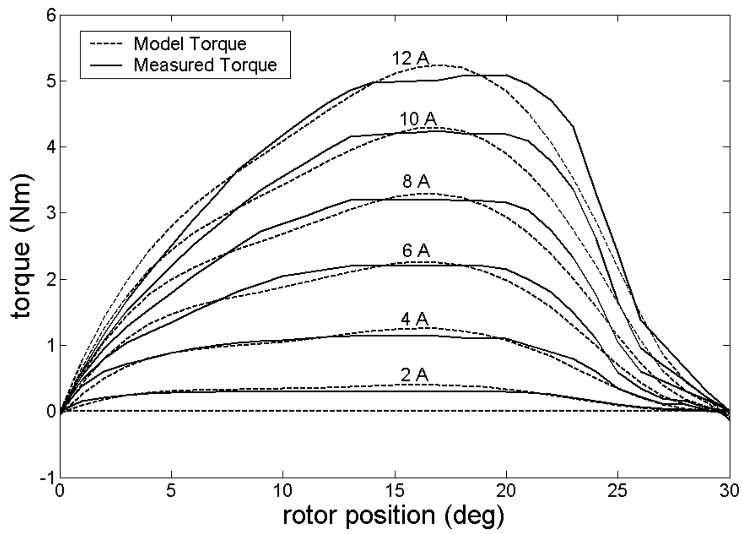

Figure 2.12: Matching of measured static torque with prediction of the torque model derived from exponential flux-linkage model, variations of model coefficients are fitted with polynomials.

It is important to note that there will be two sets of values for the coefficients, one set for the flux-linkage model and the other for the torque model. Moreover, the original purpose of being able to obtain the dynamic properties from the flux-linkage model is not achieved. This is the motivation for further research work on SRM modelling. A novel solution has been found for this problem, as described in the following section.

2.3 Proposed Polynomial Based Modelling

Torrey's exponential model for flux-linkage needs nonlinear regression as it is nonlinear in parameters. Nonlinear curve fitting method like Levenberg-Marquadt's [54] is complex. The final values of the model parameters are sensitive to the choice of initial values. Thus, it would be preferable to use a nonlinear model which is linear in parameters, *eg.* Fourier series or polynomials.

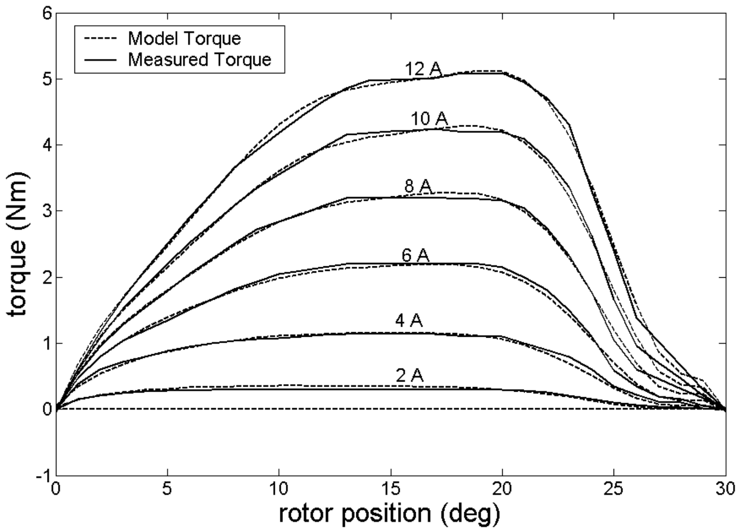

Figure 2.13: Matching of measured static torque with prediction of the torque model obtained by directly curve-fitting of measured torque data. Only torque expression is derived from the exponential flux-linkage expression.

Fourier series is used for curve fitting due to the periodicity of SRM characteristics along the rotor position. However, a good fit may require as large as ten Fourier terms. Computation of the sine and cosine terms is time-consuming for real-time implementations. A novel approach based on polynomials is proposed for capturing the flux-linkage and static torque data.

It was observed [53] that instead of having a single model to be valid globally, piece-wise modelling techniques can be used to fit simpler models. However, if some insight is used to suitably divide the complete range into smaller regions, then very simple function like low-order polynomials can provide accurate fitting.

2.3.1 Division into Four different Regions

The flux-linkage variation between unaligned and aligned rotor positions for constant current values is given in Fig.2.3. Due to the small air gap in SRM, there is a large degree of flux-fringing near the unaligned rotor position. As overlapping increases, flux-fringing decreases and the effect of saturation creeps in. This phenomenon is clearly visible from calculated 'effective inductance' (flux-linkage/phase current) variation in Fig.2.4. In the beginning, the effective inductance variation is almost independent of phase current and increases slowly with rotor position. As rotor gets away from unaligned position, the rate of rise of effective inductance keeps increasing till it becomes constant. The rotor position after which the rate of rise becomes constant, can be taken as the boundary point for the two regions described earlier. This rotor position will be referred as θ_h.

Variation of phase flux-linkage with phase current can be seen in Fig.2.2. For any rotor position, the flux-linkage varies linearly with phase current up to certain current limit, where the core is said to be in the linear region. As phase current increases further, the effect of saturation creeps in. Thus, variation of the SRM characteristics along phase current can be divided into two regions hinged at a value after which saturation effect becomes visible for any rotor position. This value of phase current will be referred as i_s.

This way the total operating range is divided into four regions as shown in Fig.2.14. This physical understanding of the magnetization characteristics of SRM is used in the proposed flux-linkage modelling.

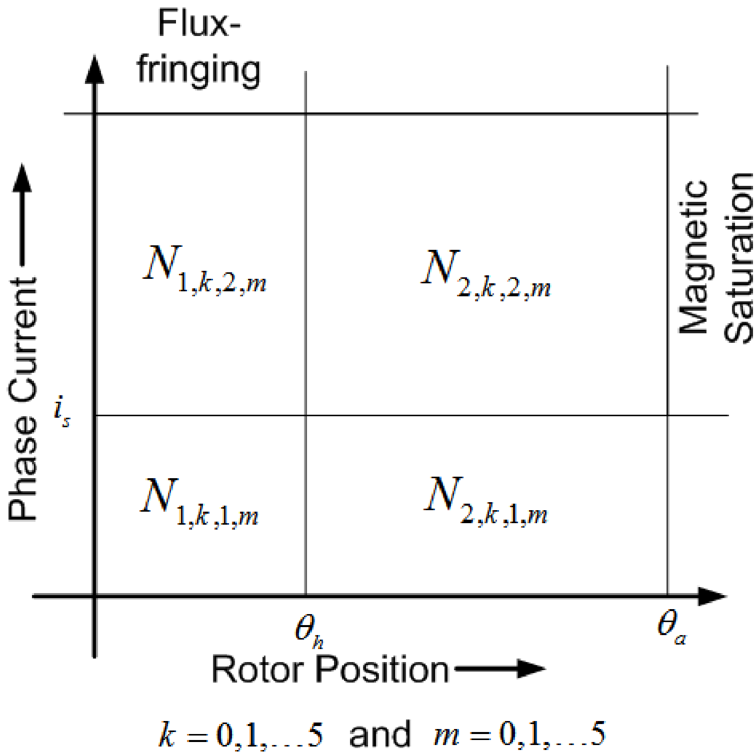

Figure 2.14: Division of the space in phase current and rotor position into four different regions. Each region has a unique polynomial model for flux-linkage

2.3.2 Choice of Polynomial Degree

The variation of effective inductance in the two regions of rotor position for a constant current is captured by two polynomials, hinged at a point that lies at the boundary of the two regions. The required degree of the polynomials depends on the degree of nonlinearity of the underlying data. A higher-degree polynomial may lead to an oscillatory fitting. At first, third order polynomials were tested, but were found to be less accurate. Finally, fifth order polynomials were found to be accurate and smooth enough for the measured data. Two fifth order polynomials in rotor position are obtained for the flux-linkage data for a given current value. The set of polynomials for all the different current values are generated. Each polynomial coefficient (there are six coefficients for each fifth order polynomial) will be different for different current value. This variation of each coefficient over the range of phase current is captured again by two fifth-order polynomials: one for the low current region and the other for high current region. This is shown in the following equations.

Flux-linkage is defined as $\psi(i,\theta) = L_e(i,\theta)\, i$, where $L_e(i,\theta)$ is the effective phase inductance. Then, $L_e(i,\theta)$ is captured using the polynomial as:

$$\begin{aligned} L_e(i,\theta) &= \sum_{k=0}^{5} M_{1,k}(i)\, \theta^k \text{ for } 0 \le \theta \le \theta_h \\ &= \sum_{k=0}^{5} M_{2,k}(i)\, \theta^k \text{ for } \theta_h \le \theta \le \theta_a \end{aligned} \tag{2.17}$$

$$\begin{aligned} M_{1,k}(i) &= \sum_{m=0}^{5} N_{1,k,1,m}\, i^m \text{ for } 0 \le i \le i_s \\ &= \sum_{m=0}^{5} N_{1,k,2,m}\, i^m \text{ for } i_s \le i \le 9 \\ & \quad \text{for } k = 0, 1, ..5 \end{aligned}$$

$$\begin{aligned} M_{2,k}(i) &= \sum_{m=0}^{5} N_{2,k,1,m}\, i^m \text{ for } 0 \leq i \leq i_s \\ &= \sum_{m=0}^{5} N_{2,k,2,m}\, i^m \text{ for } i_s \leq i \leq 9 \\ &\quad \text{for } k = 0, 1, ..5 \end{aligned} \tag{2.18}$$

The complete equation for the effective inductance is:

$$\begin{aligned} L_e(i,\theta) &= \sum_{k=0}^{5}\left(\sum_{m=0}^{5} N_{1,k,1,m}\, i^m\right)\theta^k \text{ for } 0 \leq i \leq i_s \text{ and } 0 \leq \theta \leq \theta_h \\ &= \sum_{k=0}^{5}\left(\sum_{m=0}^{5} N_{2,k,1,m}\, i^m\right)\theta^k \text{ for } 0 \leq i \leq i_s \text{ and } \theta_h \leq \theta \leq \theta_a \\ &= \sum_{k=0}^{5}\left(\sum_{m=0}^{5} N_{1,k,2,m}\, i^m\right)\theta^k \text{ for } i_s \leq i \leq i_{max} \text{ and } 0 \leq \theta \leq \theta_h \\ &= \sum_{k=0}^{5}\left(\sum_{m=0}^{5} N_{2,k,2,m}\, i^m\right)\theta^k \text{ for } i_s \leq i \leq i_{max} \text{ and } \theta_h \leq \theta \leq \theta_a \end{aligned} \tag{2.19}$$

The complete model for flux-linkage becomes:

$$\begin{aligned} \psi(i,\theta) &= \sum_{k=0}^{5}\left(\sum_{m=0}^{5} N_{1,k,1,m}\, i^{m+1}\right)\theta^k \text{ for } 0 \leq i \leq i_s \text{ and } 0 \leq \theta \leq \theta_h \\ &= \sum_{k=0}^{5}\left(\sum_{m=0}^{5} N_{2,k,1,m}\, i^{m+1}\right)\theta^k \text{ for } 0 \leq i \leq i_s \text{ and } \theta_h \leq \theta \leq \theta_a \\ &= \sum_{k=0}^{5}\left(\sum_{m=0}^{5} N_{1,k,2,m}\, i^{m+1}\right)\theta^k \text{ for } i_s \leq i \leq i_{max} \text{ and } 0 \leq \theta \leq \theta_h \\ &= \sum_{k=0}^{5}\left(\sum_{m=0}^{5} N_{2,k,2,m}\, i^{m+1}\right)\theta^k \text{ for } i_s \leq i \leq i_{max} \text{ and } \theta_h \leq \theta \leq \theta_a \end{aligned} \tag{2.20}$$

The complete flux-linkage data is captured by the 144(2x6x2x6) parameters as mentioned in (2.17) and (2.18). For look-up table based modelling, the flux-linkage data is usually [8] stored at 1^0 interval along rotor position and at $1\,A$ along phase current. Hence, for the prototype motor, the number of memory locations would be 300 over the rotor position range of $0^0 - 30^0$ and phase current range of $0\,A - 9\,A$.

As polynomials are analytical, the incremental phase inductance and back-emf constant are obtained from the flux-linkage model through integration and differentiation. The derivation of back-emf constant follows:

$$\begin{aligned}
\frac{\partial\psi}{\partial\theta}(i,\theta) &= \sum_{k=1}^{5}\left(\sum_{m=0}^{5} N_{1,k,1,m}\, i^{m+1}\right) k\,\theta^{k-1} \text{ for } 0 \le i \le i_s \text{ and } 0 \le \theta \le \theta_h \\
&= \sum_{k=1}^{5}\left(\sum_{m=0}^{5} N_{2,k,1,m}\, i^{m+1}\right) k\,\theta^{k-1} \text{ for } 0 \le i \le i_s \text{ and } \theta_h \le \theta \le \theta_a \\
&= \sum_{k=1}^{5}\left(\sum_{m=0}^{5} N_{1,k,2,m}\, i^{m+1}\right) k\,\theta^{k-1} \text{ for } 0 \le i \le i_s \text{ and } 0 \le \theta \le \theta_h \\
&= \sum_{k=1}^{5}\left(\sum_{m=0}^{5} N_{2,k,2,m}\, i^{m+1}\right) k\,\theta^{k-1} \text{ for } 0 \le i \le i_s \text{ and } \theta_h \le \theta \le \theta_a
\end{aligned} \tag{2.21}$$

Similarly, the incremental inductance can be derived from the flux-linkage model:

$$\begin{aligned}
\frac{\partial\psi}{\partial i}(i,\theta) &= \sum_{k=0}^{5}\left(\sum_{m=0}^{5} (m+1)N_{1,k,1,m}\, i^{m}\right) \theta^{k} \text{ for } 0 \le i \le i_s \text{ and } 0 \le \theta \le \theta_h \\
&= \sum_{k=0}^{5}\left(\sum_{m=0}^{5} (m+1)N_{2,k,1,m}\, i^{m}\right) \theta^{k} \text{ for } 0 \le i \le i_s \text{ and } \theta_h \le \theta \le \theta_a \\
&= \sum_{k=0}^{5}\left(\sum_{m=0}^{5} (m+1)N_{1,k,2,m}\, i^{m}\right) \theta^{k} \text{ for } i_s \le i \le i_{max} \text{ and } 0 \le \theta \le \theta_h \\
&= \sum_{k=0}^{5}\left(\sum_{m=0}^{5} (m+1)N_{2,k,2,m}\, i^{m}\right) \theta^{k} \text{ for } i_s \le i \le i_{max} \text{ and } \theta_h \le \theta \le \theta_a
\end{aligned} \tag{2.22}$$

Using the co-energy principle for reluctance torque, the phase torque model can be obtained from the phase flux-linkage model as:

$$\begin{aligned}
T(i,\theta) &= \sum_{k=1}^{5}\left(\sum_{m=0}^{5} N_{1,k,1,m}\frac{i^{m+1}}{m+1}\right) k\theta^{k-1}(\text{for } 0 \le i \le i_s \text{ and } 0 \le \theta \le \theta_h) \\
&= \sum_{k=1}^{5}\left(\sum_{m=0}^{5} N_{2,k,1,m}\frac{i^{m+1}}{m+1}\right) k\theta^{k-1}(\text{ for } 0 \le i \le i_s \text{ and } \theta_h \le \theta \le \theta_a) \\
&= T_1(i_s,\theta) + \\
&\quad \sum_{k=1}^{5}\left(\sum_{m=0}^{5} N_{1,k,2,m}\frac{i^{m+1}-i_s^{m+1}}{m+1}\right) k\theta^{k-1} \text{ (for } i_s \le i \le i_{max} \text{ and } 0 \le \theta \le \theta_h \\
&= T_2(i_s,\theta) +
\end{aligned}$$

$$\sum_{k=1}^{5}\left(\sum_{m=0}^{5} N_{2,k,2,m}\frac{i^{m+1}-i_s^{m+1}}{m+1}\right)k\theta^{k-1} \text{ (for } i_s \leq i \leq i_{max} \text{ and } \theta_h \leq \theta \leq \theta_a$$

where,

$$\begin{aligned} T_1(i_s,\theta) &= \sum_{k=1}^{5}\left(\sum_{m=0}^{5} N_{1,k,1,m}\frac{i_s^{m+1}}{m+1}\right)k\theta^{k-1} \\ T_2(i_s,\theta) &= \sum_{k=1}^{5}\left(\sum_{m=0}^{5} N_{2,k,1,m}\frac{i_s^{m+1}}{m+1}\right)k\theta^{k-1} \end{aligned} \tag{2.23}$$

The advantage of the proposed modelling method over look-up table is obvious. Only 144 coefficients of the model have to stored in memory. The other quantities like torque, back-emf and incremental inductance can be obtained analytically using the same coefficients. In conventional look-up table method, each dynamic property is estimated off-line and stored in a separate look-up table, thus requiring more on-line memory.

2.3.3 Validation of Polynomial Model with Measured Data

Fig.2.15 shows the measured flux-linkage data(dotted line) vs. rotor position, and the flux-linkage values(+) predicted for different current levels. As can be seen, the proposed polynomial based model captures the flux-linkage data quite accurately. Fig.2.16 shows flux-linkage vs phase current matching at different rotor position. Again the fitting is smooth as well as accurate at the measured data points.

Incremental phase inductance has been estimated from measured flux-linkage as:$L_{est} = \frac{\psi(i_2,\theta)-\psi(i_1,\theta)}{i_2-i_1}$ and compared with that obtained analytically as in (2.22) from the flux-linkage model. Fig.2.17 shows the incremental inductance vs phase current, and Fig.2.18 shows the incremental inductance vs rotor position. This indi-

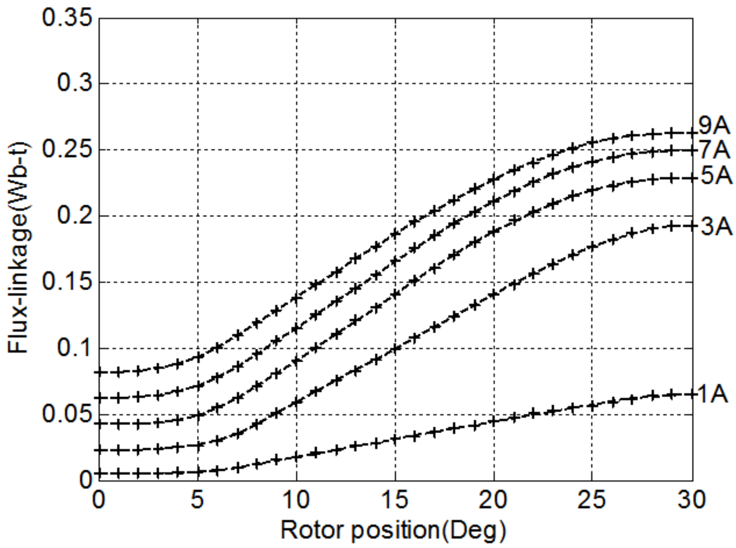

Figure 2.15: Matching of measured flux-linkage versus rotor position curves with the polynomial model predicted flux-linkage vs rotor position curves

cates that proposed polynomial flux-linkage model derived incremental inductance prediction is quite accurate.

One important use of this flux-linkage model is that an accurate torque model can be derived using the co-energy principle. The expression for torque as in (2.23) is used to predict phase torque at the measurement points. Fig.2.19 shows the comparison of measured torque with the predicted torque. There is a very good matching except towards the end regions. Such accurate torque prediction can be for on-line estimation of torque for closed-loop torque control.

2.4 Torque Measurement with a Strain-gauge type Torque Transducer

For closed-loop torque control, feedback of actual torque is necessary. Often, a strain-gauge type torque transducer is used to measure the motor torque. In this

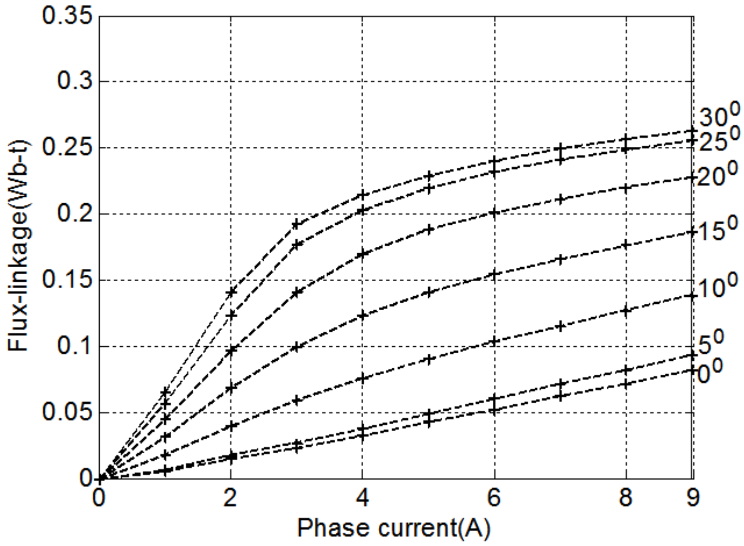

Figure 2.16: Matching of measured flux-linkage vs current curves with the polynomial model predicted flux-linkage vs current curves

work, a DC operated non-contact type (model: MCRT 49001V) is used for measurement of static torque. It will be shown in this section that such a torque transducer can not be used for online torque feedback.

The torque transducer has been installed between SRM and load, as shown in Fig.2.20(a). This arrangement results in a two-mass-spring system as shown in Fig.2.20(b), whose dynamics are given by the following differential equations:

$$\begin{aligned} J_{srm}\frac{d^2\theta_1}{dt^2} + B_{srm}\frac{d\theta_1}{dt} &= T_{srm} - K_{TT}(\theta_1 - \theta_2) \\ J_{dcm}\frac{d^2\theta_2}{dt^2} + B_{dcm}\frac{d\theta_2}{dt} &= K_{TT}(\theta_1 - \theta_2) \end{aligned} \quad (2.24)$$

The effect of this two-mass-spring system on torque measurement has been first shown through simulations, followed by experimental validation. The values of the parameters in (2.24) are given in the Table 2.1. The polynomial torque model obtained in previous section is used for predicting the motor torque from the phase current and rotor position. Simulation results for the torque-transducer system dynamics are given in Fig.2.21, where the solid line shows the estimated motor

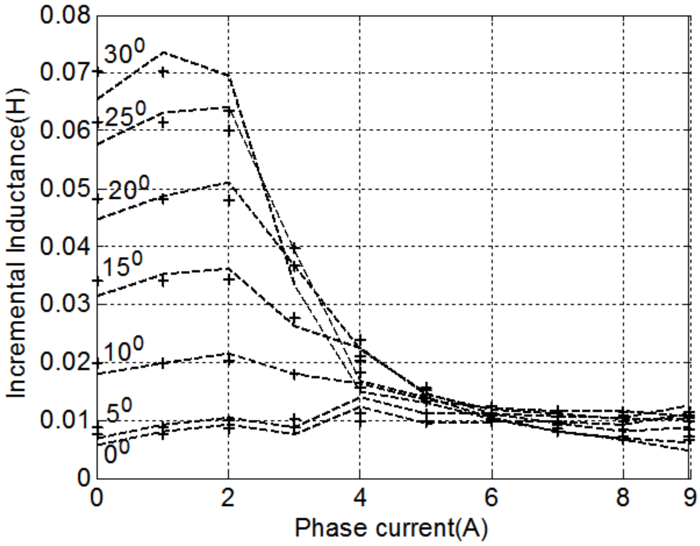

Figure 2.17: Matching of incremental inductance estimated from measured flux-linkage data with the incremental inductance predicted by the incremental inductance model derived from the polynomial flux-linkage model. The curves are plotted vs phase current.

Table 2.1: Parameters of the Mechanical Subsystem used in Simulation

J_{srm}	$5.0\text{x}10^{-4}\, Kg\, m^2$
B_{srm}	$5.0\text{x}10^{-4}\, Nm/rad/sec$
J_{dcm}	$120.0\text{x}10^{-4}\, Kg\, m^2$
B_{dcm}	$30.0\text{x}10^{-4}\, Nm/rad/sec$
K_{TT}	1320 Nm/rad

torque, and the dashed line shows the output of the torque transducer. It can be seen that the torque transducer output contains a high-frequency component superimposed on a low frequency component. The low frequency component matches the estimated motor torque quite well. This was experimentally verified at two different torque levels, as shown in Figs. 2.22 and 2.23. It can be concluded that the torque transducer can be used for DC torque measurement, but can not be used for accurate measurement of torque ripples.

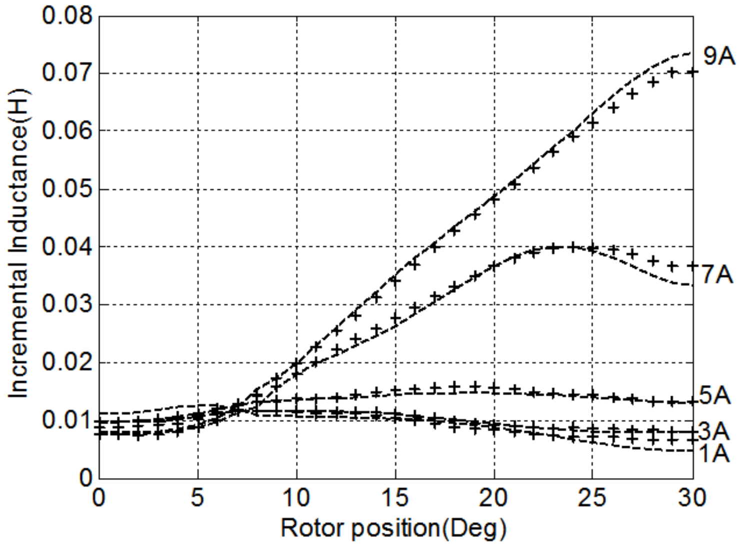

Figure 2.18: Matching of incremental inductance estimated from measured flux-linkage data with the incremental inductance predicted by the incremental inductance model derived from the polynomial flux-linkage model. The curves are plotted vs rotor position.

2.5 Summary

In this chapter, the modelling for SRM was discussed. To start with, a review was done on various flux-linkage modelling techniques for SRM. Some researches used look-up tables for capturing the nonlinear magnetic characteristics in terms of phase current and rotor position. However, this method is not useful for deriving other dynamic properties like incremental inductance and instantaneous torque. Analytical models for flux-linkage are necessary for this. It is also essential that the model should be of less computational complexity, for easy implementation in real-time systems. It was found that the models reported in literature do not satisfy the requirement of accuracy and simplicity. The periodicity of magnetic characteristics in rotor position, had motivated most researchers to use a truncated Fourier series based model. It was found that at least ten terms are required for good

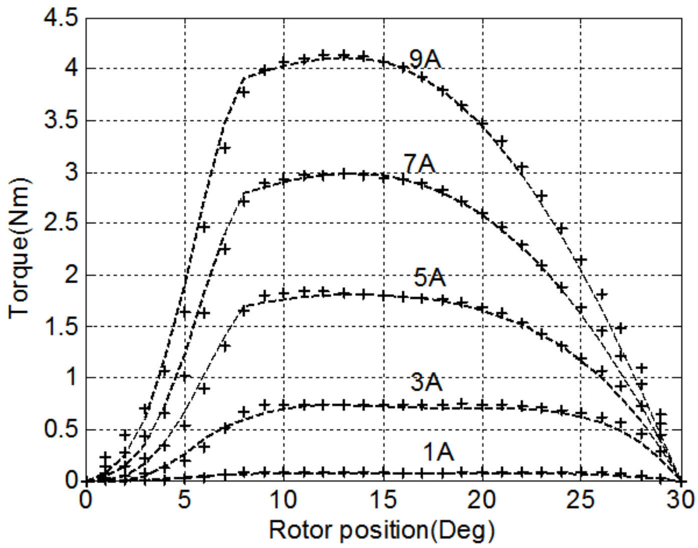

Figure 2.19: Matching of measured static torque data with the torque predicted by the toque model derived from the polynomial flux-linkage model.

approximation, which is computationally intensive. A novel fifth order polynomial modelling technique is introduced in this chapter. The effect of flux-fringing is dominant towards unaligned region, and effect of saturation is dominant near aligned region and higher currents. Thus, the operating range was divided into four different regions. Each region was then fit by a fifth order polynomials, which results in a smooth as well as accurate fitting. The fifth-order polynomials require less computation as compared to exponential or trigonometric functions. More importantly, instantaneous torque, incremental inductance and back-emf constant etc. can be obtained accurately from the flux-linkage model, through differentiation. The polynomial based model for torque has been used for torque estimation in closed-loop torque control algorithms shown in following chapters. The incremental inductance and back-emf constants derived from the flux-linkage model can be used for implementation of model-based controllers for SRM.

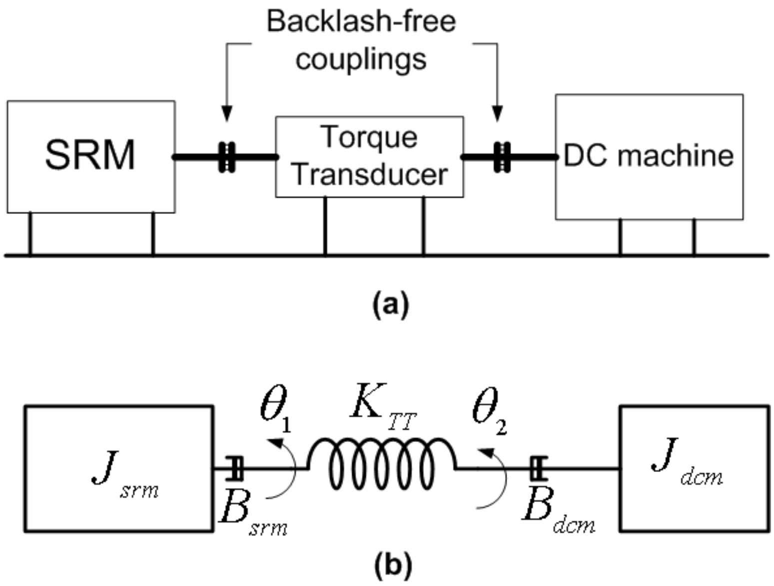

Figure 2.20: Schematic of the experimental system showing the SRM, torque transducer and DC machine

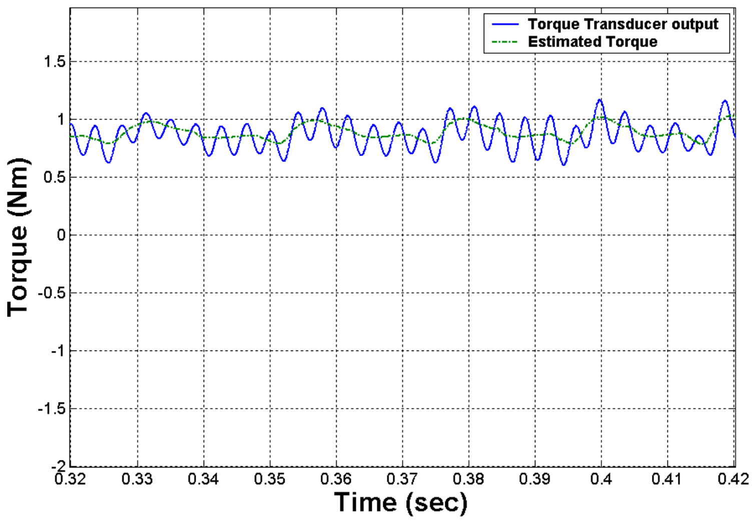

Figure 2.21: Simulation result: comparison of the output of the strain-gauge type torque transducer with torque estimator

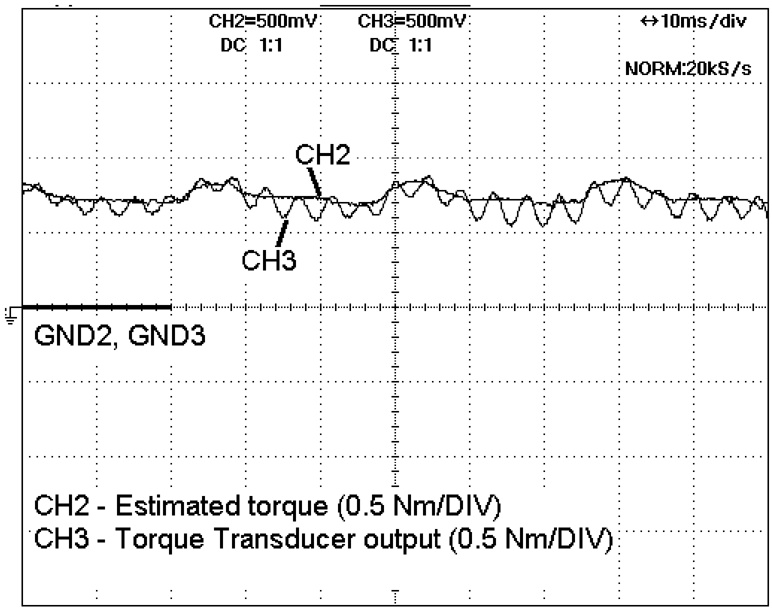

Figure 2.22: Experimental result: matching of torque transducer output and model estimated torque under motor running condition. Torque reference=0.8 N.m

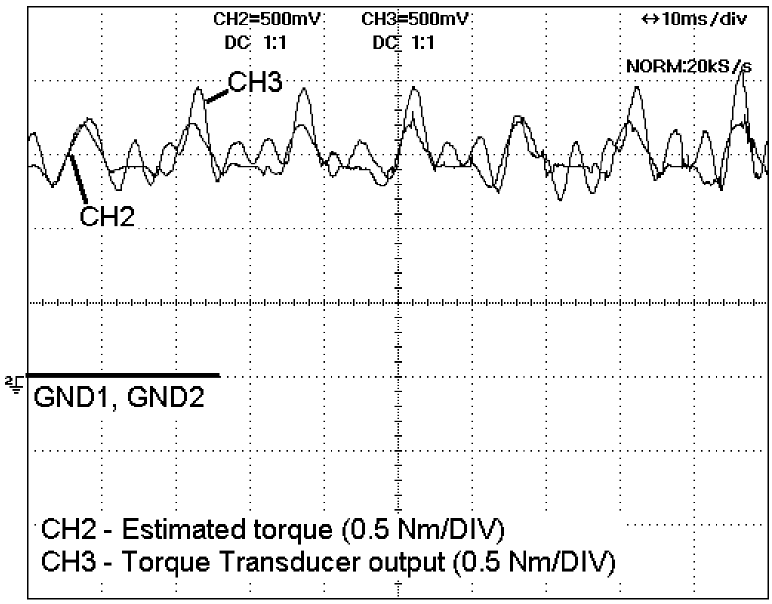

Figure 2.23: Experimental result: matching of torque transducer output and model estimated torque under motor running condition. Torque reference=1.5 N.m

Chapter 3

Torque Sharing Function

Conventionally, SRM was operated with one phase winding excited at a time. As instantaneous transfer of phase torque is not possible, this mode of operation leads to large variation of torque during phase torque commutation. To overcome this problem, a suitable torque sharing function (TSF) needs to be designed which ensures that two or more phases share the total torque demand and each phase torque reference changes smoothly. This chapter elaborates the design method of such a TSF.

3.1 Introduction

Each stator phase winding in SRM produces a positive torque in the region of increasing inductance (when rotor pole moves from unaligned position to aligned position) and negative torque in the decreasing inductance region. Hence, depending on the sign of the demanded torque, the required phases are energized for half the period of inductance profile. This region of conduction is called the active re-

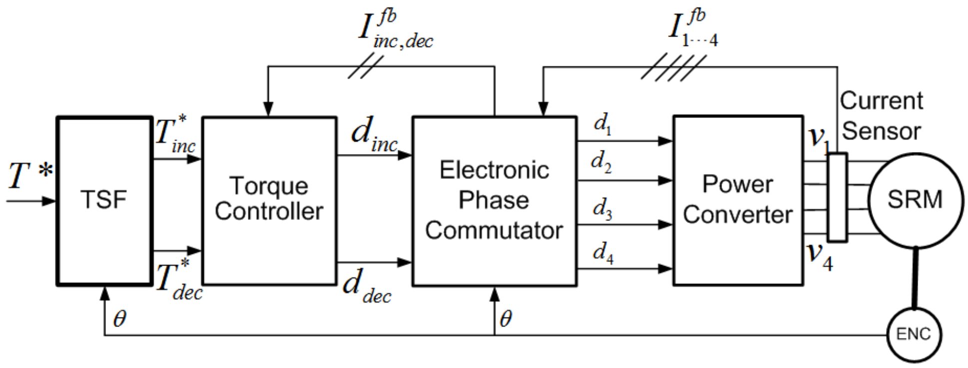

Figure 3.1: Torque Sharing Function block in the torque controller for the prototype SRM. T^* is demanded motor torque, T^*_{inc} and T^*_{dec} are increasing and decreasing phase torque shares, I^{fb}_{inc} and I^{fb}_{dec} are increasing and decreasing phase current feedback, d_{inc} and d_{dec} are duty-cycles for the increasing and decreasing phases, $I^{fb}_{1...4}$ are the four phase current feedback, d_1 to d_4 are duty-cycles for the four phases, v_1 to v_4 are four phase voltages, θ is rotor position feedback

gion. Ideally, as soon as the phase enters the active region, the phase current should be increased to a level so that it produces the total demanded torque. Similarly, the phase current should be removed as soon as it comes out of the active region. Due to non-zero phase inductance and finite DC-link voltage available, rise or fall of stator phase currents is possible only at a finite rate. Fortunately, there is an area of overlap between the active region of two neighboring phases of SRM when both can produce torque in the same direction. By exploiting this fact, the torque demand can be divided between the neighboring phases. However, the division can not be arbitrary but has to satisfy certain constraints.

3.1.1 Literature Survey for Commutation Methods

In [13], the outgoing phase is forced to be switched off quickly by applying the full negative voltage at ‘critical rotor position’ (θ_c). Rotor position where the torque productivity of the two neighboring phases is identical, with each phase carrying half the demanded motor torque, is known as critical rotor position. The torque produced by the outgoing phase is estimated and subtracted from the demanded torque. The balance torque becomes the reference for the the incoming or stronger phase. This approach of switching the outgoing phase too fast may lead to a situation when the incoming phase is not able to produce the balance torque. Also in a discrete-time implementation, using feedback alone to determine the torque reference for the incoming phase may lead to large torque tracking error.

In [39], the incoming phase current reference starts to rise while the outgoing phase current reference starts to fall so that, at the critical position, both the phases share the demanded torque equally. The main motivation behind this approach is to minimize the peak current reference for each phase. However, this method leads to large torque ripples, as it does not ensure that total torque produced matches the demanded torque.

In [40], Russa *et al.* define the on-angle (θ_{on}) at which the incoming phase is switched on and off-angle (θ_{off}) when the same phase looses active current control and goes into voltage control. Only in-coming phase has active current control where as the out-going phase is applied 0 voltage for sometime and then full negative dc-link voltage. The choice of θ_{on} and θ_{off} play an important role in the success of this scheme.

In [41], Tseng *et al.* do a good review of earlier works on commutation methods. They have suggested improvement on [40], to make it work over a large speed range by making it adaptive to speed. The on-angle (θ_{on}) and off-angle (θ_{off}) are advanced with increase in speed. Both the decreasing and increasing phase torque references are varied linearly. Both the phase currents are controlled actively, to avoid the case where the torque demand in the in-coming phase is not achievable. A torque limit for each phase at each rotor position is stored which ensures that the torque reference found by the linearly varying TSF is achievable.

Husain [8] has done an extensive survey on various torque ripple minimization techniques proposed in the last decade. Husain has divided the conduction period for each SRM phase into (1) period of magnetization when full voltage V_{dc} is applied up to the critical angle so that the incoming phase current quickly grows to a substantial value, (2) period of active current control, where the phase is supposed to be the strongest and has the responsibility of producing the difference between the total torque demand and torque produced by all the other phases, 3) period of demagnetization when $-V_{dc}$ is applied to the outgoing phase so that it demagnetizes the phase winding as quickly as possible. At any time, only one phase is in active current control while the other phases go into voltage control mode. There is a possibility of the outgoing phase current reducing too fast so as the cause the incoming phase current to be very high.

In [42], Baoming *et al.* have followed a similar approach as Husain in [8], but proposed to avoid the computational complexity of adapting the critical angle and instead fix it at the point when the phase inductance starts to increase sharply with rotor position. This happens to be the point of highest torque productivity. Full positive dc-link voltage is applied at an angle θ_{on}, ahead of the critical angle so that the current is increased quickly up to the critical angle after which this phase takes over as the strongest phase and goes into active current control mode. The previously active phase current is slowly reduced in a controlled manner ensuring it is switched off before the rotor poles are fully aligned. The on-angle, θ_{on} is calculated based on speed and the required torque level. The torque produced by the phases other than the active phase are estimated using a look-up table and subtracted from the demanded torque to give the torque reference for the active phase. Another look-up table is used to convert the toque reference to current reference and an inner current controller based on nonlinear internal model based controller is used.

For accurate tracking of the time-varying phase torque references, feed-forward control algorithm is necessary. As feed-forward controller requires derivative of the references, each phase torque should be known in advance and also should be differentiable. Hence, the method where one phase torque reference is obtained by subtracting the estimated torque for the other phase from the total demanded torque, is not appropriate for feed-forward control.

3.2 Optimal TSF

The primary constraint on choice of TSF is:

$$T_d = T_{inc} + T_{dec} \tag{3.1}$$

where,

$$\begin{aligned} T_{inc} &= T_d\, f(\theta) \\ T_{dec} &= T_d\, (1 - f(\theta)) \end{aligned} \tag{3.2}$$

where T_d is the motor torque demand, T_{inc} and T_{dec} are torque references for the increasing (incoming) and decreasing (outgoing) phases respectively, and $f(\theta)$ is the position dependent torque sharing function (TSF). The motor torque demand can be distributed among the phases in infinite number of different ways to satisfy the constraint in (3.1). However, while deciding the torque sharing function, a few additional points need to be considered, such as:

- the resultant phase torque references can be tracked for a wide speed range with the available DC-link voltage; and
- the motor torque is produced with least copper loss.

It will be shown in following subsections that these conditions are in conflict requiring a need for optimization.

3.2.1 Maximizing Speed Range

The torque sharing function has to be chosen so that each phase torque reference is trackable for a large speed range. Unidirectional torque can be produced only in one half of the phase inductance period. Hence, phase current has to grow and fall during a finite range of rotor position. As the motor speed increases, the required time rate of change of current reference increases. The time rate of rise of current is dependent on the phase inductance and available DC-link voltage as given in in Chapter 2 (2.7). The voltage drop due to the phase winding resistance can be ignored at high speeds as back-emf becomes large. Then,

$$\begin{aligned} \frac{di}{dt} &= \left(\frac{\partial\psi}{\partial i}\right)^{-1}\left(v - \frac{\partial\psi}{\partial\theta}\frac{d\theta}{dt}\right) \\ \frac{di}{dt} &= \frac{di}{d\theta}\frac{d\theta}{dt} \\ \frac{di}{d\theta} &= \left(\frac{\partial\psi}{\partial i}\right)^{-1}\left(\frac{v}{\omega} - \frac{\partial\psi}{\partial\theta}\right) \end{aligned} \tag{3.3}$$

where,

- $\frac{di}{d\theta}$ is position rate of change of phase current
- $\omega = \frac{d\theta}{dt}$ is the motor speed
- $\frac{\partial\psi}{\partial i}$ is the incremental phase inductance
- $\frac{\partial\psi}{\partial\theta}$ is the back-emf constant
- v is the voltage across the stator winding
- i is phase current
- ψ is the flux-linkage for the phase winding

For SRM, phase inductance and torque are nonlinear functions of phase current and rotor position. For ease of understanding, the analysis of maximum allowed rate of change of phase torque reference is shown for the idealized trapezoidal phase inductance profile given in (1.8). For this case, incremental inductance and back-emf constant can be obtained as:

$$\begin{aligned} \psi &= L(\theta)i \\ \frac{\partial\psi}{\partial i} &= L(\theta) \\ \frac{\partial\psi}{\partial\theta} &= \frac{dL(\theta)}{d\theta}i = K\,i \end{aligned} \tag{3.4}$$

From (3.3), for a given DC-link voltage and rotor speed, the allowed rate of change of current reference with rotor position will be the minimum near the aligned rotor position, where phase inductance is maximum (L_a). This being the worst case, the TSF should be tested at the aligned rotor position. Using (3.3) we get this as:

$$\left|\frac{di}{d\theta}\right|_{\theta_a} = \frac{1}{L_a}\left(\frac{V_{dc}}{\omega} - iK\right) \tag{3.5}$$

The TSF should be so designed that the $\frac{di}{d\theta}$ is less than the value obtained from

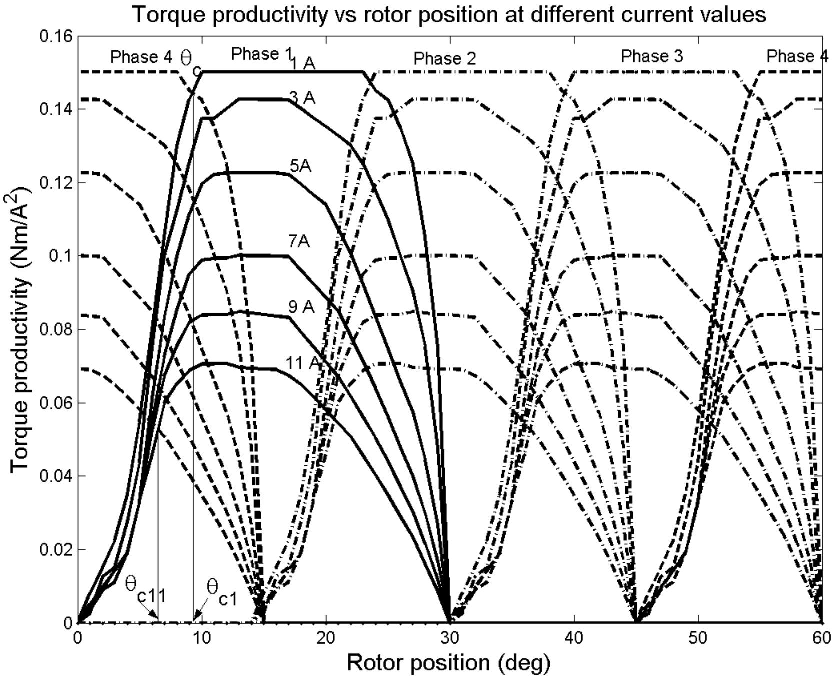

Figure 3.2: Torque productivity distribution for the prototype SRM at different current levels and rotor positions; θ_{c1} and θ_{c11} are the critical angles at 1 A and 11 A current, respectively

(3.5), for the desired speed range. When motor operates in magnetic saturation, actual incremental inductance and back-emf constants will be less than the idealized values. Thus, the approximation leads to a conservative estimation of the allowable motor speed range.

3.2.2 Minimizing Copper-loss

Torque production in SRM with an idealized inductance profile was given in Chapter 1, which is equivalent to a DC series motor. However, for the real SRM, the torque productivity is a function of both rotor position and phase current, as given by following equation,

$$T_j(i_j, \theta) = \frac{1}{2} C_T(i_j, \theta) i_j^2 \tag{3.6}$$

where $C_T(i_j, \theta)$ can be called as the *effective torque constant*, indicating the torque productivity ($N.m/A^2$). When the demanded torque is shared by more than one phase, the total copper loss is $\sum_{j=1}^{4} {i_j}^2 R_j$, which can be rewritten as $\sum_{j=1}^{4} 2\, \frac{T_j(i_j,\theta)}{C_T(i_j,\theta)} R_j$. Hence, copper loss will be minimum when total toque is developed by the phase having highest value for the effective torque productivity $C_T(i_j, \theta)$. However, instantaneous transfer of torque production responsibility from one phase to another phase is not possible. Hence, for less copper loss, phase having the higher torque productivity should share as much of the total torque demand as possible. This in turn depends on the limited DC-link voltage available.

The torque productivity for the SRM can be obtained from the static torque measurements for one phase. For other phases, the torque productivity can be obtained by shifting the productivity curves along the rotor position axis. In Fig.3.2, each curve shows the torque productivity for a phase, at constant current and for different rotor positions between unaligned and aligned positions. Following observations can be made about the torque productivity for the phases.

- Torque productivity is zero at both the fully unaligned and fully aligned positions.
- Starting from zero at the unaligned position, it increases rapidly after certain amount of overlapping between rotor and stator poles.
- As the stator and rotor pole overlap increases, the torque productivity slowly drops due to saturation of the magnetic circuit.

For two consecutive phases, there is a rotor position at which the torque productivity is same for both the neighboring phases. This rotor position is called critical rotor position (θ_c), where both the phases should share the demanded torque equally. It can be seen that (θ_c) varies with current level. For prototype SRM, the *critical rotor position* for phase current value of 1 A and 11 A are shown in Fig.3.2. Assuming that all the phase windings have identical torque characteristics, the productivity curves for only only phase are estimated from measured static torque. For the remaining phases, the productivity curves are obtained by shifting the curve for the previous phase by 15^0.

The incoming phase should be switched on just before θ_c and the incoming phase current should start to build. To keep the total torque production constant, the outgoing phase current should keep falling after the incoming phase is switched on. After θ_c, the outgoing phase would be less productive than the incoming phase. Hence, the outgoing phase current should be removed as soon as possible, after which the incoming phase should produce the total demanded torque. Thus, choosing a TSF involves a trade-off between minimizing the copper-loss and maximizing the speed range. Finally, the TSF should be computationally simple for real-time implementation. Keeping this in mind, a cubic TSF is further investigated.

3.3 TSF with Cubic Component

For minimizing copper loss, the phase current should be commutated at the critical angle (θ_c) i.e. rotor position where two neighboring phases have the same torque productivity $C_T(i, \theta)$. It is shown in Fig.3.2 that θ_c changes with phase current. However, the variation in θ_c is limited to a small range. Hence, in this work, the commutation angle is fixed at the middle of this range. This leads to ease of implementation.

Recalling (3.6), $T_j(i_j, \theta) = \frac{1}{2}\, C_T(i_j, \theta)\, i_j^2$ and

$$\begin{aligned} \frac{dT_j}{d\theta} &= C_T(i_j, \theta)\, i_j\, \frac{di_j}{d\theta} \\ &= \sqrt{\frac{2\, T(i_j, \theta)}{C_T(i_j, \theta)}}\, C_T(i_j, \theta)\, \frac{di_j}{d\theta} \\ &= \sqrt{2\, T(i_j, \theta)\, C_T(i_j, \theta)}\, \frac{di_j}{d\theta} \end{aligned} \tag{3.7}$$

For the incoming phase $T_{inc} = T_d f(\theta)$ where T_d is the motor torque demand and $f(\theta)$ is the torque sharing function. Then,

$$\frac{di_{inc}}{d\theta} = \frac{\frac{dT_{inc}}{d\theta}}{\sqrt{2\, T_{inc}(\theta)\, C_T(i_{inc}, \theta)}} = \frac{T_d\, \frac{df}{d\theta}}{\sqrt{2\, T_d\, f(\theta)\, C_T(i, \theta)}} \tag{3.8}$$

As $f(\theta)$ is in the denominator, (3.8) implies that $\frac{df}{d\theta}$ has to be zero when $f(\theta) = 0$, to have a finite $\frac{di_{inc}}{d\theta}$:

$$\frac{df}{d\theta} = 0, \ \text{ when } f(\theta) = 0 \tag{3.9}$$

This constraint can be satisfied in the simplest way by a cubic polynomial, as shown in the following section. For 8/6 pole SRM, there is an overlap period of 15^0 (mechanical) when two phases can produce torque in the same direction. Hence, the commutation process is repeated every 15^0, with all the phases taking an increasing and decreasing torque share, sequentially.

3.3.1 Designing the Cubic TSF

The TSF defined over this 15^0 will divide the torque reference to T_{inc} and T_{dec} with each having one zero, rising, and full torque segments. In the interval defined by rising and falling segments, called as 'overlap period', two adjacent phases conduct. The rising and falling segments are both cubic polynomials $T_d\, f(\theta)$ and $T_d(1-f(\theta))$ characterized by four arbitrary parameters.

$$f(\theta) = A + B(\theta - \theta_{on}) + C(\theta - \theta_{on})^2 + D(\theta - \theta_{on})^3 \tag{3.10}$$

where the A, B, C, D are constants, chosen so as to satisfy the two constraints 3.1 and 3.9; θ is the rotor position, θ_{on} is the on-angle and θ_v is the overlap-angle. The T_{inc} and T_{dec} are defined as,

$$T_{inc} = \left\{ \begin{array}{cl} 0 & \text{for } 0 \leq \theta \leq \theta_{on} \\ T_d\, f(\theta) & \text{for } \theta_{on} \leq \theta \leq \theta_{on} + \theta_v \\ T_d & \text{for } \theta_{on} + \theta_v \leq \theta \leq 15^0 \end{array} \right. \tag{3.11}$$

$$T_{dec} = T_d - T_{inc} \tag{3.12}$$

The constraints for the rising segment are defined by

$$f(\theta) = \left\{ \begin{array}{cl} 0 & \text{at } \theta = \theta_{on} \\ T_d & \text{at } \theta = \theta_{on} + \theta_v \end{array} \right. \tag{3.13}$$

$$\frac{df(\theta)}{d\theta} = \left\{ \begin{array}{cl} 0 & \text{at } \theta = \theta_{on} \\ 0 & \text{at } \theta = \theta_{on} + \theta_v \end{array} \right. \tag{3.14}$$

With these constraints (3.13) and (3.14), the various constants of (3.10) can be derived as,

$$A = 0\,;\; B = 0\,;\; C = \frac{3}{\theta_v^2}\,;\; D = -\frac{2}{\theta_v^3}\,. \tag{3.15}$$

The final form for the cubic function can be put as:

$$f(\theta) = (3\,\theta'^2 - 2\,\theta'^3) \tag{3.16}$$

where $\theta' = \frac{\theta - \theta_{on}}{\theta_v}$.

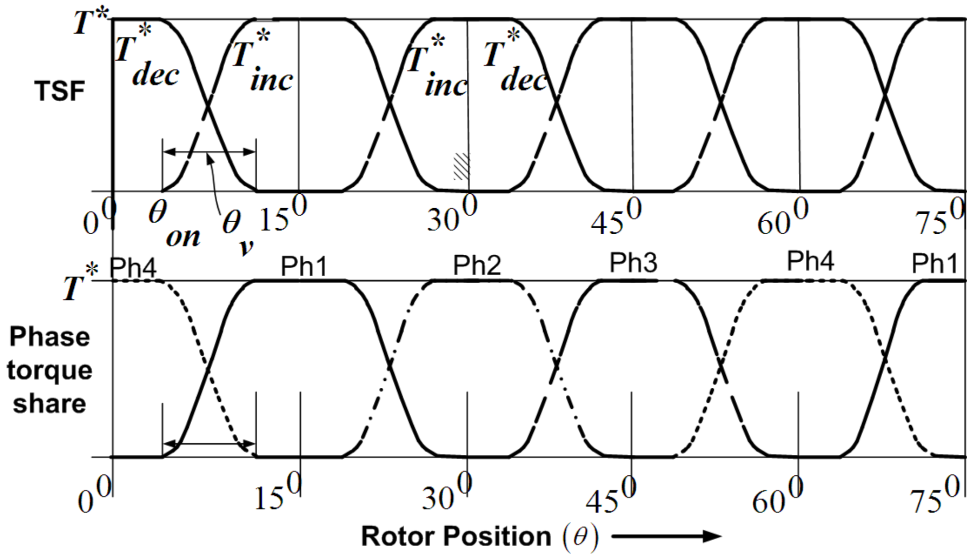

Figure 3.3: Torque sharing function with cubic segments

The overlap period θ_v should be small to ensure that the torque producing responsibility is transferred as fast as possible leading to better energy efficiency. However, a small θ_v would mean a large time rate of change of phase torque/current reference for a given speed. Following is an analytical expression for the minimum value of θ_v possible for a given operating speed.

$$\frac{dT_{inc}}{d\theta} = T_d \frac{df}{d\theta} = \frac{T_d * 6}{\theta_v} * (\theta' - \theta'^2) \tag{3.17}$$

Then

$$\begin{aligned} \frac{di}{d\theta} &= \frac{\frac{dT_{inc}}{d\theta}}{\sqrt{2T_{inc}(\theta) C_T(i,\theta)}} \\ &= \frac{\frac{6T_d}{\theta_v}\left(\theta' - \theta'^2\right)}{\sqrt{2T_d(3\theta'^2 - 2\theta'^3) C_T(i,\theta)}} \\ &= \frac{6T_d}{\theta_v \sqrt{2T_d C_T(i,\theta)}} \frac{1-\theta'}{\sqrt{3-2\theta'}} \end{aligned} \tag{3.18}$$

for $\theta' \neq 0$.

So:

$$\left(\frac{di}{d\theta}\right)_{\theta'=1} = 0 \tag{3.19}$$

The rate of change of required phase current is maximum for $\theta' = 0$ for the operating range and keeps falling until it becomes zero at $\theta' = 1$.

$$\theta_{v_{min}} = \sqrt{\frac{6T_d}{C_T(i,\theta)} \frac{1}{\left(\frac{di}{d\theta}\right)_{max}}} \tag{3.20}$$

The maximum possible value for $\frac{di}{d\theta}$ is dependent on the available DC-link voltage, motor speed and phase inductance, as given in (3.5). As seen in (3.3), $\frac{di}{d\theta}$ decreases with increasing phase inductance. Hence, we should use the maximum phase inductance at aligned position for obtaining $\left(\frac{di}{d\theta}\right)_{max}$ allowed for the DC-link voltage and desired upper limit for motor speed for instantaneous torque control. This is then used to obtain $\theta_{v_{min}}$ for the system. Then the minimum value for θ_v can be obtained from (3.20).

For the prototype SRM used in this work, with $C_T(i_j, \theta) = K = 0.14$, $L_a = 0.1H$, and for DC-link voltage of $100\,V$, $\omega = 200\,rpm$, we get $\theta_{v_{min}} = 5^0$. To have active instantaneous torque control at higher speeds, θ_v has to be increased. This means advancing the starting position for the phase current commutation. However, as $C_T(i,\theta)$ also falls drastically towards the unaligned region, the motor will loose active phase torque control and has to be operated in on-off mode.

Once the θ_v is designed for the required operation, the on-angle can be obtained using $\theta_{on} = \theta_c - \frac{\theta_v}{2}$. This completes the design of the cubic-segment TSF used in the thesis work.

3.4 Summary

In this chapter, a cubic TSF has been designed for SRM, which provides trackable references for two near-by phases. It is also important to ensure that total torque is produced while minimizing copper loss and maximizing operating speed range. Mathematical analysis has been given for obtaining the overlap-angle θ_v and on-angle θ_{on}. The following chapters discuss phase torque tracking controllers for realizing the phase torque references accurately.

Chapter 4

Indirect Torque Controller for SRM - ILC Based Torque-to-current Conversion

In electromagnetic motors, torque is produced due to current in the phase windings. In a separately excited DC motor, when field current is held constant, motor torque is proportional to the armature current. In field-oriented control (FOC) of induction motor drive, the motor torque is proportional to the quadrature component of the stator current, when the equivalent field current component in the d-axis is maintained constant. Thus, torque can be controlled indirectly by controlling the motor current. These schemes can be called as *indirect torque control* (IDTC). These schemes need to convert the motor torque reference to equivalent current reference. SRM torque can be controlled indirectly like other electric motors as shown in Fig.4.1. However, due to the highly-nonlinear and coupled relationship SRM torque has with phase current and rotor position; torque reference can not be easily converted into current reference. Researchers have proposed various methods for solving this problem, which are discussed in the following section. In this chapter, *iterative learning control* (ILC) is used for torque-to-current conversion in IDTC of SRM. The phase torque references and the equivalent current references are periodic in rotor position. As rotor rotates at constant speed, both phase torque and current references become repetitive in time. Hence, iterative learning method can be used for updating the phase current references from cycle to cycle. Detailed analysis and experimental verifications of the proposed scheme are provided in this chapter.

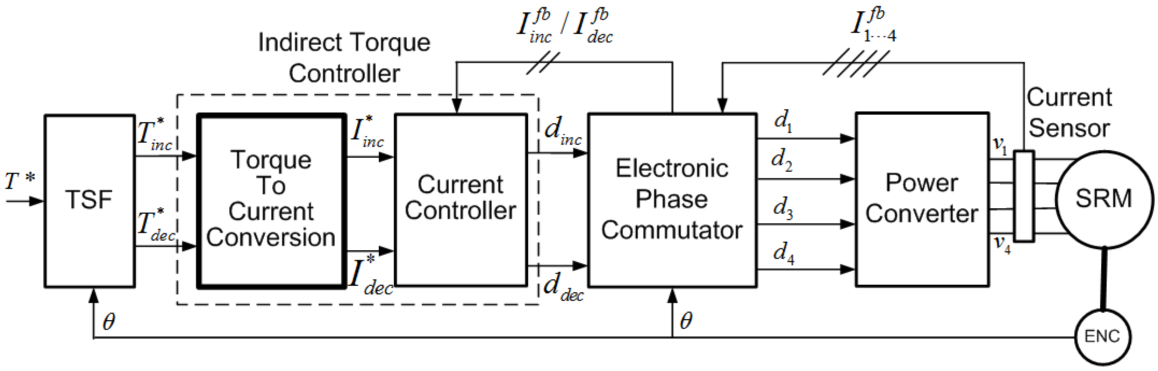

Figure 4.1: Torque-to-current conversion in IDTC scheme for SRM. I^*_{inc} and I^*_{dec} are increasing and decreasing phase current references

4.1 Past Work on Torque-to-current Conversion for SRM drive

In [36], Husain *et al.* have used the torque expression for an SRM having ideal phase inductance profile, where the inductance increases or decreases proportionately with the angle of overlap. Thus ($\frac{dL}{d\theta}$) will be constant throughout the conduction interval for all the current levels. This is re-written below,

$$T = \frac{1}{2}\frac{dL}{d\theta}i^2 \Rightarrow i = \sqrt{\frac{2T}{\frac{dL}{d\theta}}} \tag{4.1}$$

However, this assumption leads to a large error both in instantaneous as well as average torque, as magnetic saturation causes the phase inductance to vary with phase current as well. The amount of error would depend on the motor torque level, as larger torque levels would cause more saturation and hence more deviation from the idealized phase inductance profile.

In [52], Nirod has suggested using an empirical multiplying factor $F \geq 1$ to compensate for the loss in average torque when above mentioned method is used.

$$i = F\sqrt{\frac{2T}{\frac{dL}{d\theta}}} \tag{4.2}$$

However, a constant multiplying factor (F), chosen by trial and error may not be desirable for high performance torque control. Secondly, this method only improves the average torque production and not the instantaneous torque.

In [69], Taylor *et al.* have suggested approximating the torque as proportional to the square of stator current, where the multiplying factor is assumed to vary as a sinusoidal function of rotor position alone. This approximation leads to a decoupled and hence invertible expression for torque-current relationship as:

$$T(i_j, \theta) = F \sin(4\theta) {i_j}^2 \Rightarrow i_j = \sqrt{\frac{T}{F \sin(4\theta)}} \tag{4.3}$$

where F represents the torque-constant. This method captures variation of torque productivity well. However, the factor F should be a function of current level as well, since current level decides the level of magnetic saturation. Hence, such method is not accurate.

A two-dimensional look-up table [8], [41] which stores the equivalent current for various demanded torque and rotor positions, is often used for converting torque reference to current reference. This method requires very little computation. Due to the highly nonlinear nature of SRM, a finer resolution over the range of rotor position and operating torque level, is needed for good accuracy. This may be a constraint due to the limited availability of on-line memory.

Artificial neural networks (ANNs) are another type of tool used for nonlinear mapping with inherent learning capability. A multi-layer perceptron (MLP) type of ANN [21], with phase torque reference and rotor position as input, and phase current references as output, can be designed and trained off-line. As compared to a look-up table, ANNs require much less memory space. ANNs have the additional property of generalization, which can be used to filter any noise in the measurement data. However, unlike look-up table, ANNs may involve large amount of on-line computation. In [22], Reay *et al.* have used a cerebellar model articulation control (CMAC) network in place of MLP. CMAC network exhibits local globalization property and hence is most suitable for on-line learning. The network outputs are initialized with linear current profiles which make the motor run. The actual torque is measured from a torque transducer and compared to the demanded torque. The torque error is used to adjust the network outputs. On-line training takes care of the effects of any dynamics not captured through static measurements.

In [25], Henriques *et al.* use a Neuro-Fuzzy compensator that is trained off-line with the desired torque and rotor position as inputs and the current reference as the output. This method combines neural network's inherent capability of learning, with the suitability of Fuzzy systems for nonlinearities and model uncertainty in SRM. However, Fuzzy systems are not appropriate for high-performance due to the very reason of being dependent on linguistic rules.

It is being proposed to exploit the periodic nature of SRM excitation current profile for a given demanded torque, and use an 'iterative learning' based method for torque-to-current conversion. Though assuming an idealized phase inductance profile is not accurate, it can be used to provide a good initialization for our proposed torque-to-current conversion method. As the learning progresses, the system learns a position dependent compensation current to the initial current profile. The proposed method has been described in more details in the following section.

4.2 Proposed ILC Based Torque-to-current Conversion Scheme

Iterative learning is useful for solving trajectory control problems that are periodic in nature. This method is particularly useful for highly nonlinear systems like SRM. Starting with some initial values based on experience, the control input is updated from iteration to iteration, until the desired trajectory is tracked accurately.

The torque-to-current conversion problem can be formulated as follows. The phase torque reference is considered as the desired trajectory, and the phase current reference as the control input. Fig.4.2 shows the proposed scheme. The current reference will consist of two parts. Part-I (I^{nom}) is obtained from the torque reference by using the formula in (4.1). This part-I of the current reference provides good dynamic performance for the proposed scheme. Part-II is a rotor position dependent term (I^{ilc}) which is learned iteratively and compensates for the inaccuracies in part-I. The learning mechanism is driven by torque error (T^*_{err}) i.e. the difference between the desired torque and the torque estimated from the current reference. An analytical torque estimator based on (2.23) is used for computing the torque (T^*_{est}) from the current reference at each rotor position. The amount

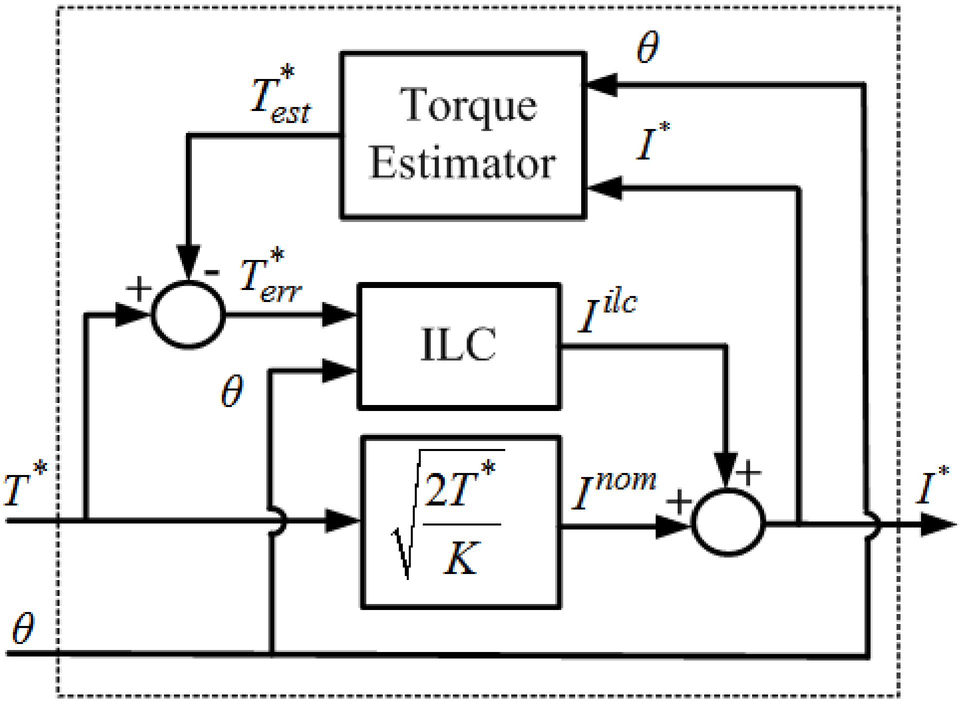

Figure 4.2: ILC based torque-to-current conversion scheme

of compensation would depend on the deviation of the actual inductance from the idealized inductance profile. For a given motor torque level, the required compensation is constant at each rotor position. The iterative learning scheme converges to this value.

The TSF block in Fig.4.1 divides the the motor torque reference T^* into T^*_{inc} and T^*_{dec}. The torque-to-current conversion block consists of two such blocks as shown in Fig.4.2, one each for the increasing phase and the decreasing phase. Both T^*_{inc} and T^*_{dec} have a period of 15^0. Hence, the ILC scheme has a period of 15^0, which constitutes one learning cycle. The task is to learn the compensation current at various rotor positions. First, one cycle of rotor position is divided into N_i position intervals. The integer N_i is chosen large enough so that, the compensation current can be considered to be constant over one interval, with tolerable error. This is required as the actual rotor position at the sampling instants will not be exact from iteration to iteration. Considering intervals of size 0.1^0, $N_i = 150$ for rotor position interval of 15^0.

The compensation current is updated according to the learning law given as:

$$I^{ilc}(m,n) = I^{ilc}(m-1,n) + G_2 \times T^*_{err}(m-1,n) \tag{4.4}$$

where $I^{ilc}(m,n)$ and $I^{ilc}(m-1,n)$ are the iteratively learned compensations for the current references at the n^{th} position interval for m^{th} and $(m-1)^{th}$ iterations respectively. The learning gain G_2 is designed to ensure convergence of the learning. $T^{err}(m-1,n) = T^*(n) - T^*_{est}(m-1,n)$ is the torque error for the n^{th} position interval, $T^*(n)$ is reference torque at the n^{th} position interval, $T^*_{est}(m-1,n)$ is estimated torque for the current reference at n^{th} position interval, for $(m-1)^{th}$ iteration.

The variation of phase torque with phase current can be approximated with Taylor's series, by ignoring the higher order terms as:

$$T(i,\theta) = T(i_0,\theta_0) + \left.\frac{\partial T}{\partial i}\right|_{i_0,\theta_0} \times (i - i_0) + \left.\frac{\partial T}{\partial \theta}\right|_{i_0,\theta_0} \times (\theta - \theta_0) \tag{4.5}$$

Assuming the learning occurs at identical rotor positions from iteration to iteration (i.e. $\theta = \theta_0$), the second term in (4.5) become zero. Hence, torque variation with current alone can be represented as:

$$T(i,\theta) = T(i_0,\theta_0) + \left.\frac{\partial T}{\partial i}\right|_{i_0,\theta_0} \times (i - i_0) \tag{4.6}$$

With torque as output, and phase current as input, the system gain is $\frac{\partial T}{\partial i}$. For learning in (4.4) to converge, the range of learning gain can be found in terms of the system gain [63]. Following inequality is solved to obtain this range:

$$\left|1 - G_2 \times \frac{\partial T}{\partial i}\right| < 1 \tag{4.7}$$

which leads to,

$$0 < G_2 < \frac{2}{\frac{\partial T}{\partial i}} \tag{4.8}$$

In actual implementation, it is advisable to start with a value for G_2 towards the lower end of this range and increase slowly until the system starts to be unstable.

4.3 Experimental Validation of the Proposed Torque-to-current Conversion Scheme

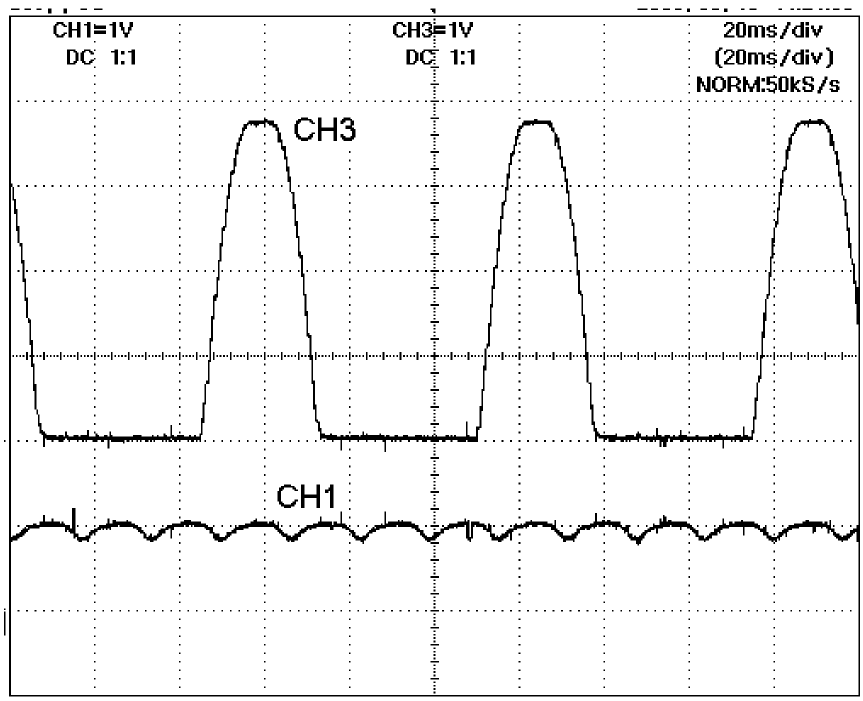

Figure 4.3: Torque-to-current conversion using the nominal model without the ILC compensation at 1 N.m, and 200 r/min, CH3(1 A/Div)-current reference without compensation, CH1(N.m/Div)-estimated total torque for the current reference

The proposed iterative learning based torque-to-current conversion scheme has been implemented in the experimental set-up. To verify the accuracy of this scheme, the current reference is converted back to torque, using the analytical torque estimator developed in Chapter-2. If torque-to-current conversion is accurate, then the estimated torque for the current reference shall match the demanded

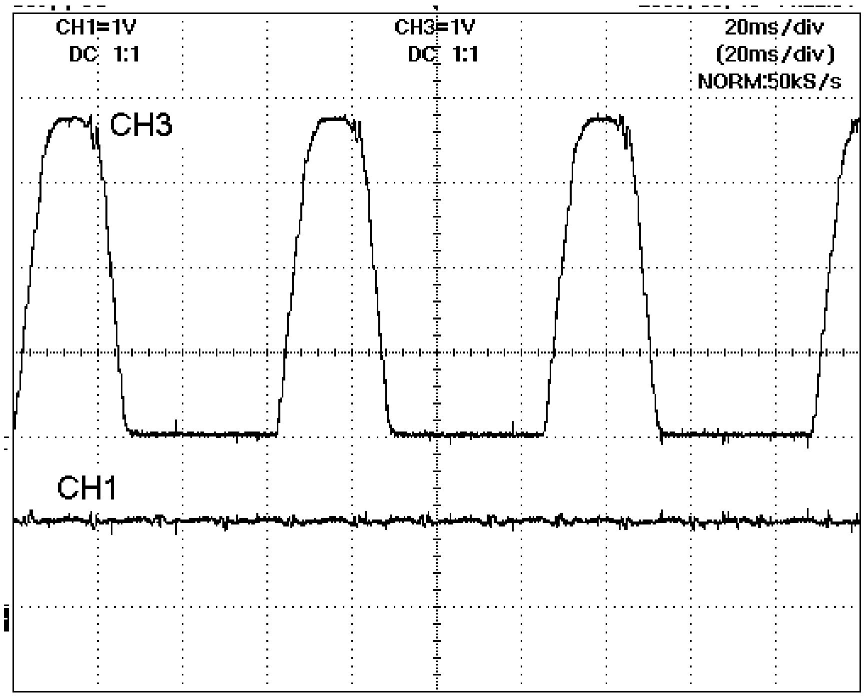

Figure 4.4: ILC based compensation for torque-to-current conversion at 1 N.m, motor speed = 150 r/min, CH3(1 A/Div)-current reference without compensation, CH1(1 N.m/Div)-estimated total torque for the current reference

torque. To show the contribution of the iteratively learned compensation part, at first only part-I(I^{nom}) of the torque-to-current conversion is enabled. In Fig.4.3, CH3 shows the current reference without any compensation, for a torque reference of 1 $N.m$. The torque-to-current conversion is not accurate as shown by the total torque estimated from this current reference in Fig.4.3,CH1. The average value of this estimated torque is about 0.9 $N.m$ with 25% ripple. This shows that using part-I alone of the torque-to-current conversion is not accurate.

When the part-II (I^{ilc}) of the torque-to-current conversion is activated, the compensation component gets added to the current reference of part-I (I^{nom}). The resultant current reference is converted back to torque through the torque estimator, for finding the T^*_{est}. As seen Fig.4.4, the estimated motor torque for the resultant current references, which is shown in CH1, matches the demanded motor torque reference of $1\,N.m$. The torque ripples have been reduced to almost zero. This confirms the effectiveness of the iterative learning based compensation scheme used for torque-to-current conversion.

4.4 Summary

The non-invertibility of SRM torque function poses a formidable challenge for the torque-to-current conversion in IDTC scheme. The past work on this issue has been discussed in this chapter. Iterative learning has been shown to be effective for converting the phase torque references to phase current references. Iterative learning is used due to the periodic nature of phase torque and current references. The equivalent current reference consists of two parts: a nominal current obtained from the linearized model of trapezoidal phase inductance profile, and a compensation current learned iteratively from the torque error corresponding to the current reference. The range of learning gain is derived which ensures learning convergence. This scheme does not involve any complex computation. Hence, it is suitable for real-time implementation of IDTC scheme for SRM.

Chapter 5

Indirect Torque Controller for SRM - Current Tracking Controller

The torque sharing function distributes the demanded motor torque among the active phases. Next, a suitable torque controller has to realize the phase torque references. In Chapter 2, it was shown that the phase toque is a function of phase current and rotor position. Thus, phase torque can be realized 'indirectly' by realizing a suitable phase current profile. In such indirect torque control scheme as shown in Fig.5.1, the phase torque references obtained from TSF are converted to equivalent phase current references such as I^*_{inc} and I^*_{dec}. The inner loop current controllers need to track the phase current references accurately. The highly nonlinear magnetic characteristics of SRM makes it difficult to obtain satisfactory tracking performance using conventional linear feedback controllers like PID. Hysteresis controller, when implemented on digital systems with finite bandwidth, results in large amount of current ripples. This is due to the unavoidable low-pass anti-aliasing filters in digital systems, which add phase lag in the feedback path.

Therefore, a suitable nonlinear controller has to be developed for accurate current tracking.

In the initial part of this chapter, various current controllers for SRM and other drives as reported in the literature, have been reviewed. Their performances have been tested by implementing on the prototype SRM. A current controller using ILC based compensation and P-type feedback controller is shown to achieve accurate current control. ILC is applicable when phase current references are periodic, as when motor torque demand is constant. Detailed analysis and results from experimental validation of the scheme have been provided in following sections.

A novel indirect torque controller (IDTC) for SRM is developed, by combining an ILC based torque-to-current conversion scheme discussed in Chapter 4, with the ILC-based current tracking controller. This ILC based IDTC scheme achieves low torque ripples for constant torque references when motor speed is constant.

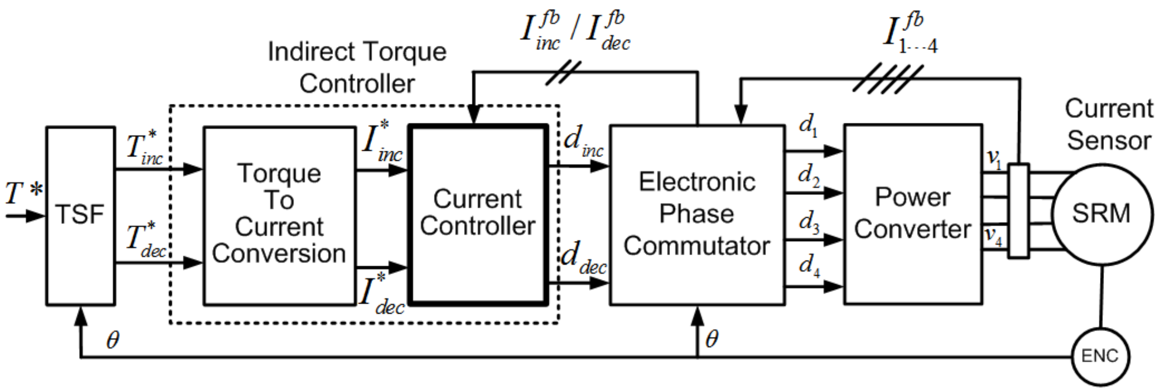

Figure 5.1: Current controller in IDTC scheme for SRM.

5.1 Nonlinear Current Dynamics

The voltage equation for any one phase winding of the SRM is given by:

$$\begin{aligned} v &= Ri + \frac{d\psi}{dt} \\ &= Ri + \frac{\partial\psi}{\partial i}\frac{di}{dt} + \frac{\partial\psi}{\partial\theta}\frac{d\theta}{dt} \end{aligned} \tag{5.1}$$

where v is the voltage across the stator phase winding, i is phase current, R is phase winding resistance, and ψ is the flux-linkage for the phase winding. Rewriting (5.1) in state-space form, we obtain the phase current dynamics as:

$$\frac{di}{dt} = \left(\frac{\partial\psi}{\partial i}\right)^{-1}\left(-Ri - \frac{\partial\psi}{\partial\theta}\frac{d\theta}{dt}\right) + \left(\frac{\partial\psi}{\partial i}\right)^{-1} v \tag{5.2}$$

The equation for a first order nonlinear dynamics can be written as:

$$\frac{dx}{dt} = f + bu, \tag{5.3}$$

where x is the system state, f captures the system nonlinearities, b is the plant gain and u is the control input. Considering current as the state variable *i.e.* $x = i$; current dynamics in (5.2) will be:

$$\begin{aligned} f &= \left(\frac{\partial\psi}{\partial i}\right)^{-1}\left(-Ri - \frac{\partial\psi}{\partial\theta}\frac{d\theta}{dt}\right) \\ b &= \left(\frac{\partial\psi}{\partial i}\right)^{-1} \end{aligned} \tag{5.4}$$

As SRM usually operates in deep magnetic saturation, its flux-linkage characteristics $\psi(i,\theta)$ is a highly nonlinear function of current and rotor position. The incremental inductance ($\frac{\partial\psi}{\partial i}$) and the back-emf constant ($\frac{\partial\psi}{\partial\theta}$) are functions of both current and rotor position. As rotor rotates, the incremental inductance and back-emf become time-varying. The current controller thus sees a nonlinear and time-varying plant. Additionally, the current reference is not constant but varies with rotor position. Current control problem becomes a nonlinear reference tracking control problem. Therefore, a linear feedback current controller can not achieve accurate current control for SRM and a suitable nonlinear tracking controller is needed. The following section does a review of past works done on current control of SRM.

5.2 Past Works on SRM Current Controllers

5.2.1 PI Controller

Linear feedback control theory is well developed and control schemes like PI are very popular in electric drives. Often, nonlinear system can be approximated to a linear system near a given operating point. Then the linearized plant can be used for linear control design. In [36], Husain *et al.* have proposed a PI current controller for SRM, as shown in Fig.5.2 and given by the following equation:

$$\begin{aligned} V &= K_p \times I^{err} + K_i \times \int I^{err}\, dt \\ d &= \frac{V}{V_{dc}} \end{aligned} \tag{5.5}$$

where V is the control voltage, I^{err} is current error, K_p is the proportional gain, K_i is the integral gain, V_{dc} is the DC-link voltage, and d is PWM duty cycle for the pulse-width-modulated (PWM) converter.

The PI gains are decided according to the desired overshoot and rise time or settling time. At a given rotor position and current value, the stator phase winding self-inductance (L_s) will have a certain fixed value. The current dynamics will be

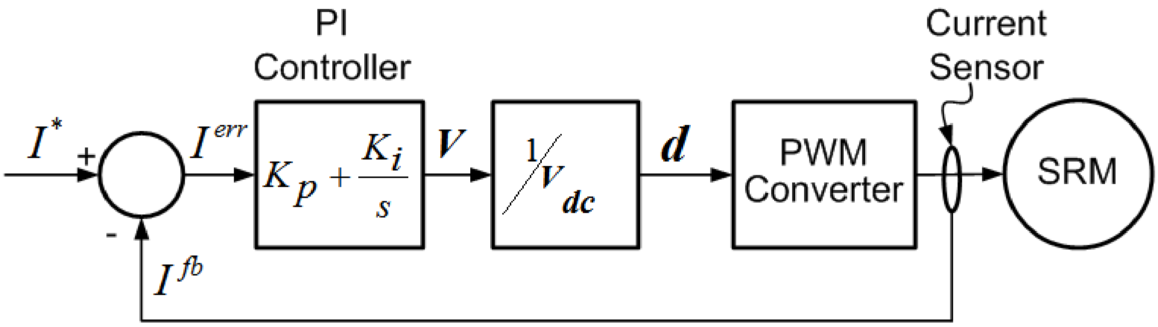

Figure 5.2: Block diagram for PI Current Controller; I^* current reference, I^{fb} - current feedback, I^{err} - current error, V - controller output, d - PWM duty cycle

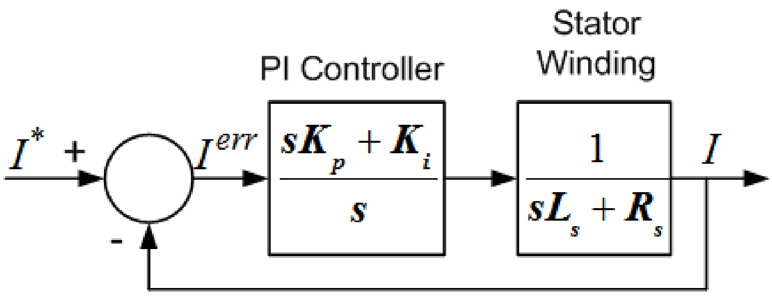

Figure 5.3: Block diagram showing the transfer function for PI Current Controller; I^* - current reference, I - current output, I^{err} - current error

linear time-invariant as:

$$\frac{dI}{dt} = -\frac{R_s}{L_s} I - \frac{e}{L_s} - \frac{V}{L_s} \tag{5.6}$$

where R_s and L_s are stator phase resistance and inductance respectively, e is the back-emf and can be treated as a disturbance term, V is the control voltage. The closed loop transfer function in Fig.5.3 will have a closed-loop transfer function as:

$$G_c = \frac{K_p\, s + K_i}{L_s\, s^2 + (R_s + K_p)\, s + K_i} \tag{5.7}$$

The PI gains can be chosen for the desired cutoff frequency $\simeq \omega_n$ and damping ratio ζ for the closed-loop system, which affect the rise-time, peak-overshoot and settling time in the step response.

$$\begin{aligned} K_i &= \omega_n^2\, L_s \\ K_p &= 2\,\zeta\,\omega_n \end{aligned} \tag{5.8}$$

The PWM frequency can be set higher than the audible frequency range to mitigate part of acoustic noise problem.

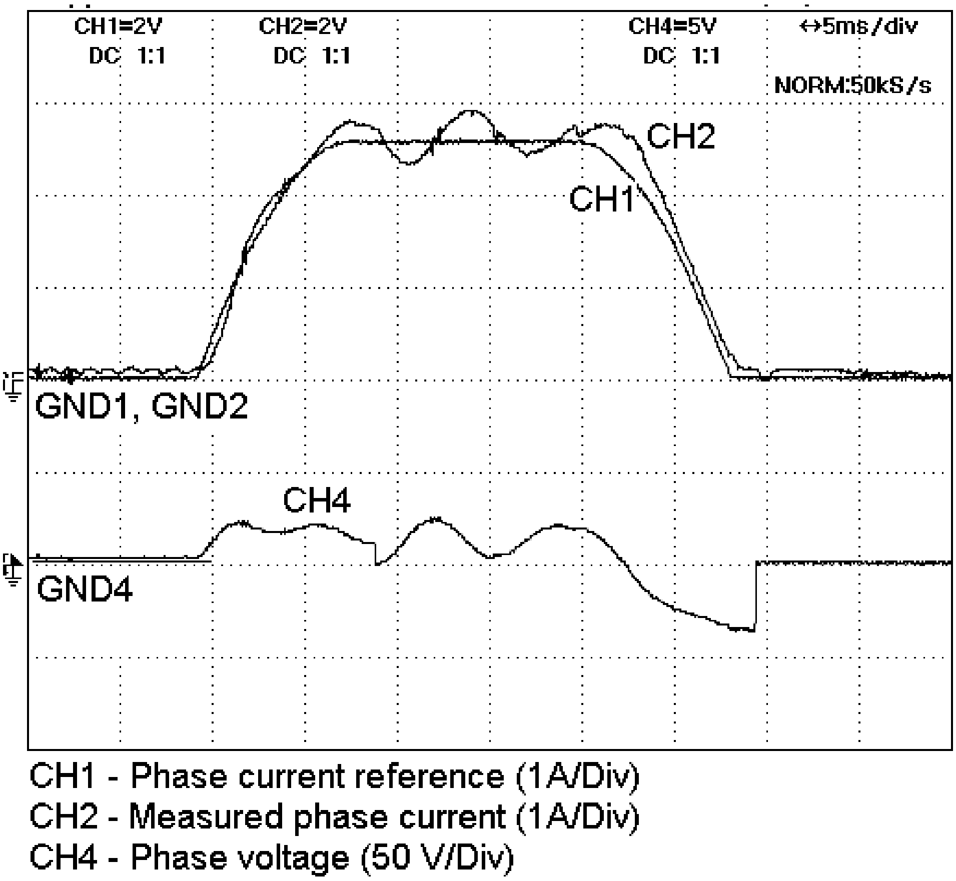

Figure 5.4: Current tracking performance of fixed-gain PI controller, CH1(1 A/Div)-phase1 current ref, CH2(1 A/Div)-phase1 measured current, CH4(1 A/Div)-phase1 current tracking error

For the experimental setup, program sampling frequency is $10\,kHz$. PI gains were set for $\omega_n = 200\,Hz$ and $\zeta = 0.75$ with $R_s = 2.0\,\Omega$ and $L_s = 0.05\,H$. The digital control law was:

$$V(k) = V(k-1) + 94.25\,e(k) - 86.35\,e(k-1) \tag{5.9}$$

Computer simulation of the PI current controller shows a rise time of about $500\,\mu s$ and peak-overshoot of $20\,\%$.

Fig.5.4 shows the experimental results for the PI current controller with motor running at $200\, r/min$ under a load torque of $1\, N.m$. PI controllers are suitable for regulation problems, where the reference is a constant or a step change. Integral controller can ensure $I^{err} \rightarrow 0$ as $t \rightarrow \infty$, only when the reference is constant. As shown in (5.2), SRM current controller sees a nonlinear plant with varying plant gain even within normal operating condition. Additionally, the current reference is time-varying. As expected and verified experimentally, integral(I) control is not effective in case of a finite-time tracking problem. The controller gains had been increased to reduce the tracking error in the rising and falling portions of the current reference. This had resulted in oscillations in current for constat part of current reference. A low-pass anti-aliasing filter with cut-off frequency of $1\, kHz$ is used on the measured current before using it as current feedback to the controller. Due to the additional phase lag introduced by this filter, phase margin is reduced. Hence, a large feedback gain can not be used to improve the tracking performance. This establishes that constant gain PI current controller is not suitable for high performance current controller in SRM.

An alternate method of using PI controller effectively for accurate current tracking in SRM had been proposed by Chapman *et al.* in [59]. In this paper, the authors have proposed to represent the pre-optimized current references as a series of harmonic components. A multi reference frame estimator/regulator concept is used, where a PI regulator is used for each harmonic component. Even though the current reference is time-varying, the harmonic coefficients are constants. Hence, the PI regulators see constant references. However, such scheme needs excessive off-line and as well as on-line computation and storage requirements.

5.2.2 PI Controller with Decoupling and Gain-scheduling

One approach of dealing with nonlinear systems is to linearize the system by state transformation, where a clever choice of new states and inputs are used to cancel out the nonlinearities of the system. This method is known as feedback-linearization. However, successful implementation of feedback-linearization scheme requires accurate and detailed knowledge of the nonlinearities in the plant. Without an accurate model, there may be substantial performance degradation due to improper cancellation of the nonlinearities. For SRM, the magnetization characteristics is modelled by using a nonlinear model from data obtained from rigorous measurements, or finite-element analysis. This process is time consuming and is prone to error. Hence, using such a model for feedback linearizing scheme, does not guarantee high performance.

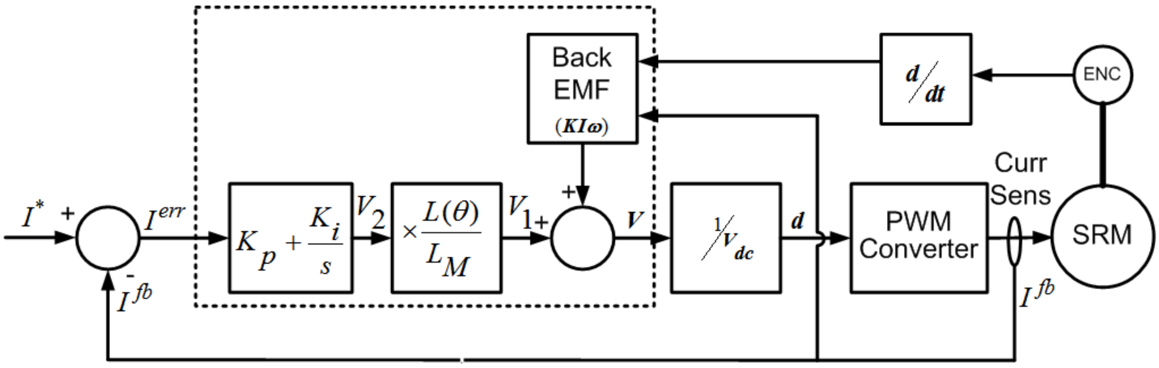

Figure 5.5: Block diagram of decoupled gain-scheduled PI current controller. I^* - current reference, I^{fb} - current feedback, V_2 - output of the PI controller, V-desired phase voltage, d - PWM duty cycle

As can be seen in (5.2), the back-emf ($\frac{\partial\psi}{\partial\theta}\frac{d\theta}{dt}$) acts as a disturbance. Hence, performance of the controller can be improved by cancelling the effect of back-emf by online estimation. In [60], the authors have used a linearized stator phase inductance profile to model the SRM as given in following equation:

$$\begin{aligned}\psi(i,\theta) &= L(\theta)\, i \\ \frac{\partial \psi}{\partial \theta} &= \frac{dL}{d\theta}\, i \\ \frac{\partial \psi}{\partial i} &= L(\theta)\end{aligned} \tag{5.10}$$

Introducing a new control input $V_1 = V + \frac{dL}{d\theta}\, i\, \omega$, and ignoring the effect of resistive drop, the resulting current dynamics becomes:

$$\frac{di}{dt} = \frac{1}{L(\theta)}\, V_1 \tag{5.11}$$

The plant gain is still variable in (5.11). If a new control variable is chosen as $V_2 = \frac{1}{L(\theta)}\, V_1$, then the transformed system will be an linear time-invariant (LTI), and PI controller should work better. The actual control input is:

$$V = (K_p\, I^{err} + K_i \int I^{err}) * \frac{L(\theta)}{L_M} - \frac{dL}{d\theta}\, \omega\, i \tag{5.12}$$

where L_M is the mid-value of stator phase inductance used for PI control design. Fig.5.5 shows the block diagram for the controller. It was found that decoupling and gain-scheduling improve the performance of the PI controller compared to the fixed-gain and uncompensated PI controller. However, tracking is still not accurate for the rising and falling part (phase current commutation) of the phase current reference.

5.2.3 Hysteresis Controller

The simplest of all nonlinear controllers is the hysteresis controller. Most researchers have used hysteresis controller for SRM current control. Hysteresis controllers are very popular for their conceptual simplicity, ease of implementation using analog electronic circuits and high dynamic performance. The controller tries to keep the phase current within the hysteresis band of the current reference signal, by applying either full positive voltage or full negative voltage. This type of controller is also called a bang-bang controller. For SRM, the phase winding inductance varies over a wide range between the unaligned and aligned rotor positions. Applying full DC-link voltage near the low-inductance unaligned position would result in fast rise or fall of the current. Such a controller is easily implementable with analog systems where the infinite sampling frequency ensures the current does not cross the hysteresis band. In a discrete time system, due to finite execution cycle time and hence finite sampling frequency, it may not be possible to achieve a narrow hysteresis band. Hence, such controller results in an unacceptable amount of current ripples. In [64], the authors have discussed these problems associated with digital hysteresis current controllers.

Fig.5.6, shows the reference and measured current for one phase, with a hysteresis current controller implemented on our experimental platform. With a sampling frequency of $3\,kHz$, and DC-link voltage of $100\,V$, and unaligned inductance of $L_u = 10\,mH$, the change of current between two consecutive sampling instants would be,

$$\triangle I = \frac{100 * 0.0001}{0.01} = 1.0\,A \tag{5.13}$$

As can be clearly seen, the change in current in one sample becomes as large as 1.0 A, with motor running at $200\,r/min$ under a load torque of $1\,N.m$. It can be seen that the Hysteresis current controller results in variable switching frequency, depending on the DC-link voltage, phase inductance and load current. This may cause acoustic noise problem.

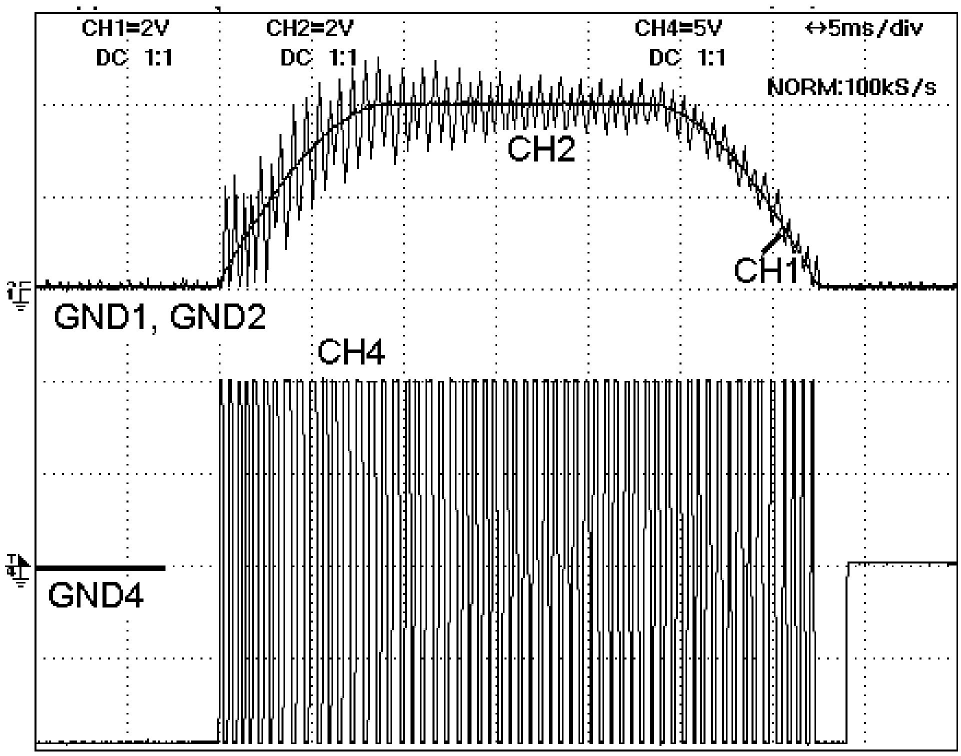

CH1 - Phase current reference (1A/Div)
CH2 - Measrued phase current (1A/Div)
CH4 -Phase voltage (50V/Div)

Figure 5.6: Current tracking performance of hysteresis controller, CH1(1 A/Div)-phase current ref, CH2(1 A/Div)-phase measured current, CH4(50 V/Div)-Phase voltage

Alternatively, if only the current controller is implemented in analog circuitry, while the TSF and $T \rightarrow i$ conversion are implemented digitally; satisfactory performance can be obtained. However, the overall control scheme with both analog and digital controllers becomes too complex. Therefore, hysteresis current controller is not best suited for high performance torque control of SRM.

5.3 Proposed SMC Based Current Controller

Sliding Mode control (SMC) is well known as a good control design method for reference tracking in nonlinear uncertain systems. This elegant control design method converts a higher-order tracking control problem into a first order stabilization problem. Given a general plant as in:

$$\dot{\mathbf{x}} = \mathbf{f} + \mathbf{b}u \tag{5.14}$$

where scalar x as the output of interest, the scalar u as the control input and $\mathbf{x} = [x\dot{x}\cdots x^{(n-1)}]^T$ is the state vector. For the single-input dynamic system, the control problem is to track a specific time-varying state in presence of model imprecision on $\mathbf{f}$ and $\mathbf{b}$. Let $\tilde{x} = x - x_d$ be the tracking error. A switching surface is defined as

$$s(\mathbf{x};t) = \left(\frac{d}{dt} + \lambda\right)^{n-1} \tilde{x} \tag{5.15}$$

λ is a strictly positive constant. The output tracking error $\tilde{x}$ is made to decay to 0 by keeping s at 0. If $|s(t)| < \phi$, then $|\tilde{x}| < \frac{\phi}{\lambda^{n-1}}$. A stabilizing controller for s can be designed using Lyapunov's method, which is valid for both nonlinear as well as linear systems. Let Lyapunov function be $V = \frac{1}{2}s^2$. By making $\dot{V} = s\dot{s} < -\eta\,|s|$ we get a stabilizing control with finite reaching time i.e. s will become zero in finite time irrespective of the initial position. The system's motion on the sliding surface can be interpreted as an average of the systems dynamics on both sides of the surface i.e. $\dot{s} = 0$. An equivalent control can be obtained, which is the continuous control law to maintain $\dot{s} = 0$.

Basically, the equivalent control compensates for known disturbances and the time-varying references. This compensation is accurate only when the nominal model matches the actual plant. However, this is often not the case for practical applications, and additional feedback control is needed to obtain a stable dynamics for s. Assuming the deviation of the actual equivalent control from the model estimated control voltage is bounded and the bound is known:

$$|\hat{u}_{eq} - u_{eq}| < M \tag{5.16}$$

where M is a known finite value, a discontinuous switching control is designed to achieve robust stability *i.e.* $s\dot{s} < -\eta\,|s|$ at all time. Then total control effort becomes:

$$u = \hat{u}_{eq} - W\,sgn(s) \tag{5.17}$$

where $W = (M + \frac{\eta}{\hat{b}_{min}})$. The signum function $sgn(.)$ is defined as:

$$\begin{aligned} sgn(s) &= +1, \text{ if } s > 0 \\ &= -1, \text{ if } s < 0 \end{aligned} \tag{5.18}$$

However, implementing such a switching control is not possible in digital systems with finite sampling frequency, where it leads to large oscillations. Hence, a saturation type feedback control is often used in place of such a switching control law, as shown in the following section.

5.3.1 Linear Flux-linkage Model Based SMC

5.3.1.1 Equivalent control

For current tracking control, $x_d = i^*$ and $x = i$. As seen from (5.2), the system is of first order and $s = \tilde{x} = i^* - i$. Equivalent voltage can be obtained solving $\dot{s} = \dot{x}_d - \dot{x} = \dot{i}^* - \dot{i} = 0$. Hence, the equivalent control voltage is:

$$v_{eq} = \frac{\partial \psi}{\partial i}\dot{i}^* + Ri + \frac{\partial \psi}{\partial \theta}\frac{d\theta}{dt} \tag{5.19}$$

The equivalent voltage compensates for resistive drop, back-emf and the time rate of change of phase current reference.

Taking advantage of the robustness property of SMC, we propose to use a simplified model for SRM, assuming linear magnetization. This model requires number of stator/rotor poles, stator/rotor pole arcs, and linearized phase inductance at rotor aligned and unaligned positions. Stator phase inductance $L(\theta)$ as shown in Fig.1.4, is given in (1.8). With the approximate linearized model for stator phase inductance, (5.19) can be rewritten as follows:

$$\hat{v}_{eq} = L(\theta)\frac{di^*}{d\theta}\omega + iR + Ki\omega \tag{5.20}$$

The actual phase inductance under saturation will be different from the assumed linearized phase inductance. So the equivalent control alone can not keep the current tracking error at zero. This calls for additional feedback control effort to force the error back to zero.

5.3.1.2 Switching control

According to sliding mode control theory, a variable structure control effort as shown in Fig.5.7(a) should be used for ensuring the system to be in sliding mode. This high-gain and high-frequency feedback control is the source of the well known robustness of SMC. The magnitude of the switching voltage W depends on the bounds of disturbances. A few difficulties in practical realization of this control scheme are :

- Due to limited bandwidth of digital controllers and some actuators, such a high-frequency control is often not possible.

- Such high-gain controller may excite unmodelled dynamics. For example, the dynamics of anti-aliasing filters in digital control systems may become significant and can no longer be ignored. If ignored, the output may become oscillatory.

To avoid these drawbacks, a saturated type of control was proposed and used by many researchers. Often, in practical systems, it is good enough to have the error within a tolerance and need not be exactly zero. Hence, a continuous but saturated controller as in Fig5.7(b) is popular in place of the switching control. Once the value of W is known from the bound of known disturbances, the feedback gain in the linear part of the saturated controller will determine the width of the error boundary. This will ensure the error to return to within the error boundary in finite time. A narrow error boundary can be obtained with a higher feedback gain. However, when implemented digitally, too high a feedback gain may result in oscillation. Thus, depending on the accuracy of the nominal model, there will be a limit to the level of accuracy of current tracking.

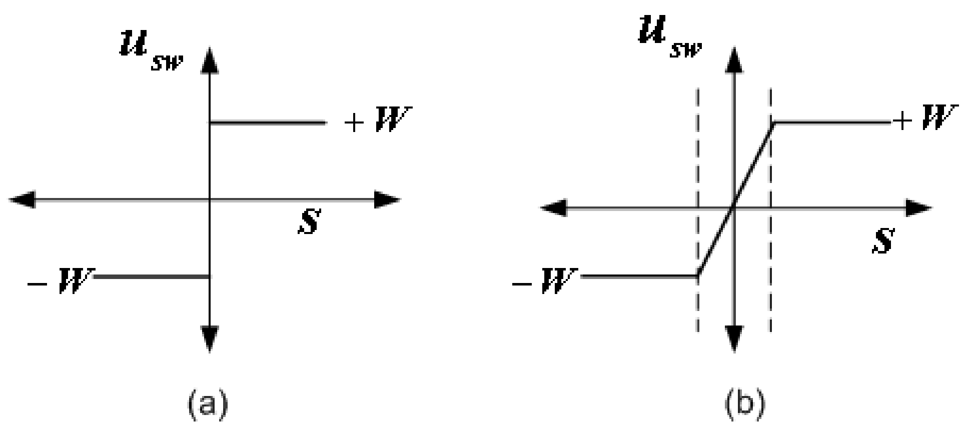

Figure 5.7: (a) Discontinuous switching control, (b) Saturated switching Control

The value of W can be obtained from the actual SRM magnetization data. To avoid this, we propose to use a constant feedback gain in place of the switching control as given in the block diagram in Fig.5.8. This gain is tuned on-site. To start with, a small gain is used which may result in a large tracking error. Then, the feedback gain is increased to improve the tracking performance until the current starts to become oscillatory. Experimental results for the proposed SMC based current control scheme are provided in the following section.

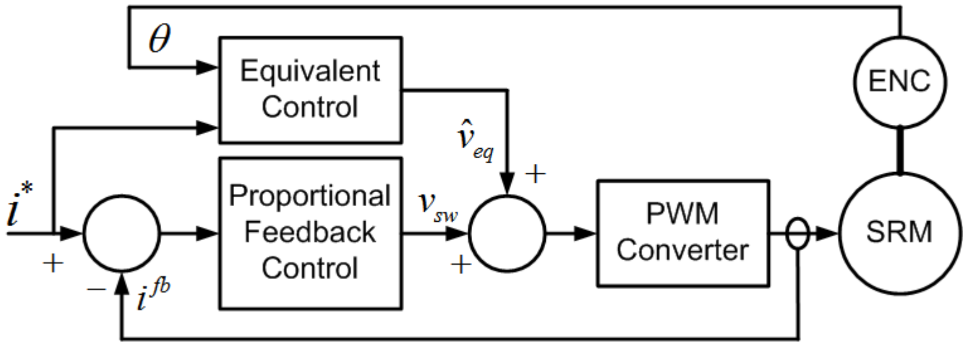

Figure 5.8: Block diagram of the proposed SMC based current controller

5.3.2 Experimental Results

The proposed current tracking control scheme has been experimentally verified on the laboratory set-up. A separately excited DC machine in series with an additional variable DC power supply with a resistive load bank act as load on the SRM. The DC supply voltage is varied to apply the desired load on the system. A dSPACE DS1104 controller board was used for implementing the control algorithm. Program execution takes 200 μs. The controller has a sampling frequency of 5 kHz.

Fig.5.9 shows the performance of the SMC based current controller for motor demanded torque of 0.4 $N.m$. CH1 shows the phase current reference, CH2 shows the measured phase current, CH3 shows the phase equivalent voltage and CH4 shows the phase feedback voltage. The current reference has a peak value of 2.3 A. There is a very good tracking of current. Most of the phase voltage is from the

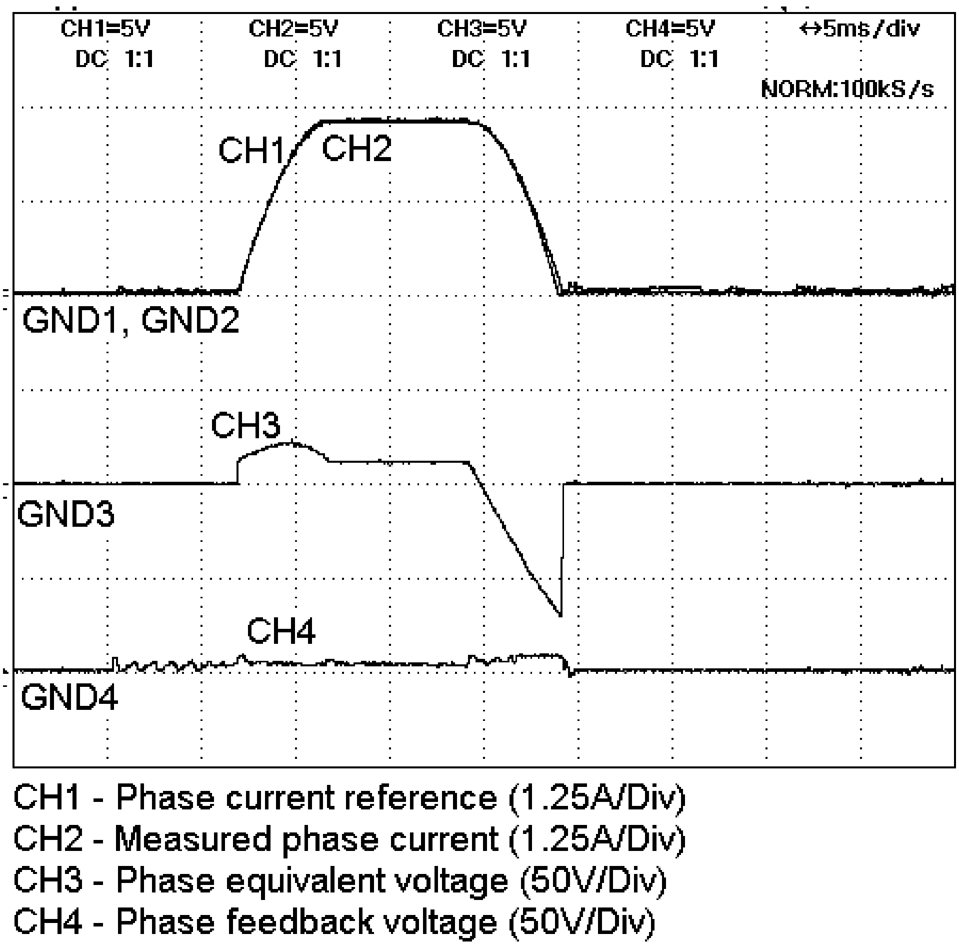

Figure 5.9: Current tracking performance of SMC with saturation type switching control

equivalent control part and the phase feedback voltage is quite small.

It is noted that the equivalent control in SMC requires the reference trajectory to be differentiable. However, the torque-to-current conversion scheme using ILC based compensation results in a current reference that is not differentiable. SMC based current controller can not be used for such schemes. Hence, an IDTC scheme using the proposed SMC based current controller was not developed.

5.4 Proposed ILC Based Current Controller

It is well known from control theory that a feed-forward control scheme improves the trajectory tracking performance. If an accurate plant model is available, such a feed-forward controller alone can achieve perfect tracking. However, it is difficult to obtain such an accurate model for SRM magnetization characteristics. To overcome this, a novel *iterative learning* based current controller has been implemented first proposed in [29]. In [29], simulation results provided for the ILC based feed-forward current controller. In this thesis work, a feedback controller is added to improve the performance of the controller during the period when ILC has not converged yet. Fig.5.10 shows the block diagram of the proposed current controller, consisting of a simple P-type feedback controller and an ILC block as the feed-forward controller. The detailed structure of the ILC part is shown in Fig.5.12.

Iterative learning controller(ILC) takes advantage of the periodic nature of an operation and learns the required control input for realizing the desired output trajectory. The basic mechanism behind learning is to store the control input and plant output error, for each operation cycle. The control inputs are updated according to a learning law, which ensures that the error is reduced from cycle to cycle until the desired level of accuracy is achieved.

5.4.1 Implementation of ILC-based Current Controller

For the prototype SRM, the phase inductance profile repeats itself after every 60^0, as shown in Fig. 5.11. The torque sharing function would convert the constant

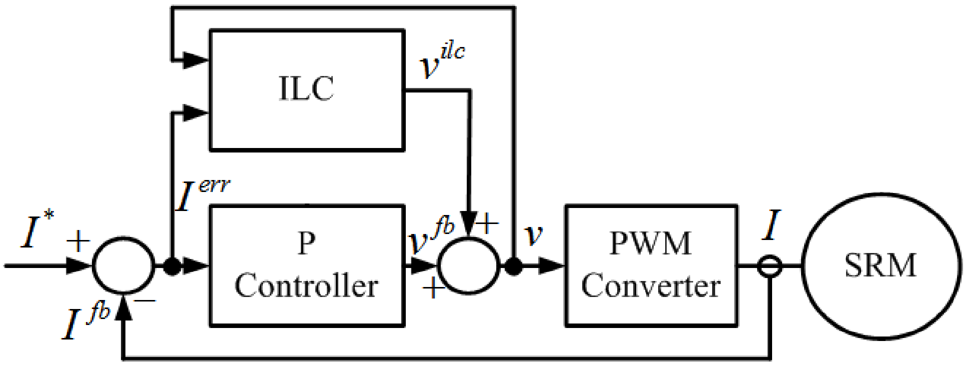

Figure 5.10: Block diagram for ILC based current controller

torque demand into a position dependent phase current reference, which repeats every 60^0. For constant speed and load torque, the phase current reference can be achieved by applying a position dependent voltage, which is periodic in nature. Thus, the controller has to learn this required voltage as a function of rotor position. We divide the 60^0 period into intervals of equal distance, such that required voltage profile can be approximated to be of constant value over each interval. During each sampling period, the error in current is calculated and stored in memory against the corresponding position interval, along with the voltage applied to the phase winding. One period(60 degrees) of the inductance profile is considered one learning iteration.

The TSF as shown in Fig.3.3, each phase is active for 30^0 with producing T^*_{inc} for first 15^0 and T^*_{dec} for the remaining 15^0. As phase windings are inactive for 30^0, there is enough time for actual current to be zero at the beginning of each period. Hence, resetting condition $I^*(m, 0) = I^*(m + 1, 0) = 0$, is satisfied for the phase current reference tracking problem; where m is the iteration number.

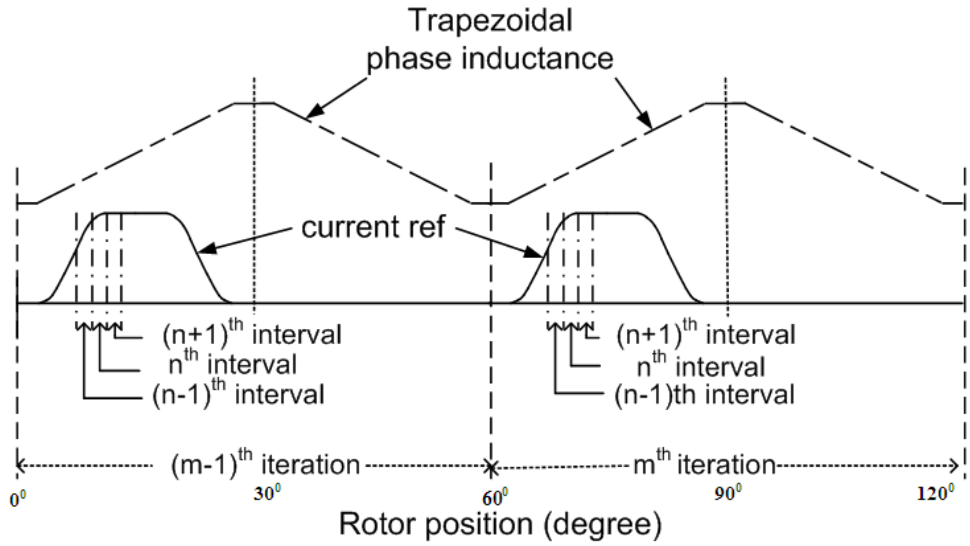

Figure 5.11: Learning iteration and position interval used in ILC learning law

5.4.2 ILC Updating Law

The ILC updating law for the current controller is:

$$v_{ilc}(m,n) = v_{ilc}(m-1,n) + G_1 * I^{err}(m-1,n+1) \tag{5.21}$$

where $v_{ilc}(m,n)$ is the ILC compensation voltage at the n^{th} rotor position during the m^{th} iteration, G_1 is the learning gain, and I^{err} is the current tracking error. Due to the dynamic relationship between the phase voltage and phase current, and the calculation delay in the discrete time system, current at $(n+1)^{th}$ position interval would correspond to the voltage applied at n^{th} position interval. In view of this, the ILC learning law uses the current error $I^{err}(m-1,n+1)$ in updating the voltage $v_{ilc}(m,n)$.

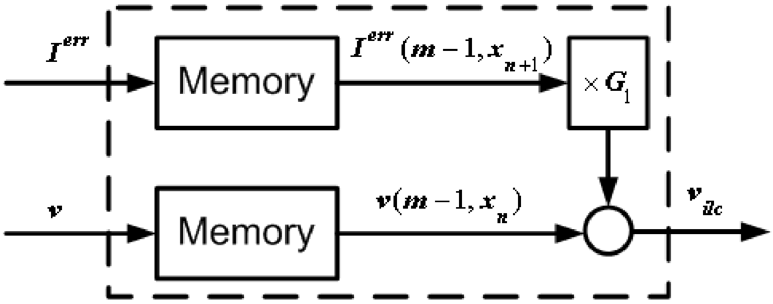

Figure 5.12: Block diagram for ILC updating law in current controller

5.4.3 ILC Convergence

In each iteration, ILC updates the control input by a quantity proportional to the error. This should result in reduction of tracking error from iteration to iteration. Error convergence is defined as reduction of tracking error to within a tolerable limit, after a number of such iterations. The learning gain is designed so as to ensure convergence. A large learning gain leads to faster error convergence. For a continuous time system given by:

$$\dot{x} = f + bu \tag{5.22}$$

and for an updating law:

$$u(k+1) = u(k) + G\,(x_d(k) - x(k)), \tag{5.23}$$

the range of learning gain to ensure convergence is given by

$$|1 - Gb| \leq 1 \tag{5.24}$$

The current dynamics at a given rotor position is:

$$\frac{di}{dt} = -\frac{Ri + K\omega i}{L(\theta)} + \frac{1}{L(\theta)}v \tag{5.25}$$

where $K = \frac{dL}{d\theta}$ is the rate of change of phase inductance with rotor position, and ω is motor speed. Hence, the range for G_1 for error convergence is determined from following inequality,

$$\|1 - \frac{G_1}{L(\theta)}\| \leq 1 \Rightarrow 0 \leq \frac{G_1}{L(\theta)} \leq 2 \Rightarrow 0 \leq G_1 \leq 2L(\theta) \tag{5.26}$$

For the prototype SRM used in this thesis work, $0.01 < L(\theta) < 0.1$. Hence, learning gain is varied with rotor position and is within the range of $0.02 < G_1 < 0.2$. In practical implementation, it is advisable to start with a learning gain somewhere in lower end of the range and observe the convergence speed and stability. From there, it can be increased for improving the convergence speed, until system behavior becomes unstable. Else, the learning gain can be decreased to improve the stability but sacrificing the convergence speed.

5.4.4 P-type Feedback Control

During dynamic conditions, like when the system is tracking a speed setting or change in load, the torque reference may be changing and hence the current reference will not be repetitive. As ILC is tuned to converge after certain number of iterations, it may not be fully effective during transient period. The P-controller is tuned to give the best possible tracking performance on its own, to take care of such situations. As soon as the torque reference stabilizes, the ILC further improves the current tracking. Thus the two parts of the proposed controller are equally important in the overall performance of the current controller.

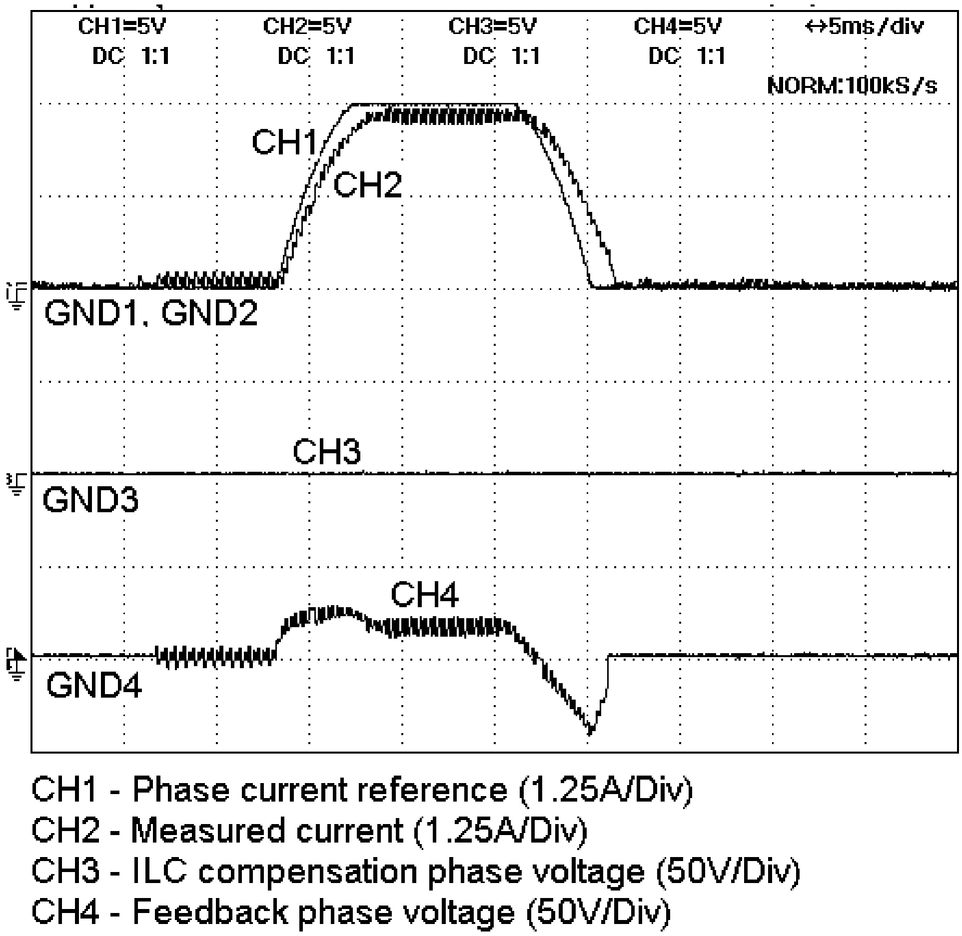

Figure 5.13: Current tracking performance of P-type current controller: motor demanded torque = 0.5 N.m

5.4.5 Experimental Validation of Proposed Current Control Scheme

The proposed current controller has been implemented on the experimental set-up. The relative significance of both the P-type feedback and ILC compensation are discussed.

To show the contribution of ILC compensation to the accuracy of current control, only P-type feedback based is used at first. The motor demanded torque is set at $0.5\,N.m$ and the DC supply voltage is set so as to get an equilibrium at

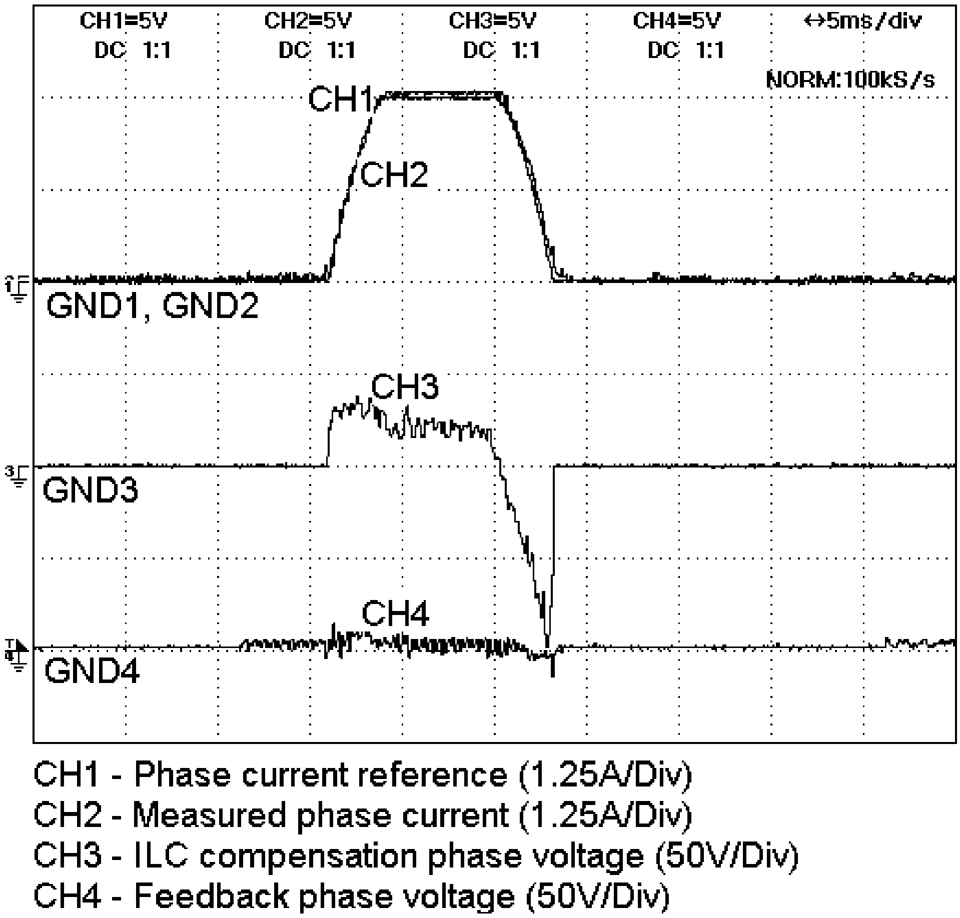

Figure 5.14: Current tracking performance of P-type current controller with ILC compensation: motor demanded torque = 0.5 N.m

about 250 $r/\min$. Fig.5.13 shows the phase current reference (CH1) and measured phase current (CH2) for P=50. ILC compensation has not been activated as can be seen in CH3. CH4 shows the feedback control part of the phase voltage, which is proportional to the tracking error. There is a large tracking error, particularly in the increasing and decreasing parts of the phase current reference.

When ILC is activated,the current tracking error is almost eliminated as can be seen in Fig.5.14, where CH1 is the current reference and CH2 is the measured current. The ILC compensation phase voltage in CH3 is the major contributor of the phase voltage, where as the feedback phase voltage shown in CH4 is almost

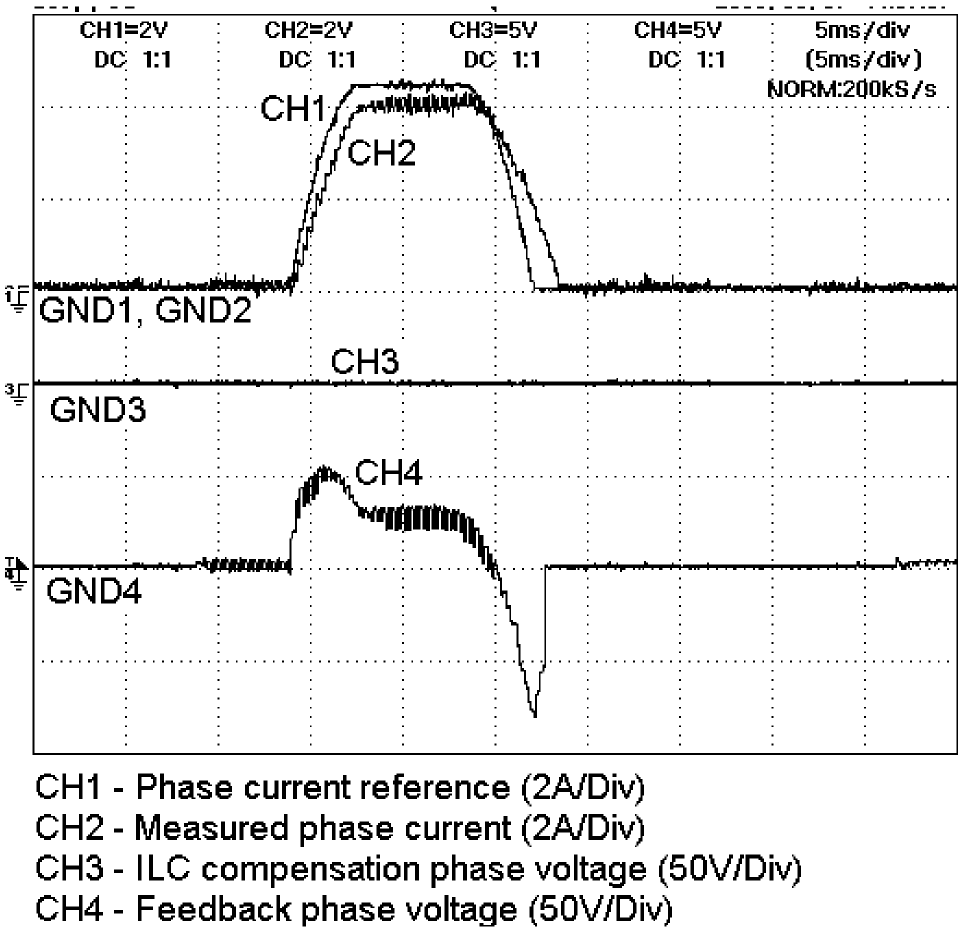

Figure 5.15: Current tracking performance of P-type current controller: motor demanded torque = 1.5 N.m

negligible. The motor demanded torque is at 0.5 $N.m$ and the motor steady-state speed is about 250 rpm.

Next, ILC based current controller is tested for a motor demanded torque of 1.5 $N.m$. As can be seen Fig5.15: CH1 and CH3, with P-type feedback controller, the current tracking error is quite large. There is no ILC compensation (CH3) and hence feedback control voltage(CH4) is the only component of the phase voltage. When ILC is activated, as seen in Fig.5.16, the current tracking error is quite small. It can be concluded that the proposed ILC based current controller gives good steady-state tacking performance for any value of the motor demanded torque.

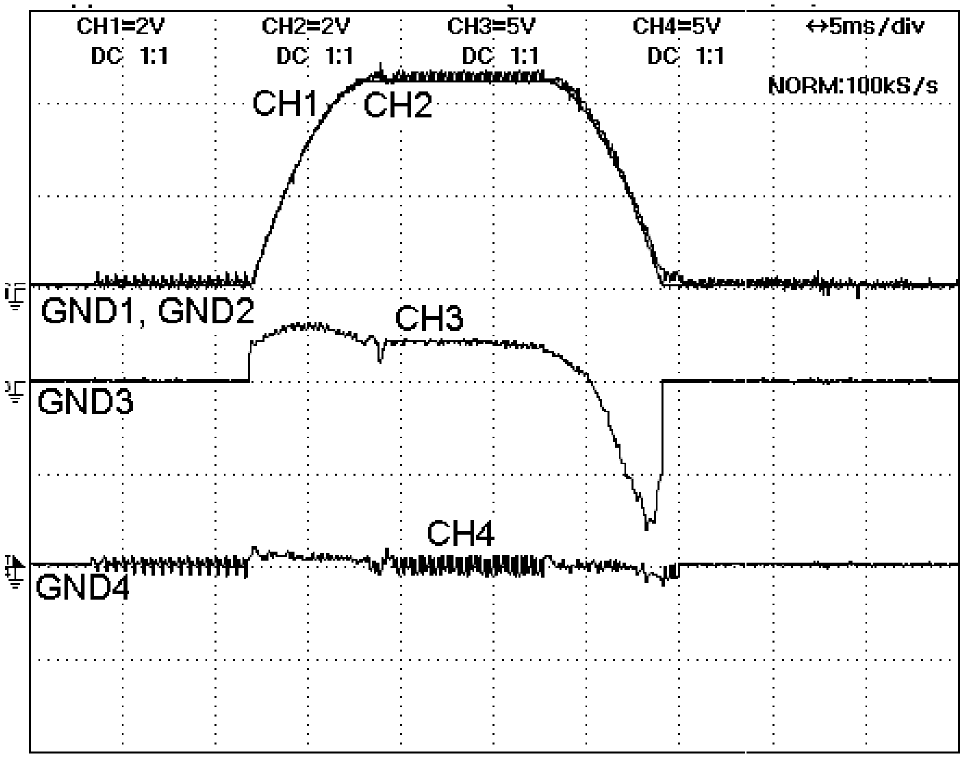

CH1 - Phase current reference (2A/Div)
CH2 - Measured phase current (2A/Div)
CH3 - ILC compensation phase voltage (50V/Div)
CH4 - Feedback phase voltage (50V/Div)

Figure 5.16: Current tracking performance of P-type current controller with ILC compensation: motor demanded torque = 1.5 N.m

Fig.5.17 shows the error convergence performance for the learning gain $G_1 = 0.1$. As it can be seen from CH3, tracking error convergence takes three to four cycles to fall within a small value.

5.5 ILC based IDTC

For indirect torque control (IDTC) of SRM to be accurate, it is required that both torque-to-current conversion and current tracking are accurate. The ILC based torque-to-current conversion scheme discussed in Chapter 4 can be combined with

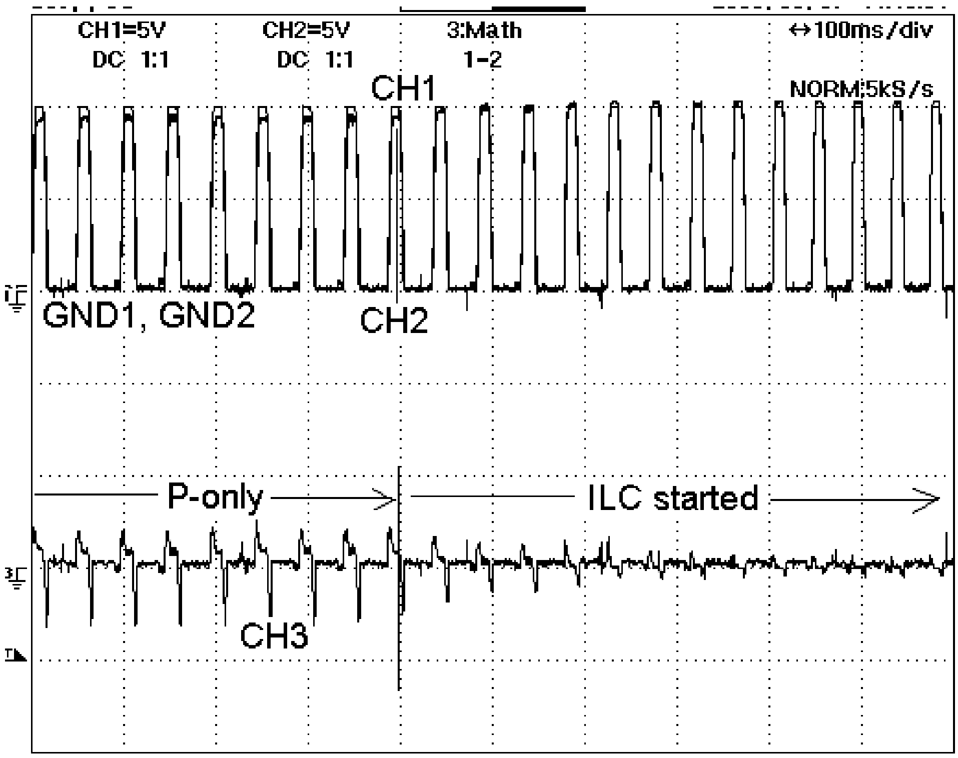

CH1 - Phase current reference (1.25A/Div)
CH2 - Measured phase current (1.25A/Div)
CH3 - Current tracking error (1.25A/Div)

Figure 5.17: ILC convergence time for proposed ILC based current controller compensation: motor demanded torque = 0.5 N.m

the ILC based current tracking controller to design an ILC based indirect torque controller.

5.5.1 Experimental Verification of the ILC based IDTC Scheme

Fig.5.18 shows the experimental results for this ILC based indirect torque controller. In Fig.5.18, CH2 is the phase current reference for demanded motor torque of 1 $N.m$, and is CH3 is measured phase current. As can be seen from this figure, the current tracking performance is quite good. The estimated motor torque as

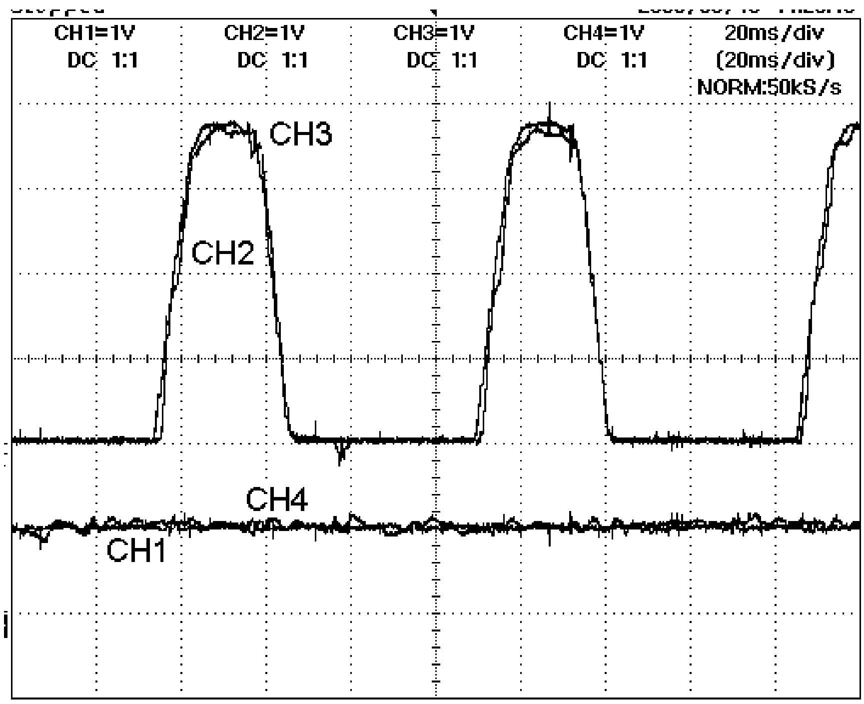

Figure 5.18: Performance of ILC based indirect torque controller for SRM, at load torque of 1 N.m and motor speed of 150 r/min, CH1(1 N.m/Div)-estimated total torque for the current reference, CH2(1 A/Div)-measured Current, CH3(1 A/Div)-current reference with compensation, CH4(1 N.m/Div)-estimated total torque for the actual current

shown by (Fig.5.18,CH4) matches the demanded torque of 1 $N.m$ quite well. This experimental figure demonstrates the overall effectiveness of the proposed IDTC scheme, which produces the desired while torque ripples are within 10% of the average torque output.

5.5.2 Disadvantage of the ILC based IDTC Scheme

It is noted that the ILC based IDTC scheme will have two ILC blocks cascaded together. To ensure proper convergence of the system, the ILC blocks must not be allowed to interact. For this, the ILC for torque-to-current conversion is activated first until the equivalent current reference is obtained. Then, the ILC for the current controller is activated to improve the current tracking performance. This process makes the ILC based IDTC scheme slow in terms of convergence. This problem is overcome in the next chapter when a single ILC based direct torque controller is developed.

5.6 Summary

This chapter presents the results of investigation on a high-performance current controller for SRM drives. At first, various types of current controllers for SRM proposed in literature are evaluated. Their performance has been experimentally verified. In view of the absence of any established current controller for SRM in the literature, a novel current controller is proposed using *iterative learning control*. The scheme does not require accurate model knowledge of the motor. ILC is an intelligent control method which exploits the periodicity of phase current reference. It is suitable for applications with more emphasis on steady-state ripple-free torque generation. Finally, an indirect torque control scheme has been implemented by combining the ILC based torque-to-current conversion and an ILC based current tracking controller. However, the use of two ILCs leads to complexity in controller design and operation. An ILC based direct torque control scheme (DTC) scheme is discussed in the next chapter to overcome this problem.

Chapter 6

Direct Torque Control for SRM using Spatial Iterative Learning Control

In the previous chapter, an indirect torque controller was shown based on iterative learning control (ILC). ILC is simple for both design and implementation and quite effective in reduction of the torque ripples when motor torque demand and motor speed are constant. As mentioned in last chapter, the two ILC blocks in the proposed indirect torque control scheme can not be active simultaneously. The outer-loop ILC for torque-to-current conversion has to converge first before the inner-loop ILC for current controller is activated. This prolongs the overall time for convergence. Secondly, implementation of the two ILC blocks requires double the memory required for one ILC block. To overcome this problem, direct torque control (DTC) strategy is proposed. The DTC scheme treats phase torque as plant output and generates the desired phase voltage directly, as shown in Fig.6.2. A novel spatial ILC based DTC scheme has been presented in this chapter.

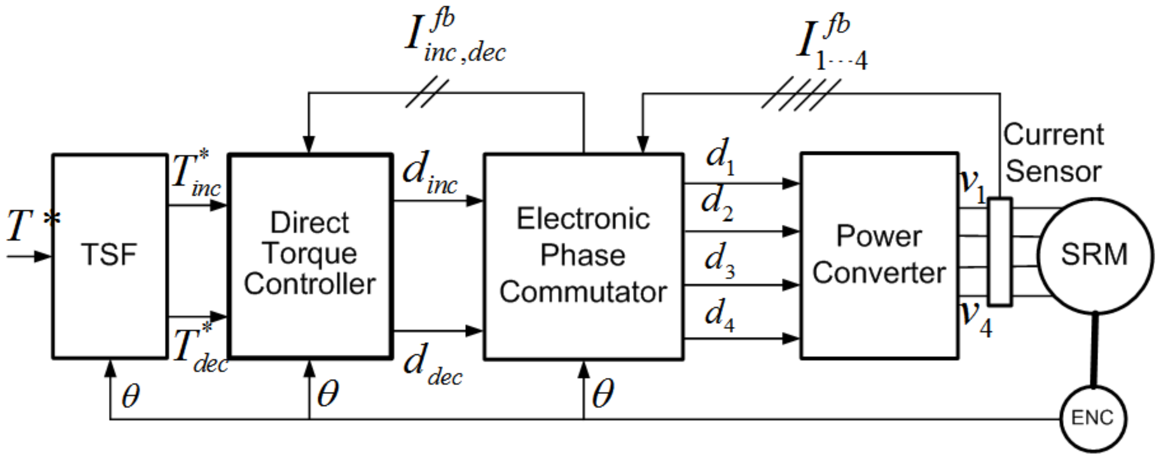

Figure 6.1: Direct torque controller for SRM

6.1 Past Works on Direct Torque Control of SRM

Direct torque control (DTC) scheme does not need to convert the torque references to equivalent current references. DTC was introduced [70]-[71] in the late 1980s for AC drives. A detailed survey on DTC was done in [72]. The defining characteristics of DTC are : 1) there is no need for obtaining an equivalent current reference for given motor torque, and 2) no current controller is required.

A hysteresis type DTC for SRM had been reported in [73]. Hysteresis controller applies full DC link voltage to the phase winding and hence requires very high sampling frequency to keep the output torque within a narrow band of the reference. Any digital controller implementation requires an anti-aliasing filter, which is basically a low-pass filter. This filter adds a phase lag to the feedback signal, and hence the change in current may not show in the feedback immediately. Due to this reason, a high-gain feedback controller will give rise to an oscillatory output.

The controller should apply a smoothly variable voltage between $-V_{dc}$ and $+V_{dc}$ to track the torque reference smoothly, as also agreed by other researchers in [87]. A pulse-width-modulated (PWM) converter can be used to supply the variable voltage to the SRM. In [87], Neuhaus *et al.* have proposed to use flux-linkage as the control variable and use predictive, dead-beat control to achieve instantaneous torque control. However, conversion of phase torque to phase flux-linkage using a look-up table is not a direct torque control scheme as such. Secondly, estimation of flux-linkage from phase voltage integrating the volt-seconds is prone to error.

6.2 Proposed Spatial ILC-based DTC Scheme

ILC is well known for improving output tracking accuracy in uncertain nonlinear systems, when the task is periodic. An ILC based DTC scheme is proposed as shown in Fig.6.2. The torque model developed in Chapter 2 as given in (2.23) is used as the torque estimator. The estimated phase torque is compared with the phase torque reference to obtain the torque error (T^{err}). The proposed DTC scheme is similar to the ILC-based current tracking controller proposed earlier. There is a simple P-type feedback controller and ILC controller is added onto it. ILC voltage is updated based on the torque error by an updating law to be shown later.

6.2.1 Phase Torque Periodic in Rotor Position

Each phase torque reference is decided by the motor torque demand and torque sharing function (TSF). For a constant motor torque demand, phase torque refer-

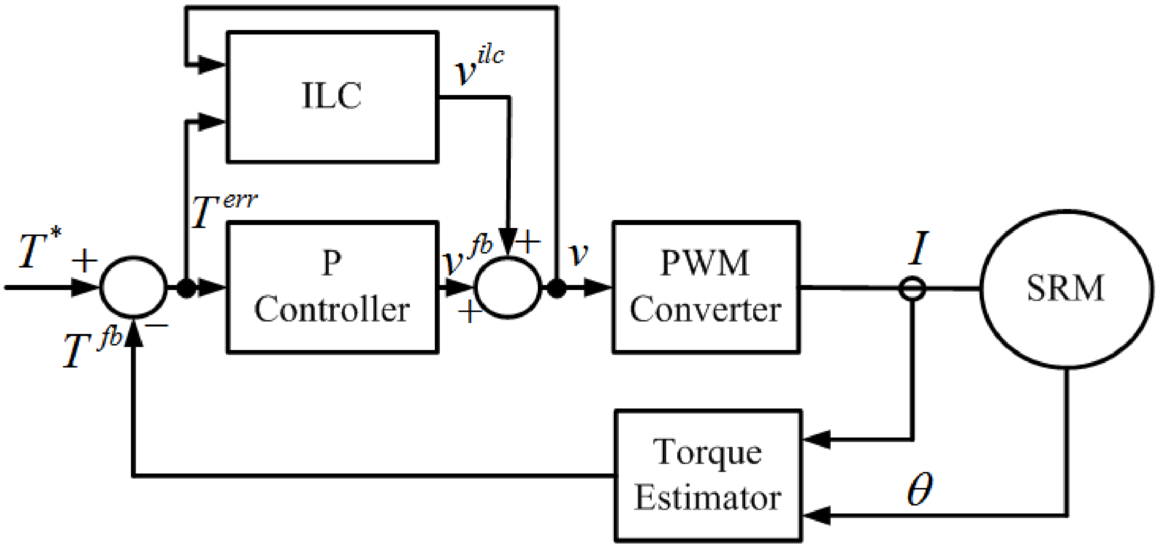

Figure 6.2: ILC based DTC scheme for SRM

ence will be periodic in *rotor position*, but not necessarily in time as speed may be varying. To cater for variation in speed, the ILC for the proposed DTC scheme has to be analyzed, designed and implemented in terms of rotor position, rather than time.

As shown in Fig.3.3 for TSF, each phase is active for 30^0 with producing T^*_{inc} for first 15^0 and T^*_{dec} for the remaining 15^0. As phase windings are inactive for the subsequent 30^0, there is enough time for actual phase torque to be zero at the beginning of each period. Hence, the resetting condition $T^*(m,0) = T(m+1,0) = 0$, where m is the iteration number, is satisfied for the phase torque tracking problem.

6.2.2 Implementation of the Spatial ILC Scheme

Usually, a digital controller samples the plant output at fixed time intervals and calculates the control input during the period between the sampling instants. The

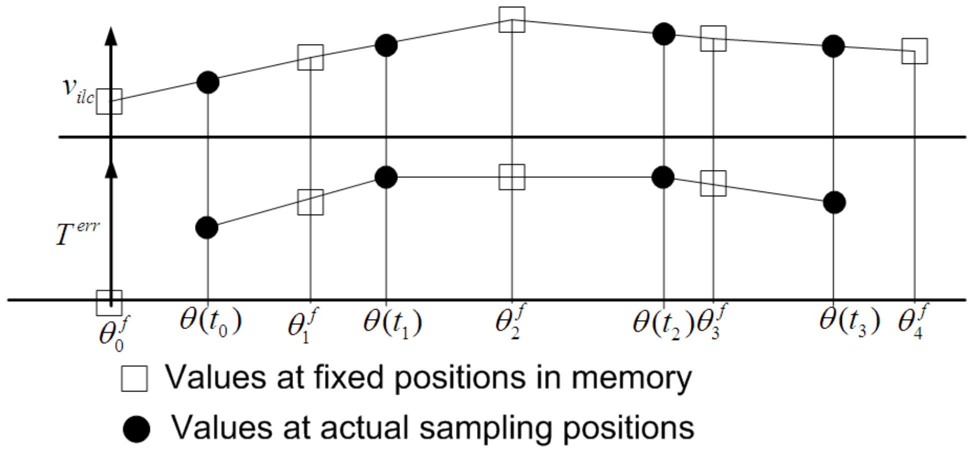

Figure 6.3: Description of position based ILC: θ_n^f-fixed rotor positions in memory, $\theta(t_n)$-rotor positions at sampling instants during an iteration, v_{ilc}-the ILC compensation voltage, T^{err}-torque tracking error

distance travelled by the rotor between two sampling instants will depend on the rotor speed. As motor accelerates or decelerates, the distance between two consecutive sampling instants will not be constant. Fig.6.3 describes the position based ILC implementation. The difference between the rotor positions $\theta(t_n)$ and $\theta(t_{n+1})$ at two consecutive time samples t_n and t_{n+1} in Fig.6.3 may vary for different values of n. Secondly, as the number of samples in one period (15^0) may not be an integer number. Hence, rotor positions at sampling instants will not be identical in all iterations. However, iterative learning control requires the operation to be repetitive and hence updating of compensation voltage has to be at identical rotor positions in all learning cycles. To overcome this problem, a set of equidistant rotor positions (θ_1^f, θ_2^f, θ_3^f etc.) are fixed per period i.e. between 0^0 to 15^0 as shown in Fig.6.3. The compensation voltages (v_{ilc}) and torque error (T^{err}) at each sampling instant (t_n), represented in Fig.6.3 as filled circles, are mapped to the fixed rotor positions (θ_n^f) represented by the empty squares; through linear interpolation. Linear interpolation is used for its simplicity, as the distance between two consecutive sampling instants will be small at low rotor speed.

$$T^{err}(m, \theta_n^f) = T^{err}(m, \theta(t_b)) + \frac{T^{err}(m, \theta(t_a)) - T^{err}(m, \theta(t_b))}{\theta(t_a) - \theta(t_b)}(\theta_n^f - \theta(t_b)) \quad (6.1)$$

where $T^{err} = T^{ref} - T$ is the tracking error, m is the m^{th} iteration number, θ_n^f is the n^{th} fixed position, $\theta(t_b)$ is the sampled position just before θ_n^f, $\theta(t_a)$ is the sampled position just after θ_n^f. ILC compensation voltage is updated using the ILC updating law:

$$v_{ilc}(m, \theta_n^f) = v_{ilc}(m-1, \theta_n^f) + G_3 * T^{err}(m-1, \theta_{n+1}^f) \quad (6.2)$$

where $v_{ilc}(m, \theta_n^f)$ is the ILC compensation voltage at the n^{th} fixed position in memory during the m^{th} iteration, G_3 is the learning gain, $\theta(t)$ the rotor position at sampling instant t, θ_b^f is the fixed position in memory just before $\theta(t)$ and θ_a^f is the fixed position in memory just after $\theta(t)$. Finally, the ILC compensation voltage for the sampling instant t, is obtained from the compensation voltages stored in memory as given by:

$$v_{ilc}(m, \theta(t)) = v_{ilc}(m, \theta_b^f) + \frac{v_{ilc}(m, \theta_a^f) - v_{ilc}(m, \theta_b^f)}{\theta_b^f - \theta_a^f}(\theta(t) - \theta_b^f) \quad (6.3)$$

6.2.3 ILC Convergence

In each iteration, ILC updates the control input by a quantity proportional to the error. This should result in reduction of tracking error from iteration to iteration. Error convergence is defined as reduction of tracking error to within a tolerable limit, after a large number of such iterations. The learning gain is designed so as to ensure convergence. Given a continuous time representation of a system as in (5.3), its discrete-time representation of the system can be obtained in the form:

$$x(n+1) = F(n) + B(n)u(n) \quad (6.4)$$

where $x(n)$ is the value of the state variable at the n^{th} sampling instant. The ILC convergence criteria for such a system is given in [63] as:

$$|1 - G_3 B| < 1 \tag{6.5}$$

where G_3 is the learning gain.

Using the rectangular method for converting the continuous-time system into discrete-time system, we get:

$$\dot{x} = \frac{x(n+1) - x(n)}{T_s d} => x(n+1) = x(n) + T_s * \dot{x} \tag{6.6}$$

where T_s is the sampling time for the system. For the torque dynamics (first order), as the learning is done at fixed rotor positions, the sampling (T_{sd}) time to be used in discretization of the torque dynamics will be speed dependent, i.e.

$$T_{sd} = \frac{\theta^f_{k+1} - \theta^f_k}{\omega} \tag{6.7}$$

This T_{sd} is different from the actual sampling time of the digital controller which is constant. The discrete form of the torque dynamics will be:

$$\begin{aligned} T(\theta^f_{n+1}) &= T(\theta^f_n) + \frac{\partial T}{\partial \theta}(\theta^f_{n+1} - \theta^f_n) \\ &+ \frac{\partial T}{\partial i}\left(\frac{\partial \psi}{\partial i}\right)^{-1}\left(-iR - \frac{\partial \psi}{\partial \theta}\omega\right) T_{sd} \\ &+ \frac{\partial T}{\partial i}\left(\frac{\partial \psi}{\partial i}\right)^{-1} T_{sd}\, v(n) \end{aligned} \tag{6.8}$$

Thus, for the discrete-time torque dynamics,

$$B = \frac{\partial T}{\partial i}\left(\frac{\partial \psi}{\partial i}\right)^{-1} T_{sd} \tag{6.9}$$

Hence, the convergence criteria for the proposed spatial ILC is obtained as:

$$0 \leq G_3 \leq \frac{2}{\frac{\partial T}{\partial i}\left(\frac{\partial \psi}{\partial i}\right)^{-1} T_{sd}} \tag{6.10}$$

Accurate knowledge of torque and flux-linkage model is not necessary for accurate tracking of phase torque. Approximate values are required to obtain the learning gain. A trapezoidal phase-inductance profile as given in (1.8) for the SRM can be used for this purpose. With $K = \frac{dL}{d\theta}$ being the slope of the assumed phase inductance vs. rotor position, the torque equation becomes simpler and a range for the learning gain can be obtained as follows:

$$\begin{aligned} T &= \frac{1}{2}Ki^2 \Rightarrow \frac{\partial T}{\partial i} = Ki \\ \psi(i,\theta) &= L(\theta)i \Rightarrow \frac{\partial \psi}{\partial i} = L(\theta) \end{aligned} \tag{6.11}$$

Then, the range for the learning gain for convergence of ILC for the DTC scheme can be obtained from:

$$0 \leq G_3 \leq \frac{2\,L(\theta)}{K\,I_{rated}}\frac{\omega}{\triangle\theta}. \tag{6.12}$$

For the prototype SRM, $L_u = 0.01$, $K = 0.10$, $I_{rated} = 10\,A$,and taking $\omega \simeq 1$ for motor speed of $10\,r/min$ and $\theta = 0.1^0$; we get the $G_3 \simeq 11$. This will be a very conservative gain for the system. However, the learning gain should be varied with rotor position to account for the trapezoidal variation of approximated phase inductance.

6.2.4 Zero-phase Low-pass Filter Design

As seen in previous subsection, ILC based controller does not require an accurate model for SRM magnetization, but only approximate values like linearized inductance profile is good enough. The learning gain is designed from this easily available information on its phase inductance characteristics to guarantee error convergence. However, in practical implementation, possible noise in torque feedback will affect the tracking performance. A low-pass filter can be implemented to filter out any high-frequency noise in torque estimation. A 'non-causal zero-phase filter' is implemented to avoid phase delay due to the low-pass filter. A non-causal zero-phase filter is feasible in ILC applications due to the storage of tracking error signals in memory for computation of control voltage. The following equation is of generic form for a zero-phase filter

$$T^{err}_{filtered}(k) = \frac{1}{2N+1} \sum_{i=-N}^{N} T^{err}(k+i) \tag{6.13}$$

which has a gain vs. frequency response:

$$H(\theta) = \frac{sin\left(\frac{(2N+1)\theta}{2}\right)}{sin(\frac{\theta}{2})} \tag{6.14}$$

where $\theta = 2\pi \frac{f}{f_s}$, with f_s as sampling frequency and f as the frequency of interest.

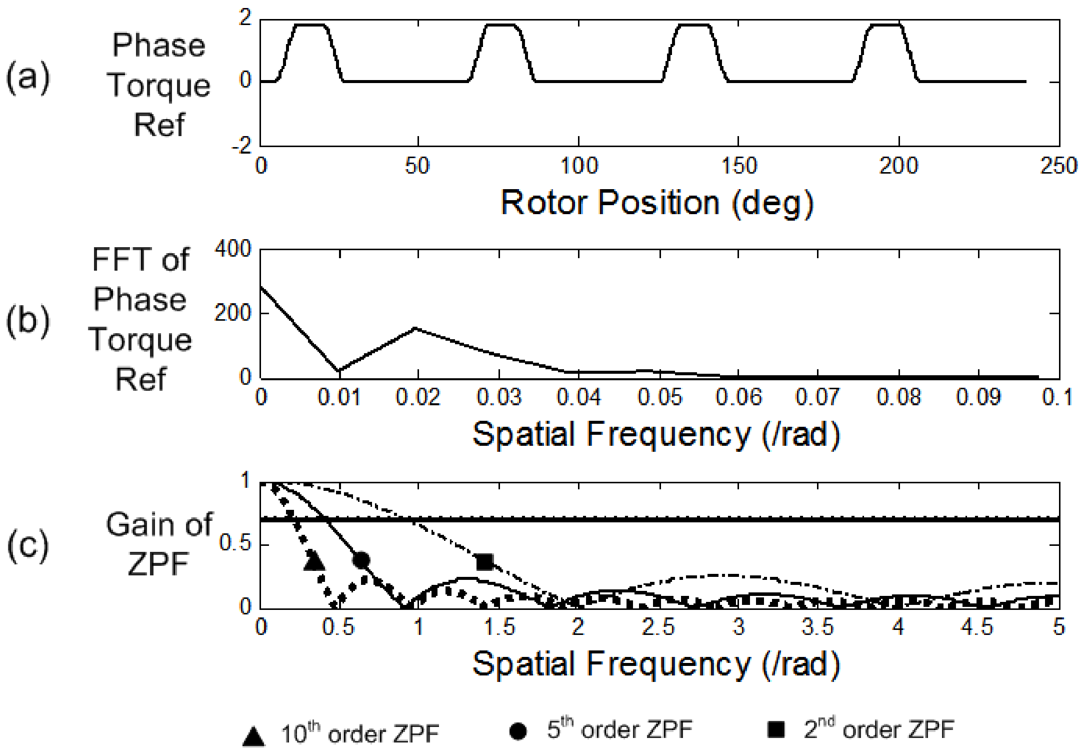

Figure 6.4: FFT of phase reference torque for the cubic TSF and zero-phase low-pass filter characteristics: (a)-phase torque reference vs rotor position, (b)- FFT of phase torque reference, (c)-gain vs spatial frequency of various order zero-phase low-pass filters

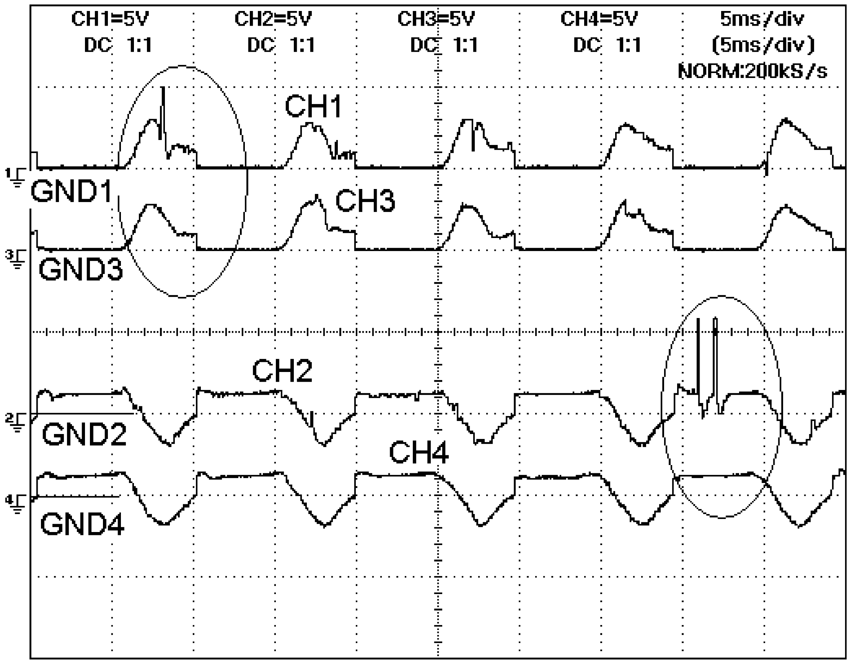

CH1 - Tracking error of the increasing phase (0.5 Nm/Div)
CH2 - Tracking error of the decreasing phase (0.5 Nm/Div)
CH3 - Filter output for increasing phase error (0.5 Nm/Div)
CH4 - Filter output for decreasing phase error (0.5 Nm/Div)

Figure 6.5: Experimental verification of a fifth-order zero-phase low-pass filter for torque tracking error

Before designing the low-pass filter, the spatial frequency content of the phase torque reference is obtained through FFT. Unlike the conventional FFT, the phase torque reference is sampled at equidistant rotor positions (position samples 0.1^0 apart), and then the FFT is obtained along spatial frequency. With the phase torque reference as in Fig.6.4(a), the FFT for phase torque reference is shown in Fig.6.4(b). The gain-vs-frequency plots for zero-phase filters of second order, fifth order and tenth order are shown in Fig.6.4(c). A fifth order zero-phase filter has been chosen in this thesis work which has a cut-off frequency at about 20 times the largest frequency component present in the phase torque reference.

Phase torque is estimated from measured phase current and rotor position, using the torque model (2.23) and (2.23) shown in Chapter 2. Due to the highly nonlinear nature of this model, a small noise in measurement of rotor position or phase current leads to a large spike in estimated phase torque and hence the estimated value of the phase torque error. This can be seen in CH1(for the increasing phase) and CH2(for the decreasing phase) in Fig.6.5. Such large amount of noise in torque estimation may lead to divergence of the ILC learning. However, application of the fifth order low-pass filter can eliminate this spikes in estimated torque error, as can be seen in Fig.6.5. CH3 shows the filtered torque error for the increasing phase and CH4 shows the filtered torque error value for the decreasing phase. It can also be noted that CH3 is in phase with CH1 and CH4 is in phase with CH2. This demonstrates the zero-phase lag behavior of the proposed low-pass filter, which is critical in ensuring learning convergence of the proposed DTC scheme.

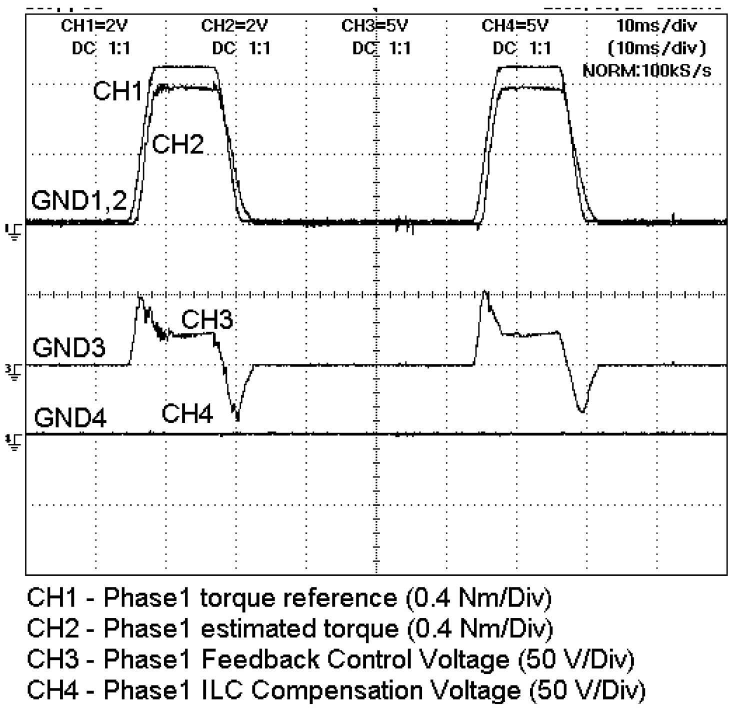

Figure 6.6: Reference torque, estimated torque, voltage and current with only the P-type feedback torque controller for phase1; motor demanded torque 0.9 N.m.

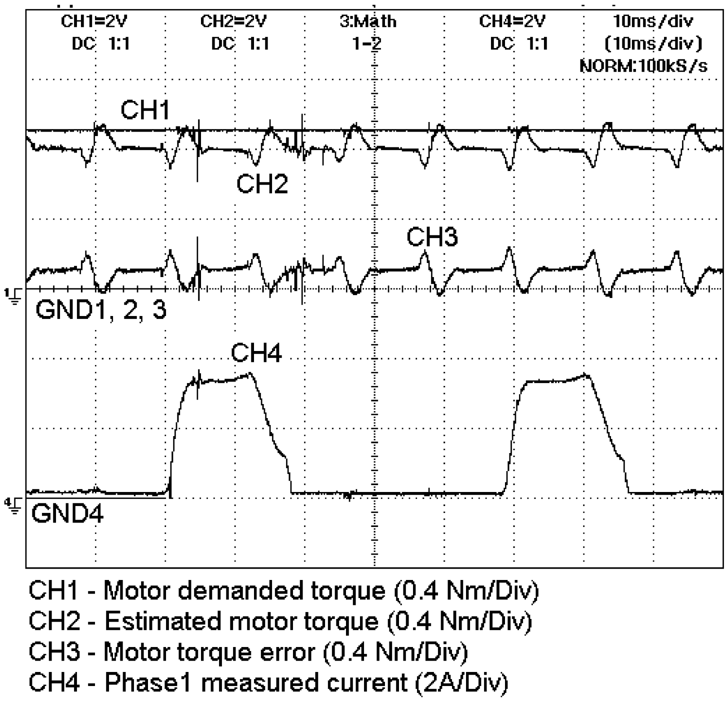

Figure 6.7: Motor demanded torque, estimated motor torque, torque error and phase1 current with only the P-type feedback torque controller; motor demanded torque 0.9 N.m.

6.3 Experimental Validation of the Proposed ILC-based DTC Scheme

The proposed DTC scheme has been experimentally verified on the laboratory set-up. The program execution takes 150 μs. The torque control loop has a sampling frequency of 6.6 kHz.

A high gain feedback controller is the simplest possible controller for nonlinear plants. Hence, at first the P-type feedback controller is tuned to get the best possible performance. The P-type feedback gain is increased until the torque output becomes oscillatory. Then, ILC compensation is activated. The ILC learning gain G_3 is varied with the rotor position as per (6.12). The experimental results are

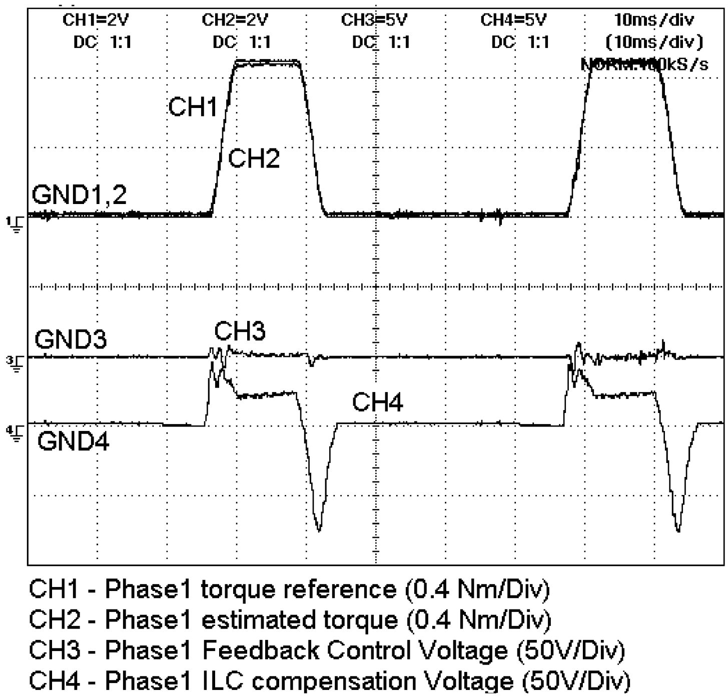

Figure 6.8: Phase1 reference torque, estimated torque, voltage and current with P-type feedback controller and ILC compensation; motor demanded torque 0.9 N.m.

presented in pair where one figure shows the relevant quantities for one phase winding like; phase torque reference, estimated phase torque, phase torque tracking error and the ILC compensation voltage for the phase. The other figure in the pair shows the quantities like demanded motor torque, estimated total motor torque, estimated motor torque error, and measured current in phase1.

The P-gain is set to 150 as any further increase makes the torque output oscillatory near the unaligned rotor position. The motor demanded torque was first set at 0.9 $N.m$ i.e 50% of rated torque, with motor speed being around 200 r/min. Fig.6.6 shows the phase1 torque reference (CH1) and estimated torque for phase1 (CH2). There is substantial phase torque tracking error with the P-type controller alone. The phase1 feedback control voltage (CH3) is proportional to the torque tracking error, but the ILC compensation voltage (CH4) is zero. With only the

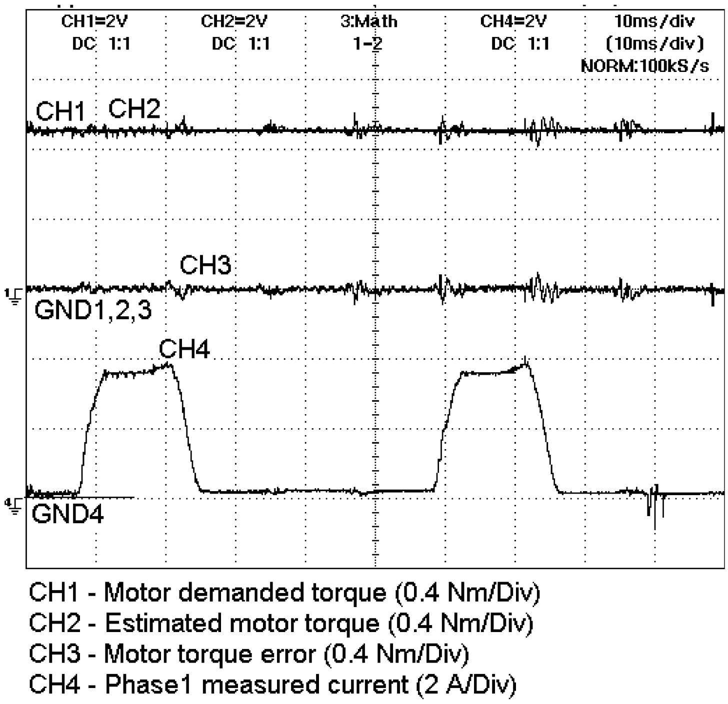

Figure 6.9: Motor torque reference, estimated torque and torque error with P-type feedback controller and ILC based compensation; motor demanded torque 0.9 N.m.

P-controller, there is a large average torque error as well as large peak-to-peak torque ripples. In Fig.6.7, CH1 shows the motor demanded torque, CH2 shows the estimated motor torque and CH3 shows the motor torque error. Thus, the average torque error is about 0.12 $N.m$ and the torque ripples are about 0.3 $N.m$ peak-to-peak or about 33 % of the demanded motor torque. In Fig.6.7, CH4 shows the measured phase1 current, which is controlled automatically within the rated current limit of 10 A.

Then, for the same operating conditions, ILC compensation is activated, in addition to the P-type feedback controller. The results for this experiment are shown in Fig.6.8 and Fig.6.9. As can be seen from the matching of Fig.6.8 CH1 and CH2, the phase1 torque tracking is quite accurate, after ILC has converged. The phase feedback control voltage is almost zero as there is no tracking error and

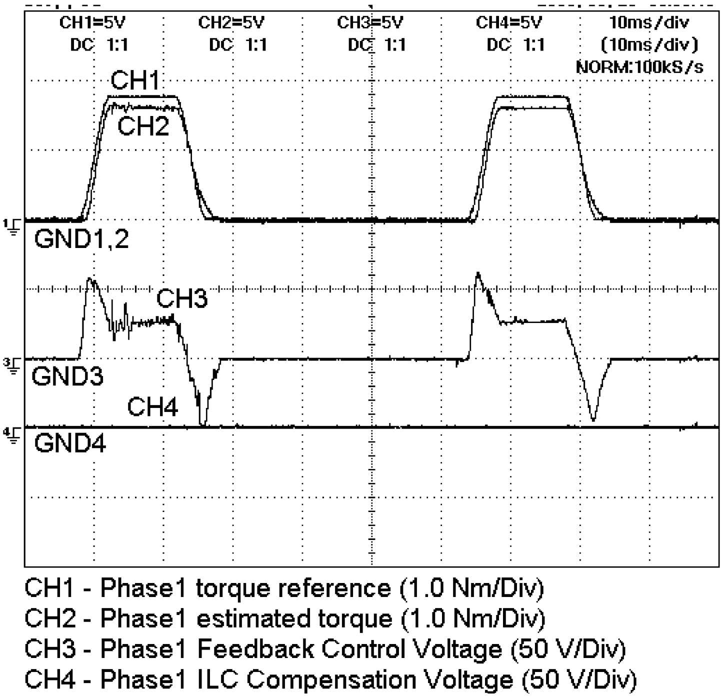

Figure 6.10: Phase1 reference torque, estimated torque, voltage and current with only the P-type feedback torque controller; motor demanded torque 1.8 N.m.

the ILC compensation voltage becomes the major part of the control voltage when ILC has converged. Also, the error in motor torque; both its average value and torque ripples are almost eliminated as can be seen in Fig.6.9 (CH3). Again, the phase current stays limited within the rated limit, without any current controller.

The proposed DTC scheme is then tested at 1.8 $N.m$ of motor torque, which is the rated torque for the prototype SRM. The previous experiment is repeated for this torque level, while keeping the motor speed around 170 r/min. At first, only the P-type feedback controller is activated. Fig.6.10 shows the results of phase1 torque tracking and control voltages. The feedback control voltage is proportional to the torque tracking error. It can be seen that with a P-type controller alone, the feedback control voltage (CH3) and the tracking error (difference between CH1 and CH2) are higher for motor torque level of 1.8 $N.m$ as compared to 0.9 $N.m$.

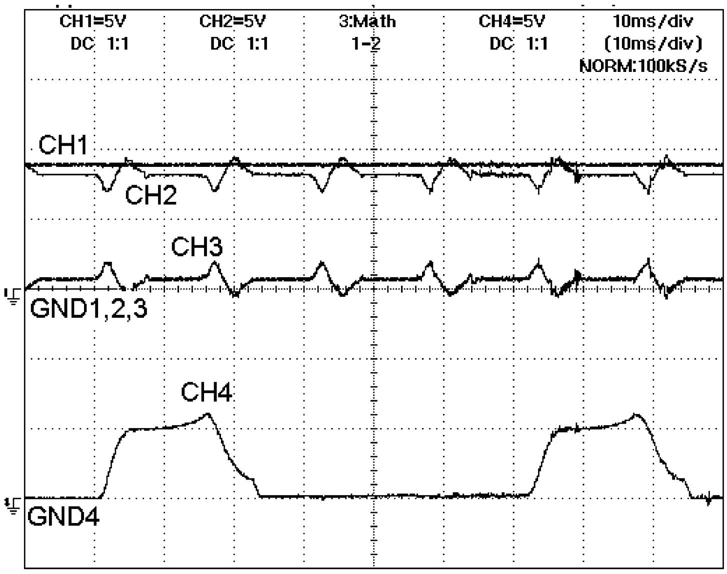

CH1 - Motor demanded torque (1.0 Nm/Div)
CH2 - Estimated motor torque (1.0 Nm/Div)
CH3 - Motor torque error (1.0 Nm/Div)
CH4 - Phase1 measured Current (5 A/Div)

Figure 6.11: Motor demanded torque, estimated motor torque, torque error and phase1 current with only the P-type feedback torque controller; motor demanded torque 1.8 N.m.

The peak-to-peak torque ripples are about $0.4\,N.m$ or about $22\,\%$ of the demanded motor torque, as can be seen from Fig.6.10 CH3. Even though the peak-to-peak value of torque ripples is higher at $1.8\,N,m$, the percentage is lower due to the increased base. The phase1 measured current for rated torque is now has a peak value of about $6\,A$.

Again, the results for both the P-type feedback controller and ILC together for the DTC scheme are shown in Fig.6.12 and 6.13. In Fig.6.12 both CH1 and CH2 are closely matching and hence phase torque tracking looks very good. The feedback control voltage for phase1 (CH3) is reduced drastically and ILC compensation voltage (CH4) is the main part of the control voltage. In essence, the ILC part takes over the control task and acts as an accurate feed-forward controller. Correspondingly, the total motor torque matches the demanded torque accurately

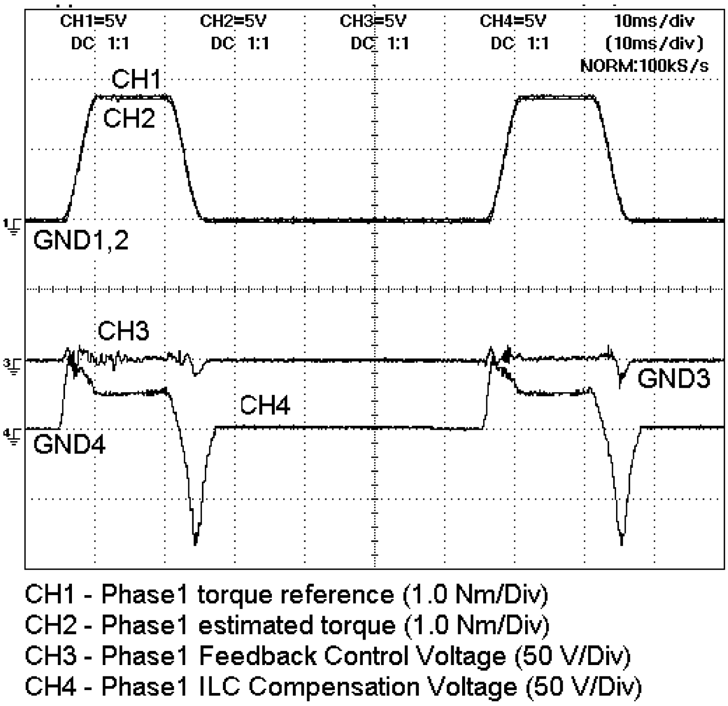

Figure 6.12: Phase1 reference torque, estimated torque, voltage and current with P-type feedback controller and ILC compensation; motor demanded torque 1.8 N.m.

as can be seen from CH1 and CH2 of Fig.6.13. The average torque error is almost zero and the peak-to-peak torque ripples are less than 0.1 $N.m$. These results demonstrate that proposed controller can provide accurate torque control for a constant motor torque reference, for any torque level, when motor speed is around 200 r/min. The torque ripples are reduced to approximately 5% of average torque, for low speed operations.

6.4 Summary

In this chapter, a spatial ILC based DTC scheme for SRM was shown. Unlike the ILC based indirect torque control scheme, the DTC scheme has only one ILC block. The ILC scheme has been analyzed, designed and implemented in position

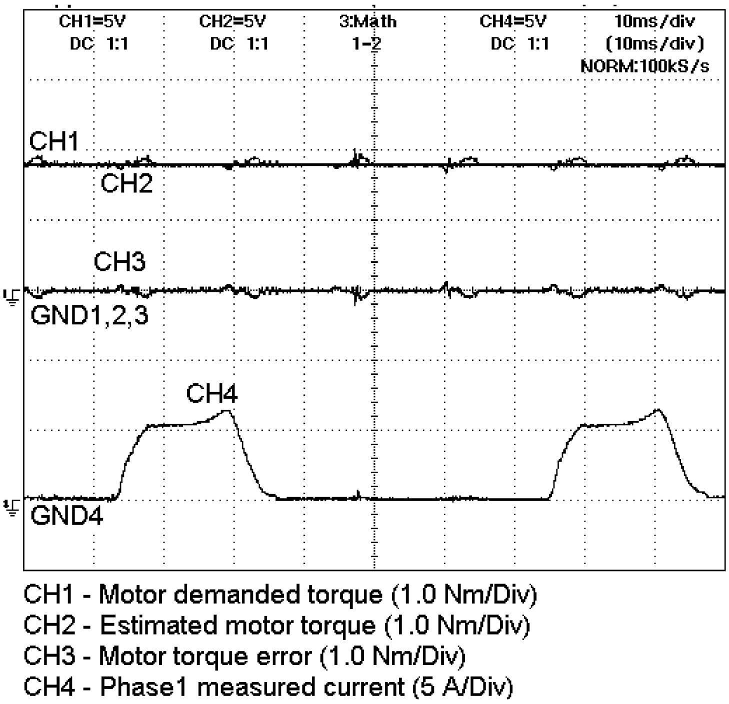

Figure 6.13: Motor torque reference, estimated torque and torque error with P-type feedback controller and ILC based compensation; motor demanded torque 1.8 N.m.

domain, considering the position periodicity of phase torque reference. This allows the application of ILC for varying speed applications, as long as motor demanded torque remains constant. The ILC-based DTC scheme does not require accurate SRM model. Only the linearized phase inductance profile is used for obtaining the learning gain. A zero-phase low-pass filter is added to the torque-estimator output to improve the robustness of ILC convergence. The proposed scheme is verified on the prototype SRM. Experimental results demonstrate the effectiveness of the scheme on for different loads, for low speed operation. Torque ripples could be reduced to about 5 % at rated motor torque.

Chapter 7

Direct Torque Control for SRM using Nonlinear Robust Tracking Control

In previous chapter, ILC based DTC scheme was shown to be quite simple in concept and design. However, the scheme is applicable when demanded motor torque is constant. This constraint ensures the periodicity of phase current references which in turn is essential for application of ILC. However, in most servo applications (e.g. pick-n-place); the motor has to accelerate, coast and decelerate. Then, the motor demanded torque is not constant but is variable according to a predetermined position/velocity trajectory. As the ILC based DTC scheme is not applicable, there is a need to find another suitable nonlinear torque control scheme for such applications. Model-based nonlinear control technique such as feedback linearization [76] requires an accurate plant model. As modelling of SRM magnetization characteristics is difficult and prone to error due to manufacturing tolerances, the controller should be robust to model inaccuracies.

A novel direct torque control scheme for switched reluctance motor (SRM) drive is discussed in this chapter, using nonlinear robust tracking control (NL-RTC). SRM magnetization characteristics is highly nonlinear, where torque is a complex and coupled function of phase current and rotor position. Direct torque control (DTC) scheme avoids the complex torque-to-current conversion required in indirect torque control scheme. Traditional DTC scheme uses a hysteresis type controller and leads to large amount of torque ripples when implemented in digital controller. Accurate tracking of fast changing references in nonlinear plants is possible by applying a model-based feed-forward control. However, a feedback control is necessary to compensate for any model uncertainties. NLRTC uses this principle for achieving accurate torque control with DTC scheme for SRM. A simple method is proposed and implemented for varying the feedback gain, which improves the tracking accuracy further. Experimental results shown for the prototype SRM, demonstrate the effectiveness of the scheme.

7.1 Proposed Nonlinear Robust Tracking Controller

Direct torque control for SRM phase torque is a first order nonlinear reference tracking problem. It can be converted to a stabilizing controller for the torque tracking error, $e = T^{err}$, which is the difference between the reference torque and estimated motor torque. Such a controller can be designed using Lyapunov's direct method. A Lyapunov function $V = \frac{1}{2}e^2$ is defined. To ensure error stability, $\dot{V}$ is made negative definite, i.e. $\dot{V} = e\dot{e} < 0$. This can be obtained by making $\dot{e} = -\lambda e$, with $\lambda > 0$.

A general nonlinear system dynamics can be represented by:

$$\dot{x} = f + bu \tag{7.1}$$

For asymptotic error stability while tracking a time-varying reference x_d, the desired control input u_d should be,

$$\begin{aligned} u_d &= b^{-1}(\dot{x_d} - f) + b^{-1}\lambda e \\ &= u_{ff} + u_{fb} \end{aligned} \tag{7.2}$$

This control input will result in stable dynamics for the tracking error. The u_{ff} compensates the varying reference and the system nonlinearity. However, it is often the case that instead of the accurate models, only approximate nominal models $\hat{f}$, $\hat{b}$ for f and b respectively, are available. Then model-based control $\hat{u}$ becomes:

$$\begin{aligned} \hat{u} &= \hat{b}^{-1}(\dot{x_d} - \hat{f} + \lambda e) \\ &= \hat{b}^{-1}(\dot{x_d} - \hat{f}) + \hat{b}^{-1}\lambda e \\ &= \hat{u}_{ff} + \hat{b}^{-1}\lambda e \end{aligned} \tag{7.3}$$

The difference in u_{ff} and $\hat{u}_{ff}$ due to model uncertainty needs to be compensated with additional feedback control to ensure stable tracking error dynamics. In absence of accurate model knowledge, a robust control design can be done where the bound on model is obtained instead and the additional feedback control of same amount is added. Let $||u_f - \hat{u}_{ff}|| = D$, then $u_{fb} = D * \frac{e}{e_b} + \hat{b}^-1\lambda e$. The *error bound*, e_b is defined as the error value beyond which the error dynamics is stable and hence the error magnitude will definitely be falling.

Fig.7.1 shows the block diagram for the proposed direct torque controller. It can be seen that direct torque controller calculates the duty cycle for the PWM converter from the torque reference without converting to equivalent current reference. It shows the two constituent parts of the NLRTC scheme: 1) feed-forward compensation control, and 2) feedback control. Following subsections will provide the details on the two components of control.

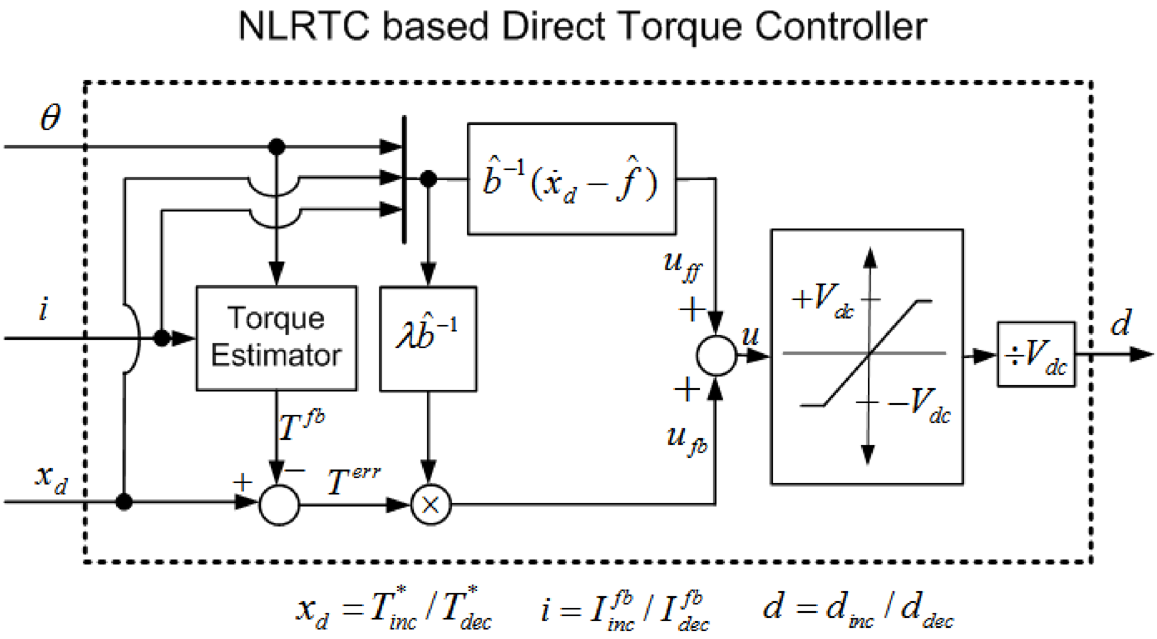

Figure 7.1: Details of NLRTC based direct torque control scheme

7.1.1 Nonlinear State Equations for DTC Scheme

In DTC scheme, phase torque is the plant output where as phase voltage v is control input. Torque $T(i,\theta)$ being a function of both phase current i and rotor position θ, torque dynamics was given in (2.11). For the sake of easy reference, it is re-written here:

$$\frac{dT}{dt} = \left(\frac{\partial T}{\partial i}\right)\left(\frac{\partial \psi}{\partial i}\right)^{-1}\left(-iR - \frac{\partial \psi}{\partial \theta}\frac{d\theta}{dt}\right) + \frac{\partial T}{\partial \theta}\frac{d\theta}{dt} + \left(\frac{\partial T}{\partial i}\right)\left(\frac{\partial \psi}{\partial i}\right)^{-1} v \tag{7.4}$$

Phase torque and phase current have a nonlinear but static relationship i.e. $T = g(i,\theta)$ and $i = h(T,\theta)$. Hence, flux-linkage $\psi(i,\theta)$ can be written as $\psi(T,\theta)$. Rewriting(7.4) in the form of general nonlinear state equation:

$$\dot{T} = f + bu \tag{7.5}$$

where,

$$f = \frac{\partial T}{\partial i}\left(\frac{\partial \psi}{\partial i}\right)^{-1}\left(-iR - \frac{\partial \psi}{\partial \theta}\frac{d\theta}{dt}\right) + \frac{\partial T}{\partial \theta}\frac{d\theta}{dt},$$

$$\begin{aligned} b &= \frac{\partial T}{\partial i}\left(\frac{\partial \psi}{\partial i}\right)^{-1} \\ u &= v \end{aligned} \tag{7.6}$$

As can be seen, the system dynamics are highly nonlinear and time-varying. Linear control design methods would not provide high dynamic performance. If accurate models for flux-linkage $\psi(i,\theta)$ and torque $T(i,\theta)$ are available, then the nonlinearities can be compensated by model based control techniques to obtain accurate tracking using linear control methods. As modelling SRM is still an open topic for research, an alternative robust control technique is investigated in this chapter for accurate torque control. Hence, a simple nominal model of SRM magnetization characteristics can be used for it.

7.1.2 Nominal Model for SRM Magnetization

To provide a feed-forward compensation, as can be seen from (7.4), the incremental inductance ($\frac{\partial \psi}{\partial i}$), back-emf constant ($\frac{\partial \psi}{\partial \theta}$) and partial derivative of torque with respect to phase current and rotor position are required. Measured flux-linkage data at different rotor position and phase current can be used to get estimations for these values as:

$$\frac{\partial \psi(i,\theta)}{\partial i}|_{i=i_1} = \frac{\psi(i_2,\theta)-\psi(i_1,\theta)}{i_2-i_1} \tag{7.7}$$

$$\frac{\partial \psi(i,\theta)}{\partial \theta}|_{\theta=theta_1} = \frac{\psi(i,\theta_2)-\psi(i,\theta_1)}{\theta_2-\theta_1} \tag{7.8}$$

where θ_1 and θ_2 are in *rad*.

As both $T(i,\theta)$ and $\psi(i,\theta)$ are continuous in both i and θ, by reordering the

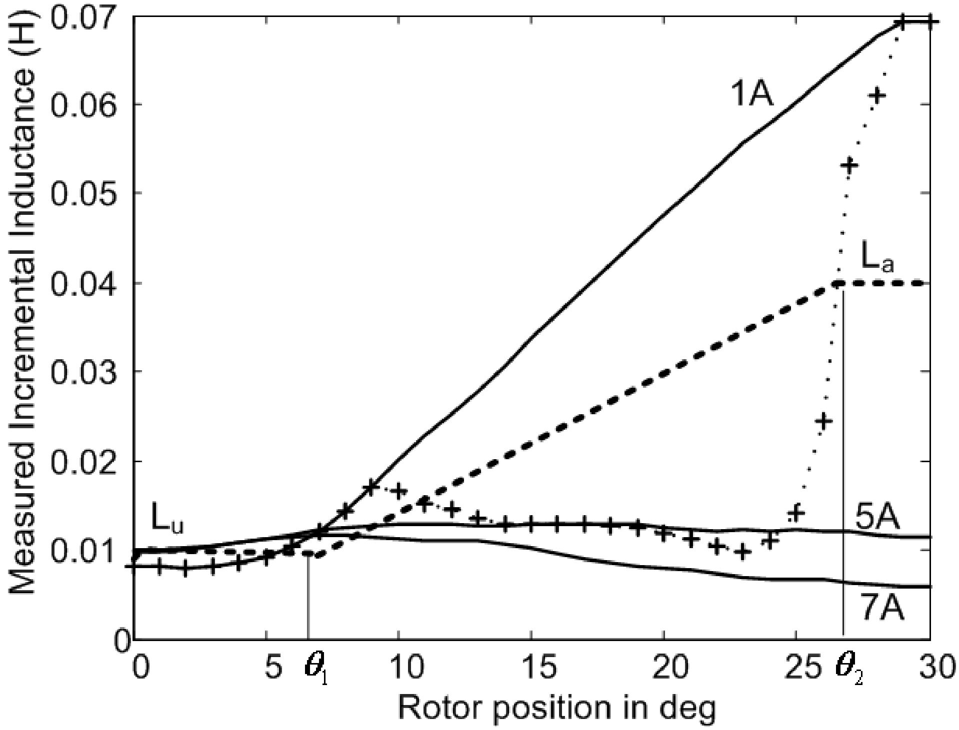

Figure 7.2: Estimated incremental phase inductance (solid lines); ..+.. shows variation of incremental inductance for demanded torque of 1.8 N.m; approximated trapezoidal phase inductance(dotted line) for prototype SRM at different current plotted vs rotor position for the 8/6 pole SRM, $\theta_1 = 7^0$, and $\theta_2 = 27^0$

differentiation and integration

$$\begin{aligned} T &= \frac{\partial}{\partial\theta}\int \psi di \\ \frac{\partial T}{\partial i} &= \frac{\partial}{\partial i}\left(\frac{\partial}{\partial\theta}\int \psi di\right) \\ &= \frac{\partial}{\partial\theta}\left(\frac{\partial}{\partial i}\int \psi di\right) \\ &= \frac{\partial\psi}{\partial\theta} \end{aligned} \tag{7.9}$$

Defining an 'effective torque constant' C_T so that

$$\begin{aligned} T(i,\theta) &= \frac{1}{2}C_T\, i^2 \\ \frac{\partial T}{\partial i} &= C_T\, i \\ C_T &= \frac{\partial T}{\partial i}\frac{1}{i} \end{aligned} \tag{7.10}$$

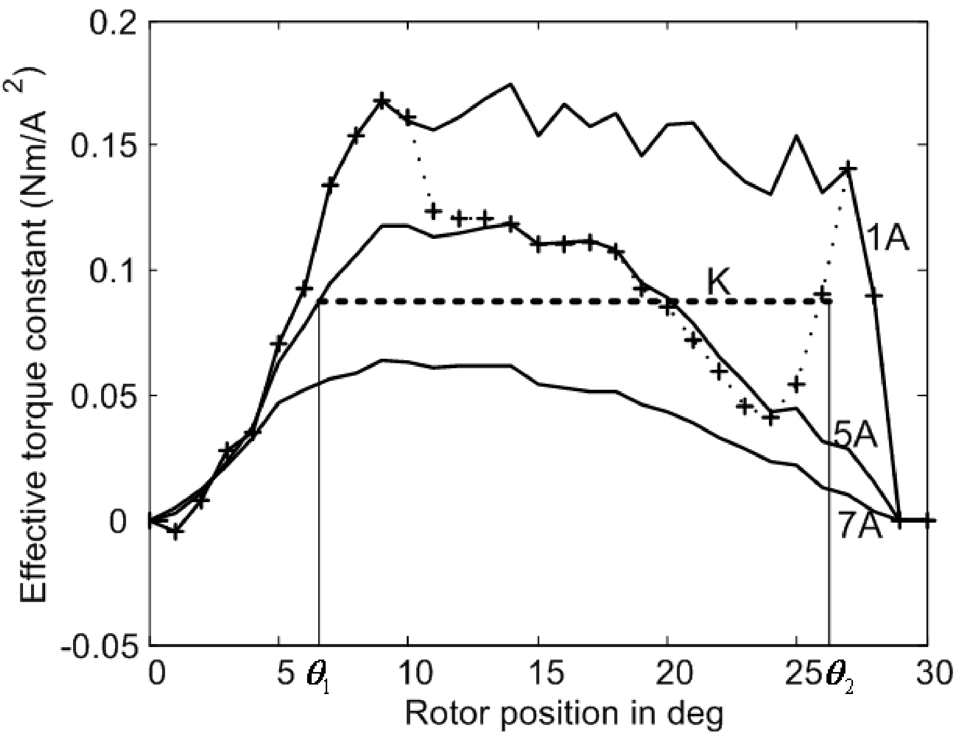

Figure 7.3: Estimated effective torque constant at three different current levels(solid lines); ..+.. shows variation of effective torque constant for demanded torque of 1.8 N.m; and approximated for trapezoidal inductance(dotted line) for prototype SRM at different current and rotor position, $\theta_1 = 7^0$, and $\theta_2 = 27^0$

Combining (7.9) and (7.10) can be rewritten as:

$$C_T = \frac{\partial \psi}{\partial \theta} \frac{1}{i} \tag{7.11}$$

This relation is used to estimate the C_T from the the measured flux-linkage data at different rotor position and phase current, as discussed in Chapter 2. Fig.7.2 shows the incremental inductance estimated from the measured flux-linkage for different current levels over the range of rotor positions. Fig.7.3 shows the *effective torque constant* C_T estimated from the measured flux-linkage data, at different current levels over $0^0 - 30^0$ in rotor position. As can be seen, both incremental phase inductance and effective torque constant vary with both phase current and rotor position in a highly nonlinear manner. However, the phase current in practice will not be constant over $0 - 30^0$, but will follow the TSF. If the TSF is defined with

$\theta_{on} = 7^0$ and $\theta_{ov} = 5^0$; then actual variation of incremental inductance and effective torque constant are shown for the rated torque of $1.8\,N.m$. For this work, the phase inductance can be approximated with a trapezoidal profile at around the middle of the range of variation. This is shown by the dashed line in Fig.7.2 given by (7.12). The corresponding approximation of effective torque constant will be the dashed line in Fig.7.3. Both these are represented by following analytical expressions:

$$\begin{aligned} L(\theta) &= L_u, \text{ for } 0^0 < \theta \leq \theta_1 \\ &= L_u + K\,\theta^{'}; \theta^{'} = (\theta - \theta_1), \text{ for } \theta_1 < \theta \leq \theta_2 \\ &= L_a, \text{ for } \theta_2 < \theta \leq\ 30^0 \end{aligned} \tag{7.12}$$

where L_u is the phase inductance at the unaligned rotor position, $K = \frac{dl}{d\theta}$ is the slope of the assumed phase inductance variation vs. rotor position , $\theta = 0$ is the unaligned rotor position and θ_a is the aligned rotor position. For the prototype motor, $L_u = 0.01\,H$, $L_a = 0.04\,H$, $\theta_1 = 7^0$, $\theta_2 = 27^0$, $K = 0.09\,N.m/A^2$. Then, torque equation becomes simpler and the corresponding feed-forward compensation can be computed as follows:

$$\begin{aligned} T &= \frac{1}{2}Ki^2 \\ \frac{\partial\psi}{\partial i} &= L_u + K\theta^{'} \\ \frac{\partial\psi}{\partial\theta} &= Ki \\ \frac{\partial T}{\partial i} &= Ki \\ \frac{\partial T}{\partial\theta} &= 0 \\ \hat{f} &= \frac{Ki}{L_u + K\theta^{'}}(-i\hat{R} - Ki\frac{d\theta}{dt}) \\ \hat{b} &= \frac{Ki}{L_u + K\theta^{'}} \end{aligned}$$

$$\hat{u} = \underbrace{\frac{L_u + K\theta^{'}}{Ki}\frac{dT^*}{d\theta}\frac{d\theta}{dt} + i\hat{R} + Ki\frac{d\theta}{dt}} + \underbrace{\frac{L_u + K\theta^{'}}{Ki}\lambda e}$$

$$= \hat{u}_{ff} + u_{fb}$$

$$= \hat{u}_{ff1} + \hat{u}_{ff2} + \hat{u}_{ff3} + u_{fb} \tag{7.13}$$

where,

$$\hat{u}_{ff1} = \frac{L_u + K\theta'}{Ki} \frac{dT^*}{d\theta} \frac{d\theta}{dt}$$
$$\hat{u}_{ff2} = i\hat{R}$$
$$\hat{u}_{ff3} = Ki\frac{d\theta}{dt}$$

When $i = 0$, the nominal voltage equation (7.13) has singularity problem. To take care of these points (at start and end of conduction for each phase), i in denominator is replaced by $(i + 0.1)$.

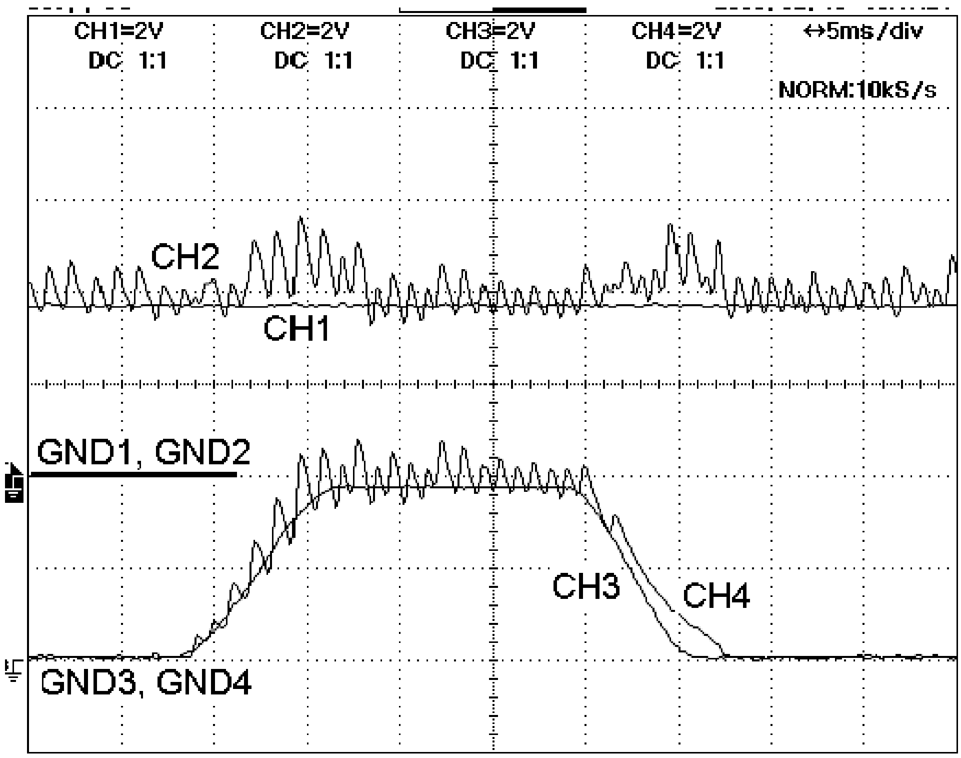

Figure 7.4: Hysteresis type DTC for SRM; ; CH1(0.8 N.m/Div)-Motor torque reference is 1.5 N.m; CH2(0.8 N.m/Div)-Estimated motor torque; CH3(0.8 N.m/Div)-Phase1 torque reference; CH4(0.8 N.m/Div)-Phase1 estimated torque

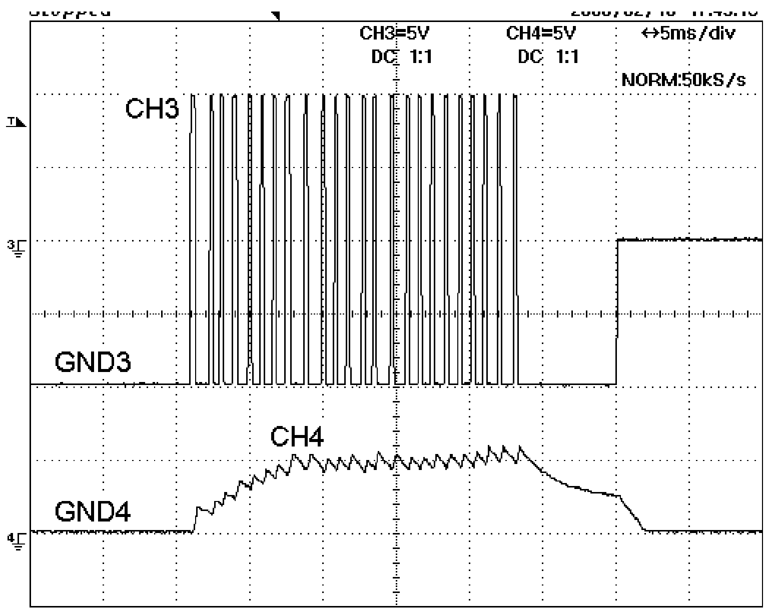

Figure 7.5: Hysteresis type DTC for SRM; Torque reference is 1.5 N.m; CH3(10 V/Div)-Phase1 voltage; CH4(5 A/Div)-Phase1 current

7.1.3 Proposed Variable Gain Feedback Control

The feedback gain is obtained from the bound on model uncertainty D and the desired error bound e_b, by using the relationship $\lambda = \frac{D}{b\hat{b}^{-1}e_b} \simeq \frac{D}{e_b}$. If the worst case deviation over the complete range of operation is used for calculating λ, then a constant but very high gain feedback controller will result. A large feedback gain will result in oscillatory response near unaligned rotor position. Hence, we need to find an estimation for D as a variable in terms of rotor position, phase current and motor speed. This results in a better tracking performance in actual implementation.

$$\begin{aligned}
\parallel d(.) \parallel &\leq \parallel \dot{x}_d(1 - b\hat{b}^{-1}) \parallel + \parallel f - \hat{f}b\hat{b}^{-1} \parallel \\
\parallel \dot{x}_d(1 - b\hat{b}^{-1}) \parallel &= \parallel \frac{dT^*}{d\theta}\frac{d\theta}{dt}\left(1 - \frac{k(i,\theta)}{K}\frac{L_u + K\theta'}{l(i,\theta)}\right) \parallel \\
&= \left|\frac{dT^*}{d\theta}\frac{d\theta}{dt}\right|\left|1 - \left(\frac{k(i,\theta)}{K}\right)_{min}\left(\frac{L_u + K\theta'}{l(i,\theta)}\right)_{min}\right|
\end{aligned}$$

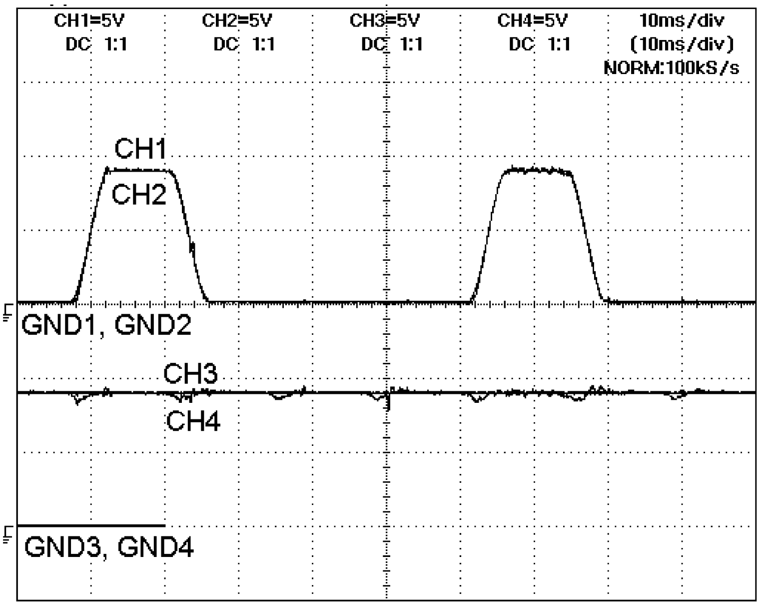

CH1 - Phase1 Torque reference (0.5 Nm/Div)
CH2 - Phase1 estimated torque (0.5 Nm/Div)
CH3 - Motor demanded torque (0.5 Nm/Div)
CH4 - Estimated motor torque (0.5 Nm/Div)

Figure 7.6: Performance of proposed nonlinear robust tracking controller at motor demanded torque of 0.9 N.m and speed of 200 r/min

$$= \left|\frac{dT^*}{d\theta}\frac{d\theta}{dt}\right| \times 0.75, \tag{7.14}$$

with $\left(\frac{k(i,\theta)}{K}\right)_{min}$ as 0.5 as can be seen from the Fig.7.2 and $\left(\frac{L_u+K\theta'}{l(i,\theta)}\right)_{min}$ taken to be 0.5 as can be seen from Fig.7.3.

$$\| f - \hat{f}b\hat{b}^{-1} \| = \left|\frac{\partial T}{\partial i}\left(\frac{\partial \psi}{\partial i}\right)^{-1}\right| \times \left(\| i(R-\hat{R}) \| + \left(\| i(k(i,\theta)-K) \| + \left\|\frac{\partial T}{\partial \theta}\right\|\right)\left|\frac{d\theta}{dt}\right|\right) \tag{7.15}$$

The value of $\frac{\partial T}{\partial \theta}$ is found to be quite small over most of the range of rotor position and can be neglected in computation of D. Assuming 100% variation in phase winding resistance with rise in temperature, $\| i(R-\hat{R}) \| = i\hat{R}$. With this, an estimation of $D(\cdot)$ is obtained as:

$$D(\cdot) = \left|\frac{dT^*}{d\theta}\frac{d\theta}{dt}\right| \times 0.75 + \left(|i\hat{R}| + 0.5 \times Ki \times \left|\frac{d\theta}{dt}\right|\right) \times \left|\frac{k(i,\theta)i}{l(i,\theta)}\right| \tag{7.16}$$

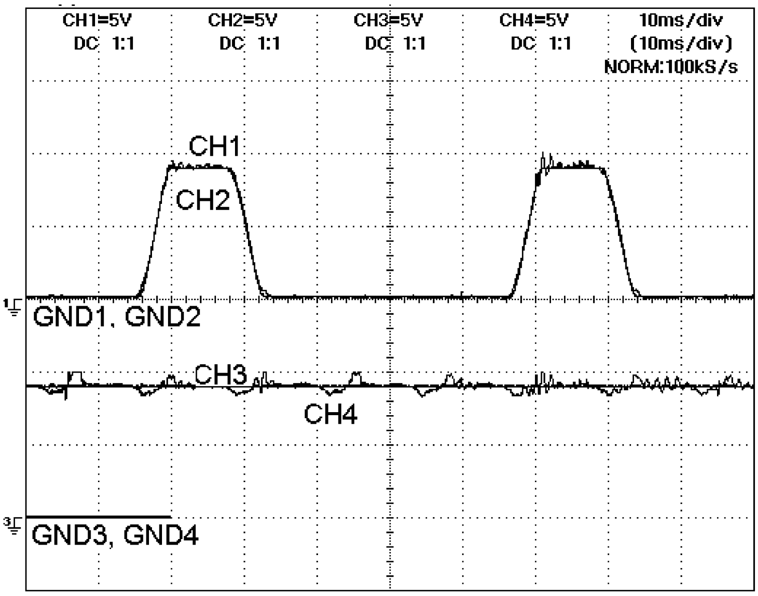

CH1 - Phase1 torque reference (1.0 Nm/Div)
CH2 - Phase1 estimated torque (1.0 Nm/Div)
CH3 - Motor demanded torque (1.0 Nm/Div)
CH4 - Estimated motor torque (1.0 Nm/Div)

Figure 7.7: Performance of proposed nonlinear robust tracking controller at motor demanded torque of 1.8 N.m and speed of 200 r/min

After $D(\cdot)$ is estimated as in (7.16), we can calculate the u_{fb} part of (7.13). This is obtained from the magnitude of the components of the u_{ff} part of the nominal voltage equation, without explicitly computing the values for D and λ. This is given in the following equation:

$$u_{fb} = (|\hat{u}_{ff1}| \times 0.75 + |\hat{u}_{ff2}| + |\hat{u}_{ff3}| \times 0.5) \times \frac{e}{e_b} \tag{7.17}$$

The variable gain feedback control and feed-forward control obtained from the nominal model result in quite accurate torque tracking performance. The following section presents the experimental results.

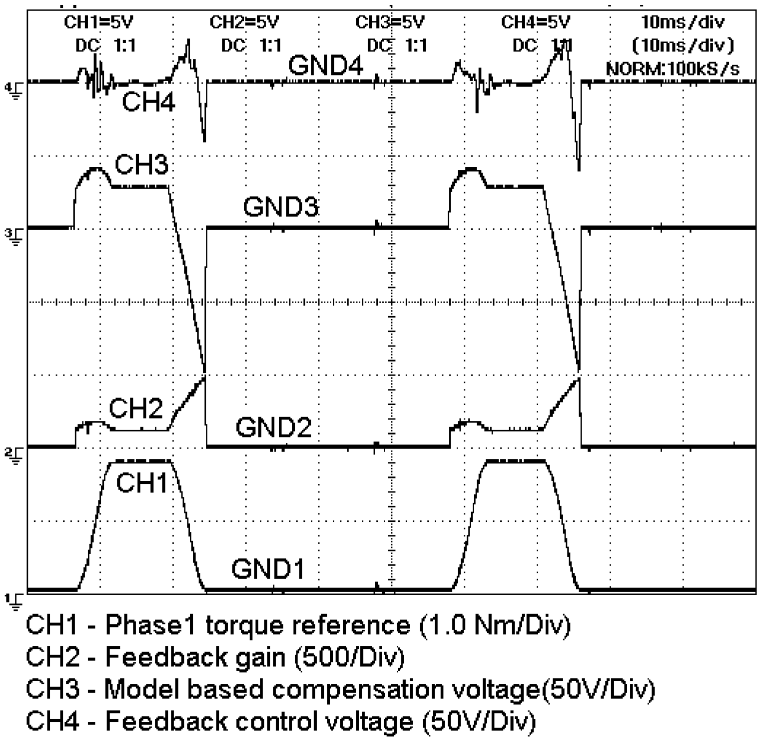

Figure 7.8: Feedback gain variation for the proposed nonlinear robust tracking controller

7.2 Experimental Validation of the NLRTC-based DTC Scheme for SRM

The proposed SMC based DTC scheme has been verified on the experimental laboratory set-up. Program execution takes $200\,\mu s$ i.e. with a sampling frequency of $5\,kHz$. Anti-aliasing filters implemented on analog circuits with cut-off frequency of $1\,kHz$ are used for current feedback. It is desired that phase torques and thereby total motor torque follow respective references accurately, with minimum torque ripples. As there is no direct control of phase current, it is also important to check if phase current remains within the maximum allowable limit, while phase torque is controlled.

A hysteresis type DTC has been implemented in the digital controller to demonstrate its inherent oscillatory response. As an example, DC-link voltage of $100\,V$, and sampling time of $120\mu s$ shows the performance of hysteresis type DTC scheme in Fig.7.4 with corresponding phase1 voltage and current in Fig.7.5. Due to the anti-aliasing filter in current feedback, oscillation in phase1 estimated torque has a fundamental frequency of about $1\,kHz$ instead of the sampling frequency. As can be seen, a narrow hysteresis band can not be achieved in digital implementation. This constraint prevents digital implementation of sign-function based switching control in the classical SMC.

The proposed nonlinear tracking control has been tested at motor demanded torque of $0.9\,N.m$ and $1.8\,N.m$ with motor speed of $200\,r/min$. Fig.7.6 shows the torque tracking with motor demanded torque being at $0.9\,N.m$. CH1(Phase1 torque reference) and CH2(Phase1 estimated torque) show that phase torque tracking is quite accurate. CH3(motor demanded torque) and CH4(estimated motor torque) show that average torque control is quite good with torque ripples being around 5% of the average torque. Fig.7.7 similarly shows the torque control performance at rated torque level of $1.8\,N.m$. Fig.7.8-CH2 shows the variation of feedback gain as calculated by (7.17), with respect to the phase torque reference (CH1). It can be seen that the feedback gain is low during the constant part of the reference and increases towards the aligned position. CH3 shows the model based feed-forward compensation voltage where as CH4 shows the feedback control voltage. Due to the small tracking error, feedback control effort is quite small.

Finally the proposed DTC scheme was tested under transient condition when motor torque was given a step change. As can be seen from Figs.7.9 and 7.10, the

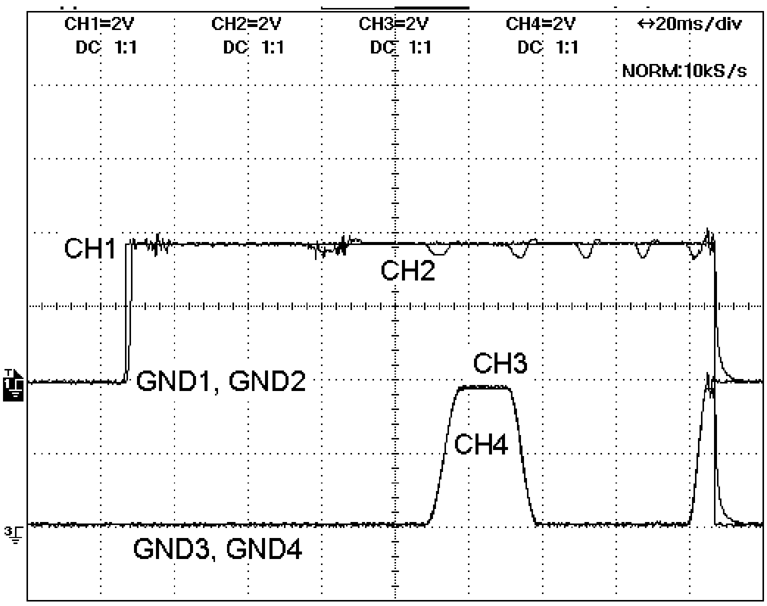

Figure 7.9: Performance of proposed nonlinear robust tracking controller when motor torque is a given a step change of 1.5 N.m

motor torque (CH2) follows the reference value (CH2) closely. The torque ripples are within 10% peak-to-peak. The phase torque tracking as seen from CH3 and CH4 is quite accurate. The motor accelerates till the time the torque reference is applied. There is slight degradation in in the ripples at speed increases. However, the performance is very good for low speeds.

7.3 Summary

This chapter shows a robust direct toque controller for SRM, with emphasis on torque ripple minimization. A nonlinear robust tracking control technique has been proposed for realizing the phase torque references. Direct torque control method avoids errors involved in converting torque references to current references. A feed-forward compensation voltage is calculated using a trapezoidal phase inductance model obtained from the measured flux-linkage data. A variable gain feedback

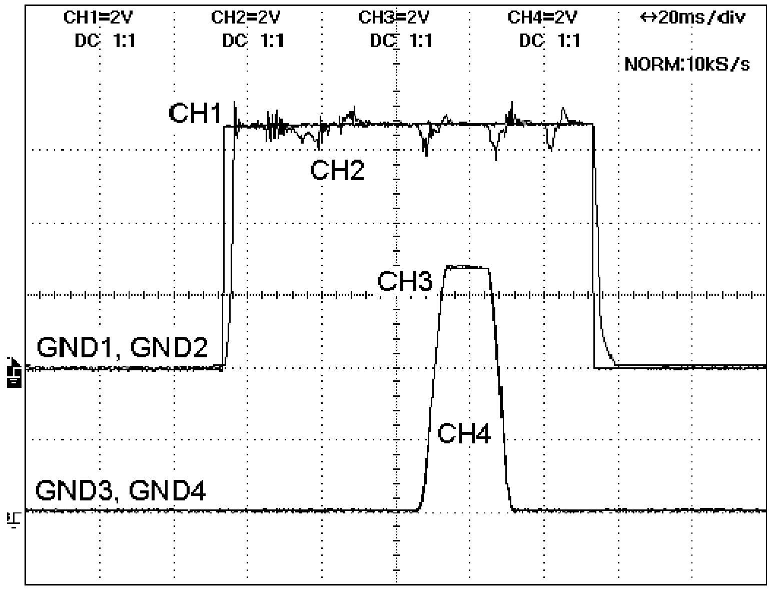

Figure 7.10: Performance of proposed nonlinear robust tracking controller when motor torque is a given a step change of 2.7 N.m

control is added to the feed-forward control that ensures that motor torque error stays within a narrow band. Upper speed limit with accepted torque ripples is decided by the controller bandwidth which in turn depends on sampling frequency and DC-link voltage. It is found to be around $200\, r/min$ for the experimental set-up used for this thesis work. Experimental results with a prototype SRM are provided for validation of the proposed direct torque control scheme.

Chapter 8

Conclusions and Future Work

This chapter concludes the thesis. It briefly restates the motivation of the thesis work, the identified problem areas and the various findings in each problem area. Finally, it shows the the direction of future research in this regard.

8.1 Conclusions

This thesis covers work done on development a high-performance digital torque controller for SRM drives. SRM is the simplest in terms of construction among all electric motors, and hence most robust and economical for mass production. It requires an equally simple and robust converter for its operation. However, inherent torque ripples are known as a major control problem with SRM. High-bandwidth and accurate torque control is necessary for using SRM drives in high-performance motion control applications. With availability of affordable and powerful digital signal processors, it has become possible to use advanced nonlinear control techniques to improve the torque control performance of SRM. The motivation for this thesis was to develop a high-performance digital torque controller for SRM drives.

There are numerous papers published on SRM technology and it would be impossible to cover all of them. However, a thorough review of various torque control schemes and modelling schemes for SRM had been carried out in this thesis work. In Chapter 1, attempts have been made to discuss the state-of-the-art for SRM drive research. The problems of torque control in general and torque ripples in particular have been identified as the major obstacle in broader use of SRM. Therefore, solving the torque control problem has been the focus of this thesis.

It is essential to have a good understanding of the plant before designing a high-performance controller. Detailed modelling of SRM magnetization characteristics was carried out in Chapter 2. Static measurement of stator phase flux-linkage and motor torque have been made on a prototype SRM with 8/6 pole, $1\,hp, 4000\,r/min$. The measured flux-linkage data clearly showed the nonlinear nature of SRM magnetization. After reviewing the past work on SRM modelling, a two-piece polynomial based analytical model has been developed for flux-linkage in terms of phase current and rotor position. The other parameters of SRM such as incremental phase inductance, back-emf constant etc. as required in a dynamic model are derived from the flux-linkage model. An analytical instantaneous torque model in terms of phase current and rotor position, has been derived from the flux-linkage model using the co-energy principle of reluctance torque production. The resultant torque estimator has been validated with measured static torque data. The torque estimator has been used for torque feedback in real-time implementation of the torque controller.

Due to the discrete excitation of the phase windings, a major part of the torque ripples in SRM occurs during the phase commutation. This can be overcome by active sharing of the total motor torque demand among two neighboring phases. Chapter 3 discussed the issues of designing an optimal torque sharing function (TSF) which would provide phase torque references trackable with the available DC-link voltage, while considering additional factors like copper loss in phase windings. Finally, a torque sharing function with cubic segments has been presented, that is the simplest among the various options. Detailed design steps have been laid out for this TSF.

Usually, torque control in electromagnetic motors is done 'indirectly' through current or flux control. At first, phase torque references are converted to phase current references and then implement current tracking controllers to track the phase current references. While torque-to-current conversion is straight forward for DC drives or field-oriented AC drives, it is quite a challenge for SRM. In Chapter 4, iterative learning control has been used for designing a novel torque-to-current conversion scheme for constant torque and constant speed operation. The conversion of phase torque reference to phase current reference was treated like a 'nonlinear root finding' problem. The initial phase current reference for the phase torque reference was obtained by using simplified torque function $T = \frac{1}{2}Ki^2$, that leads to $i = \sqrt{\frac{2T}{K}}$, where K is the position rate of change of phase inductance when phase inductance is assumed to be of trapezoidal shape. A torque estimator is used to obtain a feedback of the torque using the phase current reference and rotor position, and compare with the original phase torque reference. This torque difference is used to learn a compensation component. Each iteration, the current reference is updated by an amount equal to the product of a learning gain and the torque difference in the previous iteration. Iterative learning control has been found to be very accurate in the torque-to-current conversion process.

In the indirect torque control scheme, the phase current references have to be tracked accurately. In Chapter 5, various types of current controllers reported in the literature had been implemented on the experimental platform to compare their performance. It was found that the current tracking controller performance could be improved by using advanced control techniques like sliding mode control (SMC) and iterative learning control (ILC). SMC is a robust tracking control method, suitable for the nonlinear uncertain plants. It only requires a nominal model to design the equivalent control and the bound of uncertainty to design the switching control. The phase inductance measured at the unaligned and aligned positions were used for the ideal trapezoidal profile for designing the feed-forward equivalent control. A simple P-type feedback control was used as switching control, to be tuned on-site for obtaining an accurate and practical current controller. Then, an ILC based current controller was developed where the required phase voltage is learned iteratively. The phase current references were periodic for constant torque and constant speed operation. The current tracking errors and ILC compensation voltages at the sampling instants were stored in memory. During each iteration, the ILC compensation voltages at the sampling instants were updated by a quantity which is the product of the tracking error in previous cycle and the learning gain. A range of values for learning gain was obtained from the ideal phase inductance profile, which would ensure convergence of actual current to the current reference. In practice, the learning gain is increased from a small value until the system starts to diverge. ILC gives very good tracking without using any detailed nonlinear modelling, but this method could be used only for constant torque and constant speed applications.

Then, the ILC based current controller has been added to ILC based torque-to-current conversion, to obtain an indirect torque controller (IDTC) for SRM. This torque control scheme was found to be very accurate in terms of both average torque control and torque ripples minimization. Experimental results are provided at different torque and speed levels to show the effectiveness of the torque controller.

Though ILC based indirect torque control was accurate, there is the problem of interaction between two iterative learning loops. Both the loops can not be activated at the same time. This led to the thought of implementing a direct torque controller (DTC) for SRM using ILC scheme, where phase torque is treated as the control variable in place of phase current. The details of this work are provided in Chapter 6. With the help of an instantaneous phase torque estimator, torque feedback was obtained from measured phase current and rotor position. Iterative learning control updates the phase voltage by an amount proportional to the phase torque tracking error, directly. As the phase torque reference is periodic in rotor position, conventional ILC can be applied for constant speed applications only. To remove this constraint of constant speed, a novel spatial ILC (based on rotor position) was developed and implemented. To improve the robustness of the scheme further, a zero-phase low-pass filter was designed and implemented. Experimental validation of the proposed position ILC based DTC scheme was done. It was shown that for constant motor demanded torque level, the torque ripples were reduced to within 5% at rated torque, for speed around $200\, r/min$.

However, most motion control applications have varying motor torque demand. ILC based DTC scheme can not be used for such applications. Hence, an alternative torque control scheme was sought. Chapter 7 showed a DTC scheme using nonlinear robust tracking control (NLRTC). The NLRTC scheme has a feed-forward and a feedback controller. A feed-forward controller is developed from a simple nominal model obtained from the flux-linkage data. The feed-forward control improves the tracking performance. Robustness is added through a specially designed feedback controller. The bound of model uncertainty is shown to be a fraction of the magnitude of feed-forward control voltage. This results in a variable gain for the feedback controller. The NLRTC based DTC results in good phase torque tracking and hence minimizes the torque ripples. The steady state performance of this scheme is comparable with the ILC based DTC scheme proposed in Chapter 6. This scheme performs better than conventional DTC scheme, where hysteresis type controller leads to variable frequency switching and large amount of torque ripples. Considering these findings, the NLRTC based DTC scheme seems promising as a popular torque control scheme for high-performance applications with SRM drives.

In all, the main objectives as laid out in Chapter 1 of this thesis have been achieved. The findings of this work have been published in international technical conferences and journals for benefit of the future researchers and users of SRM technology. A list of the publications from this thesis work is provided.

8.2 Future Work

The ILC based torque control schemes proposed in this thesis have shown good steady-state performance. However, their dynamic performance could be studied in more details. It is felt that a suitably designed gain for the P-type feedback controller used in ILC schemes can result in quite good dynamic performance. This can be investigated in future work on ILC based torque controller for SRM.

For SRM modelling, the effect of mutual inductance had been neglected. As indicated by [86], mutual coupling among phases contribute to the phase torque. Hence, SRM modelling should include the effect of mutual phase inductance. Inclusion of mutual phase inductance would require further work on torque modelling and torque control algorithm. This would further reduce the torque ripples in SRM.

At low speeds, the applied voltages are small in magnitude. Hence, voltage drops across power devices should be compensated for improving the control accuracy, as shown in [87].

The focus of this thesis had been the low speed operation where torque ripples have the dominant effect. For actual operation of SRM, the control algorithms have to smoothly switch from low speed region to high speed region. Details of this have to be tested experimentally.

The proposed torque control algorithms have to be implemented in closed-loop speed and position control applications. With the inner torque control loop using the proposed NLRTC based DTC scheme, a simple PI controller can be used for the outer loop for closed loop speed and position control schemes. This should be tested experimentally.

The various algorithms have been tested on a rapid-prototyping system with a high-speed DSP. As it is commercially not feasible to use such an expensive controller for actual drive system, investigations are necessary for commercially viable, cheaper controllers with similar high-performance. This step is necessary for commercialization of various findings of this thesis work.

Bibliography

[1] P.C. Sen,“Electric Motor Drives and Control- Past, Present, and Future,” *IEEE Trans. Ind. Electron.,* vol. 37, no. 6, December 1990, pp. 562-575.

[2] H. Moghbelli, G.E. Adams, R.G. Hoft,“Performance of a 10-Hp switched reluctance motor and comparison with induction motors,” *IEEE Trans. Ind. Electron.,* vol. 27, no. 3, May-June 1991, pp. 531-538.

[3] R.S. Colby, F.M. Mottier, T.J.E. Miller, “Vibration modes and acoustic noise in a four-phase switched reluctance motor ,” *IEEE Trans. Ind. Electron.,* vol. 32, no. 6, Nov-Dec 1996, pp. 1357-1364.

[4] W. Cai, P. Pillay, “Resonant frequencies and mode shapes of switched reluctance motors,” *IEEE Transactions on Energy Conversion,* vol. 16, no. 1, March 2001, pp. 43-48.

[5] T. J. E. Miller, “Switched Reluctance Motors and their Control,” *Clarendon Press, Oxford*, 1993.

[6] Krishnan Ramu, “ Switched reluctance motor drives : modeling, simulation, analysis, design, and applications,” *CRC Press*, 2001.

[7] P. J. Lawrenson, J. M. Stephenson, P. T. Blenkinsop, J. Corda and N. N.Fulton, "Variable-speed switched reluctance motors," *IEE Proceedings Part-B,* vol. 127, no. 4, pp. 253-265, July 1980.

[8] I. Husain,"Minimization of torque ripple in SRM drives,"*IEEE Trans. Ind. Electron.*, vol. 49, no. 1, pp. 28-39, Feb. 2002.

[9] M. Garip, Y. Ozoglu, E. Mese, "An approach to torque ripple reduction in fully pitched switched reluctance motors by pole tip shaping," *Electrotechnical Conference, MELECON 2002*, May 2002, pp. 157 - 161.

[10] J. Hur, G.H. Kang, J.Y. Lee, J.P. Hong, B.K. Lee, "Design and optimization of high torque, low ripple switched reluctance motor with flux barrier for direct drive,"*Industry Applications Conference, 2004. 39th IAS Annual Meeting,* vol. 1, Oct. 2004, pp. 401-408.

[11] B. K. Bose, T. J. E. Miller, P. M. Szczesny and W. H. Bicknell, "Microcomputer control of switched reluctance motor," *IEEE Transactions on Industry Applications*, vol. IA-22, no. 4, 1986, pp. 708-715.

[12] A. R. Oza, R. Krishnan and S. Adkar, "A microprocessor control scheme for switched reluctance motor drives," *Proceedings IECON*, 1987, pp. 448-453.

[13] M. Ilic'-Spong, R. Marino, S. Peresada, D. G. Taylor, "Feedback linearizing control of switched reluctance motors," *IEEE Trans. on Automatic Control,* vol. 32, no. 5, pp. 371-379, May 1987.

[14] D.G. Taylor,"An experimental study on composite control of switched reluctance motors," *IEEE Control Systems Magazine,* vol. 11, no. 2, pp. 31-36, Feb 1991.

[15] G.S. Buja, M.I. Valla,"Control characteristics of the SRM drives. II. Operation in the saturated region," *IEEE Trans. on Ind. Electronics,* vol. 38, no. 5, pp. 56-63, Jun 1991.

[16] G. S. Buja, R. Menis, M. I. Valla, "Variable Structure Control of An SRM Drive," *IEEE Trans. on Ind. Electronics,* vol. 40, no. 1, pp. 316-325, February 1993.

[17] G.S. Buja, M.I. Valla,"Control characteristics of the SRM drives. II. Operation in the saturated region," *IEEE Trans. on Ind. Electronics,* vol. 41, no. 3, pp. 316-325, Jun 1994.

[18] J.G. O'Donovan, P.J. Roche, R.C. Kavanagh, M.G. Egan,J.M.G. Murphy, "Neural network based torque ripple minimisation in a switched reluctance motor," *Proceedings IECON '94.*, vol. 2, pp. 1226-1231, Sep 1994.

[19] C. Rochford, R.C. Kavanagh, M.G. Egan, J.M.D. Murphy, "Development of smooth torque in switched reluctance motors using self-learning techniques," *epe '93* vol. 6, pp. 14-19, Sep 1993.

[20] K.M. Rahman, A.V. Rajarathnam, M. Ehsani, "Optimized instantaneous torque control of switched reluctance motor by neural network," *IEEE IAS meeting,* vol. 1 , pp. 556-563, Oct 1997.

[21] R.C. Kavanagh, J.M.D. Murphy, M.G. Egan, "Torque ripple minimization in switched reluctance drives using self-learning techniques," *Proceedings. IECON '91.,* vol. 1, pp. 289-294, Nov 1991.

[22] D.S. Reay, T.C. Green, B.W. Williams, "Minimisation of torque ripple in a switched reluctance motor using a neural network," *Third International Conf. on Artificial Neural Networks,* pp. 224-228, May 1993.

[23] S. Mir, M.E. Elbuluk, I. Husain, "Torque-ripple minimization in switched reluctance motors using adaptive fuzzy control," *IEEE Trans. on Ind. Applications,* vol. 35, no. 2, pp. 461-468, Mar/Apr 1999.

[24] S.K.Panda, X.M. Zhu, P.K.Dash,"Fuzzy gain scheduled PI speed controller for switched reluctance motor drive," *23rd International Conference on Industrial Electronics, Control and Instrumentation,* vol. 3, Nov. 1997, pp. 989-994.

[25] L.O.A.P. Henriques, L.G.B. Rolim, W.I. Suemitsu, P.J.C. Branco, J.A. Dente, "Torque ripple minimization in a switched reluctance drive by neuro-fuzzy compensation," *IEEE Transactions on Magnetics,* vol. 36, no. 5, pp. 3592-3594, Sept 2000.

[26] L.O.A.P. Henriques, P.J. Costa Branco, L.G.B. Rolim, W.I. Suemitsu, "Proposition of an offline learning current modulation for torque-ripple reduction in switched reluctance motors: design and experimental evaluation," *IEEE Trans. on Industrial Electronics,* vol. 49, no. 3, pp. 665-676, June 2002.

[27] J.J. Carroll, A.J. Geoghan, D.M. Dawson, P. Vedagarbha, "A backstepping based computed torque controller for switched reluctance motors driving inertial loads," *Proceedings of the 4th IEEE Conference on Control Applications,* Sept. 1995, pp. 779-786.

[28] D. Kim, S. Kim"An Iterative Learning Control Method with Application for CNC Machine Tools," *IEEE Trans. Ind. Electron.,* vol. 32, no. 1, January 1996, pp. 66-72.

[29] N.C. Sahoo, J.X.Xu, S.K. Panda,"Low torque ripple control of switched reluctance motors using iterative learning," *IEEE Trans. Energy Conversion*, vol. 16, no. 4, pp. 318-326, Dec. 2001.

[30] J.-X. Xu, S.K. Panda, Y.-J. Pan, T. H. Lee, B.H. Lam, "A Modular Control Scheme for PMSM Speed Control With Pulsating Torque Minimization," *IEEE Trans. on Ind. Electron.,* vol. 51, no. 3, June 2004, pp. 526-536.

[31] S. Vukosavic, V. R. Stefanovic, "SRM Inverter Topologies: A Comparative Evaluation," *IEEE Transactions on Industry Applications*, vol. 27, nN. 6, 1991, pp. 1034-1047.

[32] A. Derdiyok, N.Inanc, V. Ozbulur, Y. Ozoglu, "Optimal phase current profiling of SRM by fuzzy logic controller to minimize torque ripple," *Proceedings of the 1997 IEEE International Symposium on Intelligent Control,* July 1997, pp. 77-82.

[33] K.I. Hwu, C.M. Liaw, "Intelligent tuning of commutation for maximum torque capability of a switched reluctance motor," *IEEE Transactions on Energy Conversion,* vol. 18, no. 1, March 2003, pp. 113-120.

[34] Changhwan Choi; Seungho Kim; Yongdae Kim; Kyihwan Park, "A new torque control method of a switched reluctance motor using a torque-sharing function," *IEEE Transactions on Magnetics,* vol. 38, no. 5, pp. 3288-3290, Sep 2002.

[35] K.I. Hwu, C.M. Liaw, "Intelligent tuning of commutation for maximum torque capability of a switched reluctance motor," *IEEE Transactions on Energy Conversion,* vol. 18, no. 1, pp. 113-120, Mar 2003.

[36] I. Husain, and M. Ehsani, "Torque Ripple minimization in Switched Reluctance Motor Drives by PWM Current Control," *IEEE Trans. Power Electron.*, vol. 11, no. 1, pp. 83-88, 1996.

[37] P.G.Barrass, and B.C. Mecrow,"Flux and Torque control of switched reluctance motor," *IEE Proc.-Electr. Power Appl.*, vol. 145, pp. 519-527, Nov. 1998.

[38] S.E. Schulz, and K.M.Rahman,"High performance digital PI current regulator for ev switched reluctance motor drives," *IEEE IAS Meeting*, vol. 3, pp. 1617-1624, 2002.

[39] R. S. Wallace, and D. G. Taylor,"A balanced commutator for switched reluctance motors to reduce torque ripple," it IEEE Trans. Power Electronics, vol.7, no.4, pp.617-626, Oct, 1992.

[40] K. Russa, I. Husain, M.E. Elbuluk, "A self-tuning controller for switched reluctance motors," *IEEE Trans. on Power Electronics,* vol. 15, no. 3, pp. 545-552, May 2000.

[41] K.J. Tseng, Shuyu Cao, "A SRM variable speed drive with torque ripple minimization control," *IEEE APEC* vol. 2, pp. 1083-1089, 2001.

[42] Ge Baoming, Wang Xiangheng, Su Pengsheng, and Jiang Jingping, "Nonlinear internal-model control for switched reluctance drives," *IEEE Trans. Power Electron.*, vol. 17, no. 3, pp. 379-388, May 2002.

[43] V. Ramanarayanan, L. Venkatesha, D. Panda,"Flux-linkage characteristics of switched reluctance motor," *Proceedings of the 1996 International Conference on Power Electronics, Drives and Energy Systems for Industrial Growth, 1996,* vol. 1, Jan. 1996, pp. 281-285.

[44] J. C. Moreira, "Torque ripple minimization in switched reluctance motors via bicubic spline interpolation," *IEEE PESC*, pp.851-856, June, 1992.

[45] D.A. Torrey, and J.H. Lang, "Modelling a nonlinear variable-reluctance motor drive," *Electric Power Applications,IEE Proceedings B* , vol. 137, Issue: 5, pp. 314-326, Sep 1990.

[46] D.G. Taylor, M. Illic-Spong, and S. Peresada, "Non-linear composite control of switched reluctance motors," *IEE Industrial electronics conference*, pp. 739-749, Sep 1986.

[47] D.A. Torrey, X.-M. Niu, and E.J. Unkauf, "Analytical modelling of variable-reluctance machine magnetisation characteristics," *Electric Power Applications, IEE Proceedings-*, vol. 142, no. 1, pp. 14-22, Jan 1995.

[48] Wei Min Chan, and W.F. Weldon, "Development of a simple nonlinear switched reluctance motor model using measured flux linkage data and curve fit," *IEEE IAS Annual Meeting*, vol. 1, pp. 318-325, Oct 1997.

[49] J. Mahdavi, G. Suresh, and M. Ehsani,"Dynamic modeling of nonlinear SRM drive with Pspice ," *IEEE Industry Applications Conference Thirty-Second IAS Annual Meeting,* vol. 1, Oct. 1997, pp. 661-667.

[50] M. Stiebler, and Ke Liu, "An analytical model of switched reluctance machines," *, IEEE Trans. Energy Conversion,* vol. 14, no. 4, pp. 1100-1107, Dec 1999.

[51] S. Saha, K. Ochiai, T. Kosaka, N. Matsui, and Y. Takeda, "Developing a sensorless approach for switched reluctance motors from a new analytical model," *IEEE IAS Annual Meeting* vol. 1, pp. 525-532, 1999.

[52] N. C. Sahoo,"A Study on Application of Modern Control techniques for Torque Control of Switched Reluctance Motors," Ph.D. Thesis, National University of Singapore, 2001.

[53] S.-U. Rehman, D.G. Taylor, " Piecewise modeling and optimal commutation of switched reluctance motors," *Proceedings of the IEEE International Symposium on Industrial Electronics, 1995. ISIE '95.,* vol. 1, July 1995, pp. 266-271.

[54] D. W. Marquardt, "An algorithm for least-squares estimation of nonlinear parameters," *Journal of the Society for Industrial and Applied Mathematics*, vol. 11, no. 2, June 1963, pp. 431-441.

[55] P.G. Barrass, B.C. Mecrow,"Flux and torque control of switched reluctance machines,"*IEE Proceedings-Electric Power Applications,* vol. 145, no. 6, Nov. 1998, pp. 519-527.

[56] M.T. Alrifai, J.H. Chow, D.A. Torrey,"Practical application of backstepping nonlinear current control to a switched-reluctance motor,"*Proceedings of the 2000 erican Control Conference,* vol. 1, no. 6, June 2000, pp. 594-599.

[57] F. Blaabjerg, P.C.Kjaer, P.O. Rasmussen, C. Cossar,"Improved digital current control methods in switched reluctance motor drives,"*IEEE Transactions on Power Electronics,* vol. 14, no. 3, May 1999, pp. 563-572.

[58] X. Wang, J.-S. Lai"Small-signal modeling and control for PWM control of switched reluctance motor drives,"*IEEE 33rd Annual Power Electronics Specialists Conference, 2002,* vol. 2, June 2002, pp. 546-551.

[59] P.L. Chapman, and S.D. Sudhoff,"Design and precise realization of optimized current waveforms for an 8/6 switched reluctance drive," *IEEE Tans. Power Electronics*, vol.17, no.1, pp.76-83, Jan. 2002.

[60] H.K. Bae, B.S. Lee, P. Vijayraghavan, R. Krishnan, "A linear switched reluctance motor: converter and control," *IEEE Trans. on Ind. Applications,* vol. 36, no. 5, pp. 1351-1359, Sep 2000.

[61] M. Sun, Danwei Wang"Sampled-data iterative learning control for a class of nonlinear systems,"*Proceedings of the 1999 IEEE International Symposium on Intelligent Controlhtelligent Systems and Semiotics,* September 1999, pp. 338-343.

[62] C.-J. Chien, 'A Discrete Iterative Learning Control for a Class of Nonlinear Time-Varying Systems,"*IEEE Trans. on Automatic Control*, vol. 43, no. 5, May 1998, pp. 748-752.

[63] J.-X. XU, "Analysis of Iterative Learning Control for a Class of Nonlinear Discrete-time Systems,"*Automatica,* vol. 33, no. 10, 1997, pp. 1905-1907.

[64] Ismail Agirman, ALeskanda M. Stancovic, Gilead Tadmore, and Hanch Lev-Ari, "Adaptive torque-ripple minimization in switched reluctance motors," *IEEE Trans. Ind. Electronics*, vol. 48, no. 3, pp. 664-672, June 2001.

[65] K.K.Tan, H. Dou, Y. Chen, and T.H. Lee,"High Precision Linear Motor Control via Relay-Tuning and Iterative Learning Based on Zero-phase Filtering," *IEEE Trans. Contr. Syst. Technol.*, vol. 9, no. 2, pp. 244-253, Mar. 2001.

[66] Chiang-Ju Chien,"A discrete iterative learning control for a class of nonlinear time-varying systems," *IEEE Trans. Automatic Control,* vol. 43, no. 5, pp. 748-752, May 1998.

[67] N.C. Sahoo, J.X. Xu, S.K. Panda, "Determination of current waveforms for torque ripple minimisation in switched reluctance motors using iterative learning: an investigation,"*IEE Proceedings-Electric Power Applications,* vol. 146, no. 4, July 1999 , pp. 369-377.

[68] J.M. Stephenson, A. Hughes, R. Mann,"Torque ripple minimisation in a switched reluctance motor by optimum harmonic current injection,"*IEE*

Proceedings-Electric Power Applications, vol. 148, no. 4, July 2001, pp. 322-328.

[69] R.S. Wallace, D.G. Taylor, "Low-torque-ripple switched reluctance motors for direct-drive robotics," *IEEE Trans. on Robotics and Automation,* vol. 7, no. 6 , pp. 733-742, Dec 1991.

[70] I. Takahashi and T. Noguchi, "A new quick-response and high efficiency control strategy of an induction machine," *IEEE Trans. Ind. Applicat.,* vol. IA-22, pp. 820827, Sept./Oct. 1986.

[71] M. Depenbrock, "Direct self control of inverter-fed induction machines," *IEEE Trans. Power Electron.,* vol. 3, pp. 420429, Oct. 1988.

[72] G.S. Buja, M.P. Kazmierkowski, "Direct torque control of PWM inverter-fed AC motors - a survey," *IEEE Trans. Ind. Electron.*, vol. 51, no. 4, pp. 744-757, Aug 2004.

[73] R.B. Inderka, and R.W. De Doncker, "DITC-direct instantaneous torque control of switched reluctance drives," *IEEE IAS Annual Meeting*, vol. 3, pp. 1605-1609, 2002.

[74] R. B. Inderka, R. W. De Doncker, "High dynamic direct average torque control for switched reluctance drives," *IEEE IAS Meeting,* vol. 3, pp. 2111-2115, Sep-Oct 2001.

[75] C.R. Neuhaus, N.H. Fuengwarodsakul, and R.W. De Doncker, "Predictive PWM-based Direct Instantaneous Torque Control of Switched Reluctance Drives," *37th IEEE Power Electronics Specialists Conference,* pp. 3240-3246, June, 2006, Jeju, Korea.

[76] S. K. Panda and P. K. Dash, "Application of nonlinear control to switched reluctance motors: a feedback linearization approach," *IEE Proceedings Part-B*, vol. 143, no. 5, September 1996, pp. 371-379.

[77] N. Inanc, A. Derdiyok, V. Ozbulur, "Torque ripple minimization of a switched reluctance motor including mutual inductances via sliding mode control technique," *Proceedings of the IEEE International Symposium on Industrial Electronics,* vol. 3, July 1997, pp. 1024-1028.

[78] D.S. Schramm, B.W. Williams, T.C. Green, "Torque ripple reduction of switched reluctance motors by phase current optimal profiling," *IEEE PESC* vol. 2, pp. 857-860, Jun-Jul 1992.

[79] G. Gallegos-Lopez, K. Rajashekara, "Peak PWM current control of switched reluctance and AC machines," *Conference Record of the Industry Applications Conference,* vol. 2, Oct. 2002, pp. 1212-1218.

[80] J.J. Gribble, P.C. Kjaer, T.J.E. Miller, "Optimal commutation in average torque control of switched reluctance motors," *IEE Proceedings-Electric Power Applications,* vol. 146, no. 1, Jan. 1999, pp. 2-10.

[81] P.C.Kjaer, P.Nielsen, L. Andersen, F. Blaabjerg, "A new energy optimizing control strategy for switched reluctance motors," *IEEE Transactions on Industry Applications,* vol. 31, no. 5, Sept.-Oct. 1995, pp. 1088-1095.

[82] P. Jinupun, P. Chi-Kwong Luk, "Direct torque control for sensorless switched reluctance motor drives," *Seventh International Conference on Power Electronics and Variable Speed Drives(IEE Conf. Publ. No. 456),* Sept. 1998, pp. 329-334.

[83] L.O.A.P. Henriques, L.G.B. Rolim, W.I.Suemitsu, P.J.C.Branco, J.A.Dente,"Torque ripple minimization in a switched reluctance drive by neuro-fuzzy compensation,"*IEEE Transactions on Magnetics,* vol. 36, no. 5, Sept 2000, pp. 3592-3594.

[84] Haiqing Yang; S.K. Panda, Y.C. Liang,"Sliding mode control for switched reluctance motors: an experimental investigation,"*Proceedings of the 1996 IEEE IECON 22nd International Conference on Industrial Electronics, Control, and Instrumentation,* vol. 1, Aug. 1996 , pp. 96-101.

[85] Y. Haiqing, S.K. Panda, Y. C. Liang, "Performance comparison of sliding mode control with PI control for four-quadrant operation of switched reluctance motors,"*Proceedings of the 1996 International Conference on Power Electronics, Drives and Energy Systems for Industrial Growth,* vol. 1, Jan. 1996, pp. 381-387.

[86] Han-Kyung Bae; R. Krishnan, "A novel approach to control of switched reluctance motors considering mutual inductance," *IEEE IECON,* vol. 1, pp. 369-374, 2000.

[87] C.R. Neuhaus, N.H. Fuengwarodsakul, and R.W. De Doncker, "Predictive PWM-based Direct Instantaneous Torque Control of Switched Reluctance Drives," *37th IEEE Power Electronics Specialists Conference,* pp. 3240-3246, June 18 - 22, 2006, Jeju, Korea.

[88] H. CAILLEUX, B.L. PIOUFLE, B. MULTON, C. SOL, "Effect of the sampling and of the phase commutation in nonlinear position control of a switched reluctance motor - Analysis and compesationI," *Proceedings of the 32nd Conference on Decision and Control*, December 1993, pp. 3403-3404

Publications

Published

Transactions

1. S. K. Sahoo, S. K. Panda, and J. X. Xu, "Iterative Learning based High Performance Current Controller for Switched Reluctance Motors," *IEEE Trans. on Energy Conversion*,vol. 19, no. 3, pp. 491-498, Sep. 2004.

2. S. K. Sahoo, S. K. Panda, and J. X. Xu, "Indirect Torque Control of Switched Reluctance Motors using Iterative Learning Control," *IEEE Trans. on Power Electronics*,vol. 20, no. 1, pp. 200-208, Jan. 2005.

Conferences

1. S. K. Sahoo, S. K. Panda, and J. X. Xu"Iterative Learning based High Performance Current Controller for Switched Reluctance Motors," *EPE 2003*, September 2003.

2. S. K. Sahoo, S. K. Panda, and J. X. Xu, "Model-based Torque Estimator for Switched Reluctance Motors," *IEEE PEDS 2003*, Nov, 2003, Singapore.

3. S. K. Sahoo, S. K. Panda, and J. X. Xu, "Iterative Learning based Torque Ripple Minimization in Switched Reluctance Motors," *IEEE IECON 2003*, Nov, 2003, USA.

4. S. K. Sahoo, S. K. Panda, and J. X. Xu, "Iterative Learning Control based Direct Instantaneous Torque Control of Switched Reluctance Motors," *IEEE PESC 2004*, June, 2004, Germany.

5. S. K. Sahoo, S. K. Panda, and J. X. Xu, "Direct Torque Controller for Switched Reluctance Motor using Sliding Mode Control," *IEEE PEDS 2005*, Nov, 2005, KualaLumpur, Malaysia.

Accepted

Conference

1. S. K. Sahoo, S. K. Panda, and J. X. Xu, "Application of Spatial Iterative Learning Control for Direct Torque Control of Switched Reluctance Motor Drive," *PES Annual meeting* Tampa, Florida, June 2007 .

Submitted for Review

Transactions

1. S. K. Sahoo, S. K. Panda, and J. X. Xu"Torque Control of Switched Reluctance Motor Drive using Nonlinear Robust Tracking Control,"*IEEE Trans. on Power Electronics*

2. S. K. Sahoo, S. K. Panda, and J. X. Xu"Application of Spatial Iterative Learning Control for Direct Torque Control of Switched Reluctance Motor Drive," *IEEE Trans. on Energy Conversion*

3. S. K. Sahoo, S. K. Panda, and J. X. Xu"Novel Piecewise Cubic Polynomial model for SRM to implement real-time model-based controllers," *IEEE Trans. on Magneitcs*

Appendices

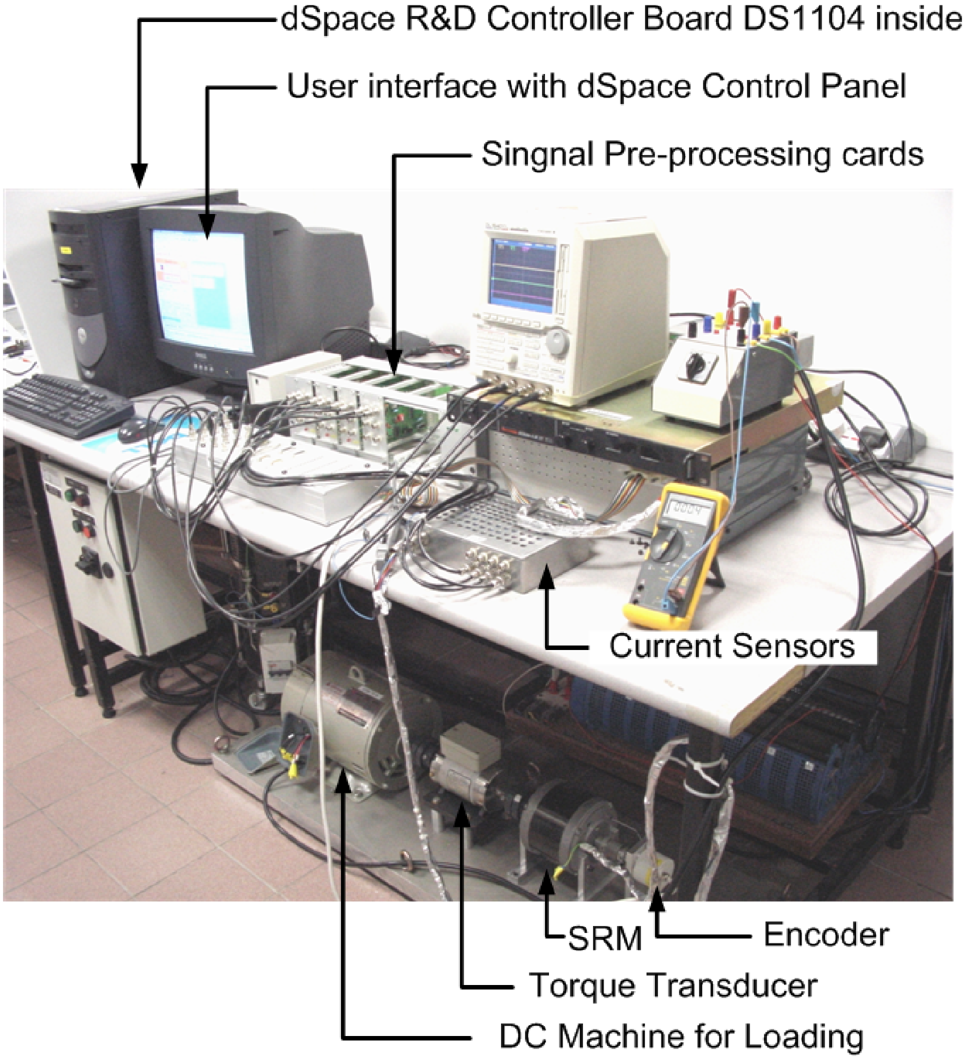

Photo of Experimental Setup

Appendix A

Measured phase flux-linkage (Wb-t) data with rotor locked at different positions and for different phase currents.

Phase current	1A	2A	3A	4A	5A	6A	7A	8A	9A
Rotor position									
0	0.0058061	0.015183	0.023261	0.032912	0.042862	0.052638	0.062502	0.072058	0.081972
1	0.0058061	0.015183	0.023261	0.032912	0.042862	0.052638	0.062502	0.072058	0.081972
2	0.0057113	0.015026	0.023275	0.033096	0.043076	0.053168	0.063075	0.072633	0.082753
3	0.0057822	0.015314	0.023752	0.033901	0.044029	0.054497	0.064587	0.074287	0.084742
4	0.0062539	0.016286	0.024989	0.035431	0.046069	0.056894	0.067393	0.077353	0.088172
5	0.0067684	0.017502	0.026825	0.03787	0.049312	0.060497	0.071552	0.082124	0.093326
6	0.0082337	0.019972	0.030478	0.042267	0.05483	0.066518	0.078007	0.089234	0.10071
7	0.010162	0.023771	0.035922	0.049046	0.062338	0.074542	0.086343	0.097994	0.10967
8	0.012915	0.029004	0.043164	0.057388	0.07134	0.083976	0.095816	0.10754	0.11926
9	0.015578	0.034483	0.05097	0.066519	0.080739	0.093576	0.10541	0.11709	0.12862
10	0.018316	0.039889	0.059233	0.075956	0.090489	0.10335	0.11516	0.12672	0.13805
11	0.02103	0.045422	0.067645	0.085921	0.10073	0.11356	0.12528	0.13684	0.14792
12	0.023239	0.050993	0.075711	0.095493	0.1108	0.12371	0.13535	0.14681	0.15788
13	0.025898	0.056553	0.083543	0.10475	0.12083	0.13367	0.14535	0.15667	0.16769
14	0.028455	0.062452	0.091761	0.11412	0.13102	0.14389	0.15556	0.16675	0.1774
15	0.031346	0.068304	0.10006	0.12368	0.14106	0.15397	0.16575	0.1766	0.18681
16	0.033803	0.073903	0.10826	0.13304	0.15097	0.16399	0.17559	0.18599	0.19562
17	0.036974	0.079928	0.11656	0.14278	0.16095	0.17403	0.18535	0.19515	0.20425
18	0.039472	0.085442	0.1247	0.15188	0.17069	0.18367	0.19436	0.20374	0.21229
19	0.042175	0.091178	0.13303	0.1612	0.1802	0.1931	0.20316	0.21223	0.2204
20	0.04473	0.096317	0.14071	0.16954	0.18856	0.20107	0.21086	0.21966	0.22767
21	0.047794	0.10189	0.14858	0.17798	0.19636	0.20875	0.2184	0.22678	0.23449
22	0.050802	0.10745	0.15625	0.18561	0.20322	0.21539	0.22515	0.23313	0.24055
23	0.053025	0.11297	0.16371	0.19241	0.20947	0.2219	0.2316	0.2393	0.24634
24	0.054964	0.11813	0.17049	0.19809	0.21485	0.22712	0.2369	0.24459	0.25146
25	0.05665	0.12313	0.17683	0.20287	0.21917	0.23167	0.24131	0.24904	0.25576
26	0.059123	0.12827	0.1825	0.20715	0.22281	0.2351	0.24465	0.25228	0.25895
27	0.061778	0.13263	0.187	0.21013	0.22527	0.23751	0.24676	0.25433	0.26071
28	0.064176	0.13731	0.19021	0.21246	0.22748	0.23924	0.2484	0.25582	0.26195
29	0.065357	0.14045	0.19214	0.21378	0.22881	0.24031	0.24931	0.25667	0.26254
30	0.065357	0.14045	0.19214	0.21378	0.22881	0.24031	0.24931	0.25667	0.26254

Appendix B

Measured phase torque (N.m) data with rotor locked at different positions and for different phase currents.

Phase current	1A	2A	3A	4A	5A	6A	7A	8A	9A
Rotor position									
0	0	0	0	0	0	0	0	0	0
1	0.002442	0.007955	0.024605	0.047952	0.070941	0.10123	0.14297	0.18685	0.23473
2	0.003737	0.019092	0.048211	0.088245	0.13521	0.19373	0.26873	0.34687	0.44086
3	0.007696	0.036001	0.076627	0.13831	0.21546	0.30984	0.42546	0.5503	0.69382
4	0.011618	0.058793	0.11995	0.21401	0.3357	0.47878	0.65176	0.84686	1.067
5	0.020017	0.088097	0.18785	0.33603	0.53265	0.75369	1.0207	1.3199	1.6427
6	0.035335	0.14822	0.32734	0.58138	0.89307	1.2422	1.6253	2.0232	2.4568
7	0.060162	0.22848	0.51375	0.88471	1.3117	1.7668	2.2522	2.7276	3.2386
8	0.080068	0.29681	0.66496	1.1331	1.6502	2.1775	2.711	3.2331	3.7799
9	0.087949	0.32682	0.73282	1.2391	1.7941	2.3277	2.889	3.431	3.993
10	0.08658	0.32775	0.73275	1.2528	1.8297	2.3717	2.9297	3.508	4.0685
11	0.084286	0.32738	0.73867	1.2639	1.8415	2.3839	2.9644	3.535	4.1011
12	0.084064	0.32542	0.74089	1.2702	1.8426	2.3898	2.9696	3.5513	4.1314
13	0.083768	0.32708	0.74333	1.2628	1.8282	2.3872	2.9789	3.5446	4.1351
14	0.082658	0.32597	0.74037	1.2465	1.8104	2.3847	2.9611	3.5402	4.1236
15	0.080512	0.32412	0.74037	1.2321	1.7941	2.3761	2.9459	3.5231	4.0752
16	0.078884	0.31968	0.7363	1.2258	1.7849	2.3687	2.9289	3.478	4.0119
17	0.077885	0.31487	0.7363	1.2251	1.7767	2.3484	2.8927	3.4118	3.9194
18	0.077922	0.31302	0.73815	1.2203	1.7605	2.3095	2.8201	3.3074	3.7929
19	0.080734	0.32116	0.74703	1.2206	1.7346	2.2367	2.7132	3.1872	3.6408
20	0.085174	0.32967	0.74148	1.2103	1.6846	2.1453	2.5981	3.0425	3.4761
21	0.089799	0.33355	0.73563	1.1862	1.6258	2.035	2.4668	2.8771	3.2937
22	0.091908	0.33022	0.71972	1.1422	1.5296	1.8981	2.294	2.6644	3.0503
23	0.091649	0.32911	0.70677	1.0815	1.423	1.7497	2.0949	2.4257	2.7691
24	0.091094	0.32671	0.68413	1.0134	1.3031	1.5936	1.8822	2.1675	2.4542
25	0.091501	0.3182	0.6623	0.93684	1.1914	1.4352	1.6761	1.9111	2.1479
26	0.08917	0.30303	0.62271	0.85396	1.0678	1.261	1.4548	1.6365	1.816
27	0.075998	0.27898	0.56203	0.75258	0.92315	1.0675	1.2162	1.352	1.4785
28	0.051948	0.22977	0.45214	0.59866	0.72224	0.82473	0.92944	1.0186	1.0974
29	0.025298	0.15318	0.29045	0.3774	0.44696	0.49987	0.55574	0.60495	0.64417
30	0	0	0	0	0	0	0	0	0